

DIAMOND SEEDING PROCESS FOR THE HETEROGENEOUS INTEGRATION OF
HIGH-QUALITY DIAMOND ON SEMICONDUCTORS

by

Anupam K.C., B.S., M.S.

A dissertation submitted to the Graduate Council of
Texas State University in partial fulfillment
of the requirements for the degree of
Doctor of Philosophy
with a Major in Materials Science, Engineering, and Commercialization
May 2022

Committee Members:

Edwin L. Piner, Chair

Mark W. Holtz, Co-Chair

Yoichi Miyahara

Casey Smith

Christopher Engdahl

COPYRIGHT

by

Anupam K.C.

2022

FAIR USE AND AUTHOR'S PERMISSION STATEMENT

Fair Use

This work is protected by the Copyright Laws of the United States (Public Law 94-553, section 107). Consistent with fair use as defined in the Copyright Laws, brief quotations from this material are allowed with proper acknowledgement. Use of this material for financial gain without the author's express written permission is not allowed.

Duplication Permission

As the copyright holder of this work I, Anupam K.C., refuse permission to copy in excess of the "Fair Use" exemption without my written permission.

DEDICATION

I dedicate this work to my father *Balaram K C* and mother *Kanchi K C*.

ACKNOWLEDGEMENTS

I consider myself fortunate to have had the opportunity to work and grow alongside many wonderful people during my graduate studies at Texas State University, both in the M.S. in Material Physics and the Ph.D. in Material Science, Engineering, and Commercialization (MSEC) Program.

First and foremost, I would like to express my heartfelt gratitude to my advisor, Professor Dr. Edwin Piner, for his dedication and personal investment in me, as well as his graceful abilities to teach and motivate. He assisted me in a variety of ways during the difficult research I was involved in, as well as providing access to our excellent lab facilities. It would be impossible to complete my work and this dissertation without his active supervision. I'd also like to thank my co-adviser, Professor Dr. Mark Holtz, for his dedication, collaboration, and thoughtful discussions about various aspects of physics as well as research data. He is one of the most brilliant physicists and mentors I've ever met. I am fortunate to work under his supervision.

I would also like to thank Christopher Engdahl from Crystallume for tolerating me and providing valuable support on CVD tools during this dissertation research. His help regarding the CVD tool was beyond the expectations. I would also like to thank my committee members, Dr. Yoichi Miyahara, Dr. Casey Smith for their valuable time and suggestions throughout my work.

I am thankful to my fellow lab mate Dr. Anwar Siddique, Dr. Jonathan Anderson, and Anival Ayala for supporting the experimental work in the lab and providing training for the tools. I would like to thank the Texas State ARSC and NRSC technical teams and support staff, with special acknowledgement to Dr. Casey Smith, Dr. Joyce Anderson, Dr. Juan Gomez, Brian Samuels, and Jacob Armitage for the many hours spent training and answering my questions. I wish to thank Dr. Jennifer Irvin and Dr. Tania Betancourt for their help, guidance, and encouragement. I would like to thank the MSEC program for providing financial support for my doctoral degree. Thanks are due to the outstanding faculty staffs of the MSEC program, especially Karla Pizana and Kelsie Crumpton for their continual support throughout the journey. I also gratefully acknowledge the National Science Foundation and US Army Research Office for partial funding of my PhD research.

My gratitude and appreciation are insufficient for my wife Rajina Ranabhat K.C., whose encouragement and support have been invaluable to me over the last few years. I'm looking forward to assisting her on her journey, just as she has aided me.

TABLE OF CONTENTS

	Page
ACKNOWLEDGEMENTS	v
LIST OF TABLES	ix
LIST OF FIGURES	x
LIST OF ABBREVIATIONS.....	xvi
ABSTRACT.....	xviii
 CHAPTERS	
I. INTRODUCTION	1
Diamond.....	3
Chemistry of CVD Diamond Deposition.....	6
Wide Bandgap Electronics.....	18
III-Nitrides Heterostructures.....	20
Ultra-Wide Bandgap Semiconductors	22
Research Motivations.....	24
Research Problems and Solution	25
Dissertation Outline	27
II. CHEMICAL VAPOR DEPOSITION PROCESSES AND CHARACTERIZATION TECHNIQUES	30
Hot Filament Chemical Vapor Deposition	30
Metal-Organic CVD for III-Nitride Deposition.....	33
Characterization Techniques.....	37

III. STUDY OF AND OPTIMIZED NANO-DIAMOND SEEDING ON SEMICONDUCTORS	61
Introduction.....	61
Experiment and Results	63
Summary	75
IV. EFFECT OF SEEDING DENSITY ON THE GROWTH OF DIAMOND FILMS BY HOT-FILAMENT CHEMICAL VAPOR DEPOSITION FROM SPARSE TO DENSE RANGE	77
Introduction.....	78
Experiment and Results	80
Summary	111
V. ULTRAHIGH SEEDING DENSITY TO ACHIEVE DIRECT GROWTH OF DIAMOND ON GALLIUM NITRIDE WITHOUT DIELECTRIC ADHESION INTERLAYER.....	113
Introduction.....	113
Experiment and Results	115
Summary	131
VI. STUDY ON THE HETEROGENEOUS INTEGRATION OF DIAMOND ON ULTRA-WIDEBAND GAP SEMICONDUCTOR.....	133
Integration of Diamond on AlN with Different Seeding Density	133
Integration of Diamond on High Al Content $Al_xGa_{1-x}N$ (x = 52%) with High Seeding Density	152
Summary	160
VII. CONCLUSIONS AND FUTURE WORKS	162
Conclusions.....	162
Suggested Future Works	163
REFERENCES	166

LIST OF TABLES

Table	Page
1. Physical properties of diamond [2,19,20].	5
2. Semiconductor properties from [42–44].	19
3. Material properties of wide bandgap (WBG) and ultra-wide bandgap (UWBG) semiconductors [46].	23
4. Peak Positions from micro-Raman spectroscopy before and after diamond growth.	127

LIST OF FIGURES

Figure	Page
1.1.(a) Carbon ternary phase diagram (b) Bachmann triangle of C–H–O composition [16].	3
1.2. Diamond crystal structure [16].	4
1.3. Schematic diagram of chemical and physical process during diamond CVD [19].	11
1.4. A schematic diagram of a simplified version of the standard growth model of CVD diamond [19].	12
1.5. Variation in the crystal shape by the growth ratio of (100) face to (111) face [16].	14
1.6. Subdivision of the disordered region near diamond interface with non-diamond substrates [24].	16
1.7.(a) Bandgap versus lattice constant of III-N semiconductors [23]. (b) Band structure of the InAlN/GaN heterostructure.	21
2.1. Schematic representation of HFCVD process for diamond deposition [20].	30
2.2. Different parts of the Hot Filament CVD reactor at Texas State University (a) Computer control system and power supply, (b)-(c) front side of chamber and inside the chamber, (d)-(e) Chamber cooling water loop and Mass flow controllers.	31
2.3. Schematic diagram of an MOCVD reactor system [63].	34
2.4. (a) Dynamic light scattering technique to measure size and zeta-potential of nanoparticles (b) Malvern Zeta-sizer equipment used for this dissertation.	38
2.5. Systematic of electric double layer (stern and diffuse) formed on the surface of charged nanoparticle [68].	40

2.6. (a) Schematic diagram of an AFM system [70] (b) The Bruker dimension ICON AFM at Texas State University.	42
2.7. (a) Schematic view of an SEM chamber [74] and (b) FEI HELIOS Nano Lab SEM at Texas State University.	44
2.8. Schematic diagram of the UV Raman set-up at the optical characterization laboratory, Texas State University [22].	50
2.9. The Lab RAM HR evolution visible Raman system (HORIBA scientific) of ARSC at Texas State University (a) Front view and (b) Backside view.	51
2.10. (a) Basic principle for XPS [84] (b) Nexsa photoelectron spectroscopy at Texas State University.	53
2.11. (a) A schematic diagram of the stylus profilometer measurement set up [87] (b) The Dektak XT stylus profilometer of ARSC at Texas State University.....	55
2.12. (a) Schematic representation of Bragg's law where λ is x-ray wavelength, n is an integer, θ is the incident angle and d_{hkl} is the lattice spacing of the (hkl) crystal plane and (b) Rigaku Smart Lab XRD system at Texas State University.....	56
2.13. (a) Schematic of the Steady-State Thermo Reflectance (SSTR) experiment [84] (b) Texas State SSTR set up.....	59
3.1. Zeta- potential measurement on PDDAC and diamond seeds using dynamic light scattering technique.	64
3.2. Dynamic light scattering data of the diamond nano-particle size distribution in the solution.....	65
3.3. Dip electrostatic seeding approach for diamond seeding on non-diamond semiconductors.	66
3.4. (a) $(5 \times 5) \mu\text{m}^2$ AFM scan from the seeded Si substrate from dip electrostatic seeding approach (b) Line profile from AFM images shown in (a) and (c) Diamond nano-seeds distribution from AFM images measured from scanning probe microscope image processing software Gwyddion.	68

3.5. Modified dip electrostatic seeding approach for diamond seeding on non-diamond semiconductors.	70
3.6. AFM morphology of seeded Si substrate showing variation on nano-diamond seed coverage on Si substrate with different sonication time.	72
3.7. Seeding density variation with sonication time on nano-diamond slurries on (a) Si, (b) AlN and (c) GaN.	73
3.8. (a)-(c) Morphology of Si, AlN and GaN surface respectively prior to diamond seeding (d)-(f). Morphology of Si, AlN and GaN surface after diamond seeding with mixed electrostatic approach with 60 min sonication.	75
4.1. (a) Dynamic light scattering data of particle size distribution in solution. (b) Average diamond seed density based on analysis of at least three AFM images for each sample. Uncertainty ranges are standard deviations from analysis of multiple AFM scans. (c)-(e) AFM images of seeded Si samples S-1, S-2, and S-3, respectively. (f) AFM image of S-3 over smaller range.	82
4.2. SEM images for diamond film grown on sample S-1, S-2, and S-3, respectively after (a)-(c) 30 min (d)-(f) additional 5.5 h (total 6 h) and (g)-(i) additional 10 h (total 16 h). (j) Region with smaller grains seen on S-1 after 6 h.	87
4.3. Average for at least three images of (a) grain size and (b) RMS roughness from AFM scans of diamond film on samples S-1, S-2 & S-3 after 6 h and 16 h growth. (c) Approximate coalescence time and measured thickness for diamond film at the point of coalescence with different seeding density grown with 3% methane. (d) Thickness of diamond film after 6 and 16 h growth taken from cleaved cross section SEM.	90
4.4. (a)-(c) Cross-sectional SEM images for samples S-1, S-2 and S-3, respectively, taken from cleaved samples. The arrows in (a) indicate columnar structure perpendicular to substrate surface. Horizontal dashed lines in (a)-(c) are corresponding thickness of diamond following 6-h growth and additional 10 h at each seeding density. (d) TEM cross-section for S-3 at the diamond/substrate interface.	93
4.5. UV Raman spectra. (a) Diamond film grown on S-3 for 30 min. (b)-(c) Diamond film after 6 h and 16 h growth, respectively.	95

4.6. Analysis of UV Raman spectra, as a function of seeding density, following 6 and 16 h growth. (a) Relative FWHM, (b) ratio of integrated intensities, and (c) relative peak shift and corresponding stress.....	97
4.7. Cross-section micro-Raman spectra of diamond from near-interface with Si (0 μm) to near-growth surface (5 μm) for samples S-1, S-2 & S-3, respectively. (a)-(c) 532-nm visible excitation. (d)-(f) 363.8-nm UV excitation.....	101
4.8. Vertical columns are visible (left) and UV (right) micro-Raman results. (a)-(b) Relative FWHM as a function of distance from Si/Diamond interface for all samples measured by visible and UV Raman spectroscopy, respectively. (c)-(d) Relative diamond intensity ratio as a function of distance from Si/Diamond interface for all samples measured by visible and UV Raman spectroscopy, respectively.....	103
4.9. XPS results for diamond samples (a) Survey scan before and after Ar ion etching for sample S-3 after 30 min growth (b) C 1s fitted XPS spectra for the diamond grown on S-3 for 30 min. (c)-(e) C 1s fitted spectra for samples S-1, S-2 & S-3, respectively after 6 h growth (f)-(h) C 1s fitted spectra for samples S-1, S-2, and S-3, respectively after 16 h growth.....	106
4.10. The correlation of relative diamond volume fraction from XPS (surface) and UV Raman (volume) data for the diamond samples grow for 6 h and 16 h.....	107
4.11.(a) Sample layer stack for SSTR measurements (b) Thermal conductivity variation with thickness and grain sizes for sample S-1, S-2, and S-3.....	109
4.12. Thermal boundary conductance between Diamond-Al and Diamond-Si measured by SSTR.....	110
5.1. Diamond nano-particle signal collected from ATR-FTIR spectra on GaN after nano-diamond solution sonication from 5-60 min.(b) Diamond seed density variation on GaN with different ultrasonication time on nano-diamond slurries and corresponding C=O integrated peak intensity observed from FTIR. (c)-(d) AFM with $(2.3\pm 0.2) \times 10^9 \text{ cm}^{-2}$ and $(3.1\pm 2.3) \times 10^{12} \text{ cm}^{-2}$ seed density on sample S-1 and S-2, respectively.....	116

5.2. SEM images of diamond film grown on sample S-1 (a) after 30 min (b) after 6 h, (c) Focused ion beam (FIB) cross-section SEM image for sample S-1 after 6 h growth. (d)-(e) are SEM images for diamond grown on sample S-2 after 30 min and 6 h respectively, (f) FIB cross-section SEM image for diamond grown on sample S-2 after 6h and (g)-(i) cross-section SEM images for diamond grown on another sample with identical seeding as S-2 from center to edge, respectively.....	120
5.3. (a) HRXRD theta/two theta spectrum for the samples before and after diamond growth and (b) GaN (002) rocking curve for the samples before and after diamond growth.	123
5.4. Ultraviolet (a) and visible (b) Raman spectra taken before and after diamond growth on sample S-1 and S-2. Detailed spectra of E_2^2 (GaN, AlN) and $A_1(\text{LO})$ (GaN) showing phonon shift.....	125
5.5. Visible Raman spectroscopy map of relative FWHM and phonon shift (stress) for (a)-(b) GaN E_2^2 peak, (c)-(d) GaN $A_1(\text{LO})$ peak and (e)-(f) Diamond $O(\Gamma)$, for sample before diamond growth and after diamond growth with low seed density (S-1) and high seed density (S-2).....	128
6.1. (a) $5 \times 5 \mu\text{m}^2$ AFM images before seeding and (b)-(c) after seeding with low seed density $1.1 \times 10^8 \text{ cm}^{-2}$ (S-1) and dense seeding density $2 \times 10^{12} \text{ cm}^{-2}$ (S-2), respectively.	136
6.2. (a)-(b) SEM morphology of diamond film on S-1 and S-2, respectively. (c)-(d) Cross-sectional SEM image for the sample S-1 with low magnification, respectively. (e)-(f) Cross-sectional SEM image for the sample S-1 with higher magnification, respectively taken from cleaved samples.	140
6.3. Average for three images of (a) grain size (b) and RMS roughness from AFM scans of diamond film on samples S-1 & S-2 after 20 h growth. (c) Average thickness measured on samples S-1 & S-2 from cross-section SEM from cleaved samples.	141
6.4. Raman spectra for diamond film after 20 h growth.	143
6.5. (a) Relative FWHM (b) Relative diamond intensity (c) Relative peak shift and stress, as a function of seeding density on the samples after 6 h and 16 h growth.	145

6.6. Map of diamond (a) relative FWHM (b) relative diamond intensity and (c) relative peak shift and stress measurements using visible micro-Raman spectroscopy.....	146
6.7. Visible Cross-section micro-Raman spectra of diamond from near interface with AlN (0 μ m) to near-growth surface (10 μ m) for samples S-1 and S-2, respectively.	149
6.8. Visible micro-Raman results for (a) relative FWHM and (b) Relative diamond intensity as a function of distance from AlN/Diamond interface for all samples.....	150
6.9. (5 \times 5) μ m ² AFM morphology of the Al _{0.52} Ga _{0.48} N sample (a) before and (b) after diamond seeding.	153
6.10. HRXRD θ -2 θ spectrum of the AlGa _{0.48} N/AlN structure on Si (111) before and after diamond growth.	155
6.11. 2 θ - ω scan for Al _{0.52} Ga _{0.48} N sample before and after diamond growth.....	156
6.12. Asymmetric RSM 1014 scan of the Al _{0.52} Ga _{0.48} N/AlN thin film grown on Si (a) before and (b) after diamond growth.....	158
6.13. Cross-section SEM images taken (a) before and (b) after diamond growth , and (c) surface morphology of the diamond film.	159

LIST OF ABBREVIATIONS

Abbreviation	Description
GaN	Gallium nitride
AlGaN	Aluminum gallium nitride
HEMT	High electron mobility transistor
RF	Radio frequency
CVD	Chemical vapor deposition
CTE	Coefficient of thermal expansion
PCD	Polycrystalline diamond
Hz	Hertz
AlN	Aluminum nitride
SiC	Silicon carbide
TBR	Thermal boundary resistance
HFCVD	Hot filament chemical vapor deposition
MOCVD	Metal organic chemical vapor deposition
SEM	Scanning electron microscope
TEM	Transmission electron microscope
UV	Ultraviolet
XPS	X-ray photoelectron spectroscopy
XRD	X-ray diffraction

AFM	Atomic force microscope
PDDAC	Poly (diallyl dimethyl ammonium chloride)
DLS	Dynamic light scattering
SPM	Scanning probe microscope
FWHM	Full width half maxima
DI	De-ionized
FTIR	Fourier transform infrared spectroscopy
GPa	Giga pascal
MBE	Molecular beam epitaxy
RMS	Root mean square
RSM	Reciprocal space mapping
TMA	Trimethylaluminum
TMG	Trimethylgallium
NDC	Non diamond carbon
WDS	Wavelength dispersive spectroscopy
EDS	Electron Dispersive Spectroscopy
CTE	Coefficient of thermal expansion
KCl	Potassium chloride
ACF	Autocorrelation function
RADAR	Radio Detection and Ranging

ABSTRACT

Diamond thin films grown by chemical vapor deposition (CVD) have a wide band gap, high hardness, chemical inertness, and high thermal conductivity, making them an attractive material for a wide range of applications. Due to high surface energy and low sticking probability of diamond, it is difficult to grow thick coalesced diamond films on non-diamond substrates. To deposit diamond film with acceptable surface roughness, desired grain size, and other properties, nucleation enhancement steps through the diamond seeding process are generally required. In this work, an effort is made to improve seeding density, nucleation process, growth kinetics, film morphology, quality as well as material thermal properties of diamond film on different semiconductors. The growth of high-quality diamond on silicon as well as III-Nitrides were achieved through a series of experiments and characterization in various steps of the process.

The first and foremost experiments were conducted to improve the diamond seeding density on silicon and III-Nitride semiconductors. An innovative approach is developed to disperse dense nano-diamond particles by electrostatic van der Waals bonding between the oxygen terminated diamond nanoparticles and a cationic polymer. Then, a systematic study is reported of the effects of nano-diamond seeding densities 4×10^8 , 8×10^{10} and $2 \times 10^{12} \text{ cm}^{-2}$ on silicon wafers on the growth, quality, and morphology of diamond films from sparse to dense range. The growth dynamics, morphology and quality of diamond were found to depend upon the change in seeding density. Diamond

crystals were found to develop three dimensionally via Volmer-Weber (VW) growth into large grains with low seeding density. The transition from VW conditions to van der Drift mode (mostly one dimensional) were found with increasing seeding density on the sample. Diamond crystal quality is found to improve both in the near interface region as well as the growth surface with thickness, at a given seed density, and as density increases. The interface thermal property is improved with increasing seed density on the sample with thermal boundary conductance (TBC) between diamond and Si of 256 ± 32.3 MW/m²K, 292 ± 19.7 MW/m²K, and 318 ± 21.8 MW/m²K, for seed densities 4×10^8 , 8×10^{10} and 2×10^{12} cm⁻², respectively.

This work also investigates the effect of diamond seeding density to achieve direct growth of diamond on epitaxial gallium nitride on silicon substrate. A comparative study is performed for the diamond growth on gallium nitride with low 2.3×10^9 cm⁻² and dense 3.1×10^{12} cm⁻² seed density. It is found that the gallium nitride decomposed and creates pinholes in the growing diamond layer or caused it to delaminate at sparse seed density. The quick diamond lateral coverage during early growth stage help to protect the gallium nitride film from etching at high seeding density. Finally, a comparative study is performed on nucleation, growth, and quality of diamond film on ultra-wide bandgap aluminum nitride at 1×10^8 and 2×10^{12} cm⁻² seed densities. High quality diamond of $\sim 10\mu\text{m}$ thickness is deposited without delamination of the underlying nitride layer. The crystalline quality and diamond phase is found to improve for the diamond film with increasing seed density. The diamond/aluminum nitride interface is seen to be porous

when isolated diamond grains coalesce for diamond growth with lower seeding density. The relative absence of pores or voids is found with high seed density.

At its core, this dissertation develops a fundamental way to deposit high quality diamond on semiconductors with improved nucleation using dense nano-diamond seeding density. Such diamond coating on GaN based high electron mobility transistors (HEMTs) is applicable to solve the self-heating issue on the device.

I. INTRODUCTION

Group III-nitrides have been considered a promising material for semiconductor device applications since 1970, especially for the development of blue and UV light emitting diodes [1,2]. Group III nitride-based semiconductors have enabled processing wide bandwidth and high breakdown voltage simultaneously due to their high electron velocity, high two-dimensional electron gas (2-DEG) and large breakdown field. More recently, AlGaN/GaN-based transistors for terahertz (THz) emitter and detector have been reported that can operate from 0.75 THz to 2.1 THz [3–5]. Furthermore, the switching speed for AlGaN/GaN HEMTs grown on silicon are reported to have as high as ~150 GHz and power densities can exceed 12W/mm under harsh operational conditions [6,7].

The maximum RF power densities for GaN based HEMTs reported to date is 41.4 W/mm at 4 GHz frequency [8]. However, the commercially available HEMT is working only at 5-6 W/mm. This massive gap in the performance is due to power loss upon self-heating in the device, which causes the degradation of power added efficiency resulting in device failure. Due to the band offset between GaN and AlGaN in GaN based material heterostructures, a large spontaneous and piezoelectric effect arises resulting in a 2-D electron gas (2-DEG) induced at the AlGaN/GaN interface without any doping [9]. The 2-DEG and active GaN/AlGaN layer are very thin and the heat dissipation from the self-heating source is dominantly vertical. Therefore, a low resistant thermal pathway from the self-heating source to a nearest heat sink (high thermal conductive substrate) is very much desired. One solution to this is to attach the device to a high thermal conductivity diamond which can rapidly transfer the localized heat to an external cooling system or

radiator.

Chemical vapor deposited (CVD) polycrystalline diamond has emerged as a promising substrate solution for GaN HEMTs due to its high thermal conductivity (800-2000 W/m K) [10,11]. Due to the polycrystalline nature of CVD diamond, historically, it is either attached with, or grown on, the backside of the GaN HEMT structure [12,13]. In both cases a low thermal conductive dielectric layer is employed as an adhesion layer [14]. Although GaN-on-diamond have demonstrated three times better thermal performance than any other substrate, the full advantage of diamond substrate has not been achieved due to this poor dielectric adhesion layer and excessive thermal boundary resistance associated with it [14]. Compounding the problem, another limiting factor associated with CVD diamond is its poor thermally conductive graphitic content nucleation layer which impedes efficient thermal conduction [11,15,16]. Addressing the issue related to the thermal resistance between the device active region and heat sink is important to achieve the full advantage of GaN-on-diamond devices.

The purpose of this dissertation is to minimize the above-mentioned problems arising during the heterogenous integration of diamond film on non-diamond substrate. For this, an innovative approach for electrostatic diamond seeding technique is developed in this dissertation work to improve the diamond nucleation process, quality and interface between the diamond and non-diamond substrates. This approach gives precise control over nano-diamond seed density from sparse $\sim 10^8 \text{ cm}^{-2}$ to dense $\sim 10^{12} \text{ cm}^{-2}$ range. Using Si as a test base, the seeding and growth mechanism of CVD diamond is studied with different seeding density from sparse to the dense range. Later, this seeding approach is used on different III-nitride semiconductors, AlN, GaN and Al (Ga)N, to improve the

diamond film quality and interface properties. The improved seeding density on different semiconductors followed by improved materials and interface properties between diamond to non-diamond substrate is presented in this work. The outcome of this research is important to improve the power efficiency and lifetime of GaN-based power electronic devices and other optoelectronic devices. The physical properties including optical and thermal properties is studied. Extensive characterization for the diamond film is performed using state of art characterization techniques such as atomic force microscope (AFM), micro-Raman spectroscopy (UV and visible), scanning electron microscopy (SEM), transmission electron microscopy (TEM), x-ray photoelectron spectroscopy (XPS), steady state thermo reflectance (SSTR) measurements and x-ray diffraction (XRD). A discussion on diamond and group III-nitrides will be presented in the next sections along with research motivation and proposed solution. Detailed organization of this dissertation will be presented at the end of the chapter.

Diamond

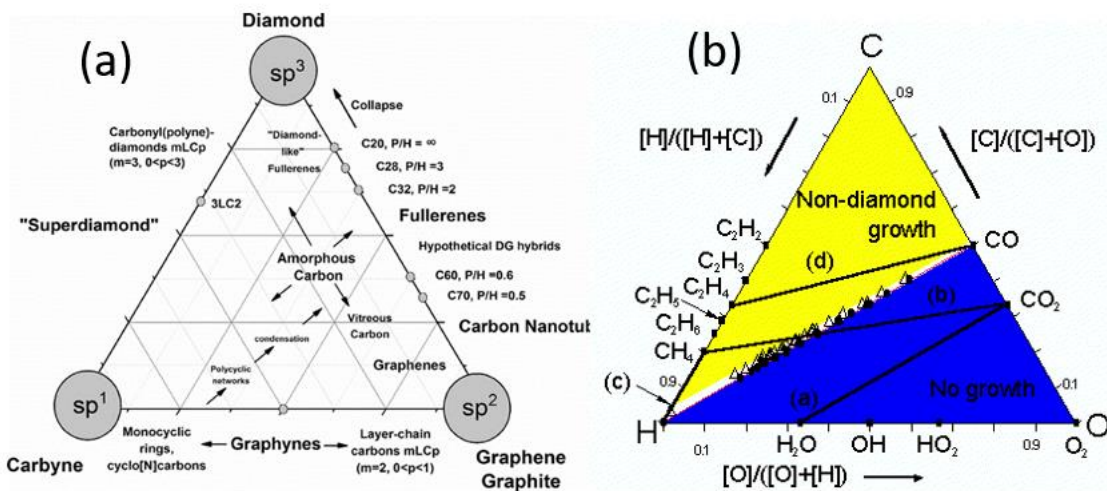


Figure 1.1.(a) Carbon ternary phase diagram (b) Bachmann triangle of C–H–O composition [16].

Carbon is the fourth most abundant element in the universe and has three relatively well-known allotropes amorphous carbon, graphite, and diamond [17]. The family of carbon-based materials has grown substantially since the middle of last century. The possible forms of carbon through sp^1 , sp^2 , sp^3 hybridization of its valence configuration provides a wide range of possible carbon forms [18]. The most widely accepted equilibrium carbon structures, based on hybridization, originate from the work of Heimann et al [17]. The first ternary phase diagram is shown in the Figure 1.1(a). The three main vertices of the diagram are defined by the hybridization states, while the interior of the diagram represent the materials processing in a mixture of respective hybridizations [17]. The classification uses sp^n groups for allotropes owning mixtures of hybridizations. Such groups have ‘n’ hybridization, which is defined as being ($1 < n < 3$). The number of different carbon allotropes is extensive, including the well-known materials, diamond, graphite, graphene, carbon nanotubes, fullerenes, amorphous carbon, and many others.

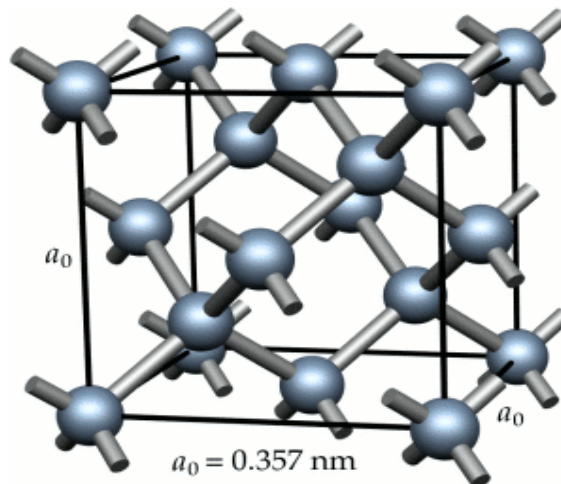


Figure 1.2. Diamond crystal structure [16].

Table 1. Physical properties of diamond [2,19,20].

Properties	Value
Bandgap(eV)	5.45
Lattice constant(nm)	0.35
Thermal conductivity ($\text{Wm}^{-1}\text{K}^{-1}$)	2200
Breakdown strength (MV/cm)	~10
Young modulus (GPa)	1140
Electron mobility (μ_e), cm^2/Vs	4500
Hole mobility(μ_h), cm^2/Vs	3800

The applications of diamond in industry are very well known. At standard temperature and pressure, it is a metastable form of carbon, and as such, it is not formed at the surface of the earth. Graphite is the thermodynamically stable allotrope of carbon at standard temperature and pressure. Their standard enthalpy differs by just 2.9 kJ/mol, but an activation barrier separates the two phases from spontaneous conversion [21]. So, diamond is a metastable form of carbon which is kinetically stable but not thermodynamically. The crystal structure and chemical bonding of diamond has made diamond an outstanding choice for many applications because carbon is the smallest atom that form a three-dimensional network of covalent bonds. Diamond crystals can be viewed as two interpenetrating face centered cubic lattices shifted along the body diagonal by $(1/4, 1/4, 1/4) a$, where a is the lattice constant [20], as shown in Figure 1.2. Each carbon in diamond lattice consists of sp^3 hybridized atomic orbitals. Four covalent bonds from each carbon atom makes up three-dimensional lattice in which each of their outer four electron is shared with electron of four neighboring carbon atoms resulting in the formation of the diamond lattice. Diamond has some outstanding physical

properties, listed in Table 1.

Worldwide interest on diamond has been further increased by the more recent discovery that polycrystalline diamond can be grown by a wide variety of chemical deposition process using methane gas in excess of hydrogen. Mechanical, tribological, and even electronic properties of CVD diamonds are identical to those of natural diamond. [18,20]. There are various processes for the deposition of CVD diamond. Most common techniques are filament assisted chemical vapor deposition, plasma enhanced chemical vapor deposition, combustion assisted chemical vapor deposition and so on [20].

Chemistry of CVD Diamond Deposition

The CVD diamond use carbon containing gases (most commonly methane) and molecular hydrogen, breaks, activated and ionized by means of an energy source (e. g. hot filament or electric discharge). The carbon containing gas precursor and molecular hydrogen are dissociated passing through the activation region, forming carbon reactive radicals and atomic hydrogen, which diffuse towards the substrate surface by a gradient in temperature and concentration [21]. The reactive species undergo a complex set of chemical reactions prior to reaching the substrate surface, where they can either adsorb and react with the surface, desorb back into the gas phase, or diffuse until an appropriate reaction site is found [22]. If a surface reaction occurs, carbon is left on the surface, in the form of both diamond and graphite. However, due to the different reaction rate between atomic hydrogen/graphite and atomic hydrogen/diamond, deposition of the diamond phase is favored; in fact, in the right conditions, atomic hydrogen etches graphite at a faster pace than diamond, hence leading to a build-up of diamond [23]. Apart from

etching the graphitic sp^2 carbon during diamond deposition, atomic hydrogen is also responsible for tying up the carbon dangling bonds until it gets available carbon to form tetrahedral structure and minimize the formation of graphitic phases [18].

The great complexity of gas phase reaction during CVD diamond growth can be understood by means of the C-H-O composition diagram known as Bachmann triangle diagram [20,21], as shown in Figure 1.1(b). It shows that the diamond grows only when the gas composition is close to the CO line, and it is independent of the deposition system or gas mixture [21]. Of particular interest is a small region at the lower left corner of the diagram, along the CH line, representing gas mixtures, where methane is highly diluted in hydrogen and no oxygen is present [18]. This is indeed the most common gas mixture used in CVD diamond growth, comprising solely CH_4 and H_2 , with methane/hydrogen ratios usually between 0.1% and 3% by weight according to the activation method adopted and to the kind of polycrystalline diamond (PCD) film one aims to deposit (with respect to crystalline structure and concentration of graphitic phases embedded in the film).

Nucleation sites through seeding. The diamond growth process on a foreign substrate generally contains two distinct phases; a diamond seeding, during which the diamond crystallites are embedded on the substrate to act as a seed for the subsequent growth cycle and the actual growth [23]. Seeding step is essential for the CVD process in the deposition of diamond with less graphitic and amorphous carbon. It also has significant impact on the microstructure of the polycrystalline diamond film. Diamond seeding can be achieved by several methods. When using Si as a substrate, a common technique consists of mechanically scratching the substrate surface with a powder of

hard, μm -sized particles like sapphire, SiC or diamond; as the particles scratch the surface they break down into smaller fragments, which stick onto it. While with such a method high seeding density can be reached, the mechanical abrasion damages the substrate by creating a rough surface with μm -sized pits and defects. This method is therefore unsuitable for those diamond applications in which the substrate surface should be preserved, either because it hosts electronic devices whose circuit geometries are on a sub-micrometer scale, or because a high surface roughness is detrimental for the thermo-mechanical properties of the interface between the diamond film and the substrate.

Apart from mechanical scratching, many other seeding techniques such as photolithography, bias enhanced nucleation, ultrasonic polishing, etc. have also been used successfully [24,25]. It is important to know that different seeding densities greatly affect thermal conductance at the interface [26]. Lower seeding density can create voids at the interface, while overly high seeding densities can create extremely small grains near the nucleation region that do not allow for coalescing into the high-quality columnar grain structure that is desired for efficient thermal conduction [26]. The seeding procedure varies according to the carrier, in which the nanoparticles are dispersed, which can be either a liquid (water or isopropanol), a gel, or a slurry. Photoresist and polymer-based seeding process are also reported [27,28]. These polymers / photoresists convert into carbon during the diamond growth process and the nano seeds dispersed therein act as the nucleation sites for the diamond growth.

Typically, a high concentration of diamond nuclei on the substrate is desired prior to diamond deposition to achieve a denser diamond film with high growth rate with better mechanical and optical properties, fewer defects, and smoother surface. The nucleation

stage differs from the diamond growth stage and depends upon the nature of the substrate and/or diamond seeding [29]. Diamond has a high surface energy and low sticking probability, so it is not readily nucleated on smooth surfaces such as silicon [29]. The nucleation of diamond typically includes the following steps:

Step I – Formation of carbon clusters

Carbon clusters are formed on the substrate surface due to the constant atomic hydrogen bombardment, causing a change in local thermal conditions. Thereby, there is a change in carbon structure from sp^1 to sp^2 .

Step II – Conversion of sp^1 to sp^2 and then to sp^3 bonding

Molecular bombardment of activated hydrocarbon and atomic hydrogen gives the substrate sufficient energy to transform sp^2 bonded carbon into sp^3 . Atomic hydrogen promotes this reaction and stabilizes the sp^3 phase. Etching of all three carbon phases (sp^1 , sp^2 , and sp^3) is taking place at the same time. However, the etch rate of the less stable sp^1 and sp^2 phases is ten times faster than etching the sp^3 phase [29].

Step III – Crystallization of amorphous phase

For crystallization to occur, the carbon bonding undergoes a transition stage from sp^2 bonded carbon, to disordered domains with sp^3 bonded carbon and finally to sp^3 bonded carbon. Carbon atoms must rearrange themselves during the crystallization process to acquire minimum surface energy. This rearrangement should favor (111) crystallographic orientations since (111) orientation has the lowest surface-free energy in the diamond crystal. The crystallized region becomes a nucleus for subsequent diamond growth.

For the non-diamond substrate, the nucleation stage can be divided into several sub-stages: (a) Incubation period, (b) 3D surface nucleation, (c) termination of nucleation and 3D growth of nuclei to grains, and (d) faceting and coalescence of individual grains and formation of continuous films [30]. The diamond nucleation can happen on the non-diamond substrate if the substrate surface is saturated with carbon and high energy sites such as active vacancies, dangling bond, and active sites are present.

Diamond growth. During diamond growth, a complex physical and chemical process occurs during chemical vapor deposition as shown in Figure 1.3. Before diffusing toward the substrate surface, the process gases must first mix in the chamber. They pass through an activation region e.g., a hot filament, which provides energy to the gaseous species [21]. This activation causes molecules to fragment into reactive radicals and atoms, create ions and electrons, and heat the gas up to temperatures reaching a few thousand Kelvins. Beyond this activation regions, these fragments continue to mix and complete a complex set of chemical reactions until they strike the substrate surface. The gaseous species either adsorb and react with the surface, desorb again back into the gas phase, or diffuse around close to the surface until an appropriate reaction site is found [22,23]. If surface reaction occurs, one possible process, if all conditions are suitable, is the growth of diamond.

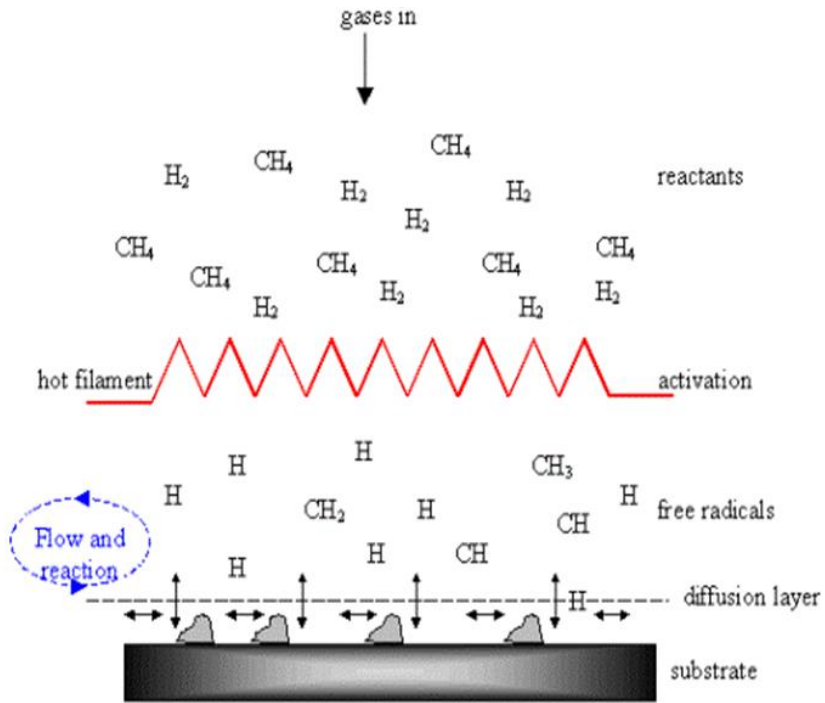


Figure 1.3. Schematic diagram of chemical and physical process during diamond CVD [19].

Many theories have been proposed to describe the growth of diamond after nucleation. The most accepted theory for diamond deposition described by Paul May [21] is shown in Figure 1.4. After the nucleation process, the growth process can begin by saturating the surface with hydrogen. Atomic H attracts a surface H to form H_2 leaving behind a reactive surface site. The site will most likely react with a nearby H atom, returning to the original structure. However, a CH_3 radical may react with the surface site, which adds a carbon atom to the lattice. This process occurs continuously as the diamond growth continues as shown in Figure 1.4. This is a stepwise addition of carbon atoms to the already existing diamond lattice, catalyzed by the presence of excess atomic hydrogen.

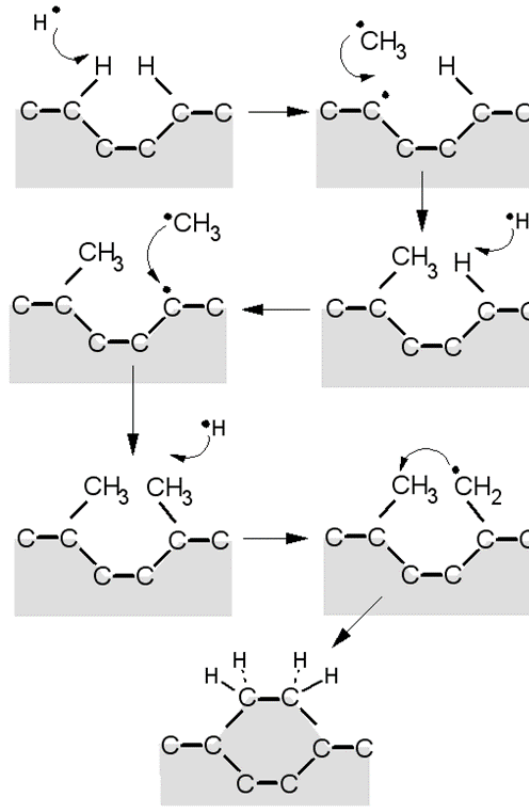
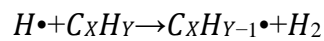


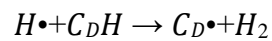
Figure 1.4. A schematic diagram of a simplified version of the standard growth model of CVD diamond [19].

The generic model [29,31] which describes the formation of diamond is well known through the following set of equations:

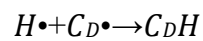
i. Formation of free radicals,



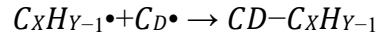
ii. Hydrogen adsorption from activation site (C_D)



iii. Addition of hydrogen to the diamond surface

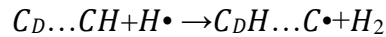


iv. Addition of hydrocarbon radicals to the diamond

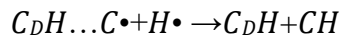


The surface bonds are initially hydrogen terminated, followed by hydrogen absorption with the addition of hydrogen or hydrocarbon radicals on the diamond surface. The replacement of hydrogen in the diamond surface is more than the addition of hydrocarbon radicals on the activated diamond sites [31]. The sequence of reactions (i)-(iv) leads to the addition of radical hydrocarbons to the surface [32]. The process of chemisorption of newly added hydrocarbon species to the adjacent terminated diamond site ($C_DH\dots CH$) happens through the process of hydrogen removal and rearrangement of added hydrocarbon atoms.

v. Hydrogen adsorption from the adjacent diamond site,



vi. Hydrogen addition to the adjacent diamond site,



vii. Hydrogen adsorption from the diamond site and formation of new carbon to carbon bond,



The most used process gasses include hydrogen/methane, argon/methane, or hydrogen/argon/methane [18]. The reaction rates depend upon the concentration of atomic hydrogen species. Hydrocarbon species supplies the necessary carbon atoms for the diamond formation during the diamond synthesis from the gas phase. Argon is often used as the main atmosphere volume with a small hydrocarbon gas concentration, or

combination with a small amount of hydrogen. The effect of an argon rich atmosphere is like the effect of increasing hydrocarbon gases within the system or lowering the plasma density. They all lead to lowering the size of diamond grains within the nanoscale regions [16,18].

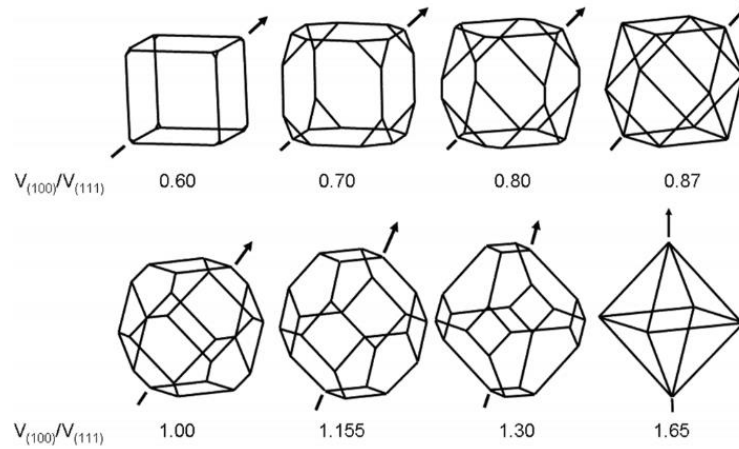


Figure 1.5. Variation in the crystal shape by the growth ratio of (100) face to (111) face [16].

The surface morphology of the diamond film obtained during CVD depends upon the various process conditions, especially the gas mixing ratio, which determine the value of the α -parameter, described by Wild and coworkers [33–35]. They first systematically investigate the way diamond crystals are arranged polycrystalline diamond film and correlate the microstructure which develops with the film thickness to the growth parameters. They introduce the α -parameter to characterize the outgrowth velocity dependence of the crystal orientation which define the growth rates on {100} and {111} faces:

$$\alpha = \sqrt{3} \frac{V_{100}}{V_{111}} \quad (1)$$

Also, the value of the α -parameter describes the shape assumed by a single diamond grain, as it changes from the cubic($\alpha=1$), to octahedral($\alpha=3$), shown in Figure 1.5.

Diamond thermal properties. Heat transport in material is generally found to be governed by particle-interaction mechanism which endeavors to restore thermodynamic equilibrium subjected to a temperature gradient. The thermal conductivity of diamond is governed by the lattice conductivity of phonon scattering. Due to the relatively low mass of carbon and strong carbon-carbon covalent bond, the phonon can easily pass, and carbon atoms do not interfere with the thermal waves. Therefore, diamond has maximum reported thermal conductivity in the range of 2000-2300 Wm⁻¹K⁻¹ at room temperature. Diamond thermal conductivity is different for single crystalline and polycrystalline structures.

The heterogenous integration of diamond film on non-diamond substrate results in a polycrystalline diamond film in which diamond crystals are embedded into a grain boundary matrix. According to the theory of lattice thermal conductivity, phonon scattering at the grain boundaries, defects, dislocation and impurities will limit the phonon diffusion length in such a material in a wide temperature range (0-500 K) [22,23]. Thus the thermal properties of the polycrystalline may differ from the properties of the single crystalline counterpart and may vary significantly according to the thickness of the film, shape, size and arrangement of the diamond crystallites (i.e. grains), as well as to size, orientation and composition of the grain boundaries. Columnar diamond crystal structure has reported the highest thermal conductivity [36–38]. Thermal properties on the diamond film are thus thickness dependent and anisotropic, with a different conductivity for the heat flowing perpendicular to the growth direction (the in-

plane thermal conductivity) and for heat flowing parallel to the growth direction (the cross-plane or out of plane) conductivity.

Film/substrate interface properties and thermal boundary resistance. A major contribution to the thermal boundary resistance of polycrystalline diamond films comes from the nucleation layer near the interface with the substrate. The thickness of such interface layer is <10 nm where the diamond crystallites bond to the surface and nucleate. Due to the disordered microstructure and fine-grained microstructure, there's high phonon scattering, contributing to the rise in total thermal boundary resistance [26,39]. The nucleation density, nucleation method, and grain dimension near the interface, all play a key role in the structure and thickness of such a nucleation layer, moreover as its bound resistance with the substrate[24].

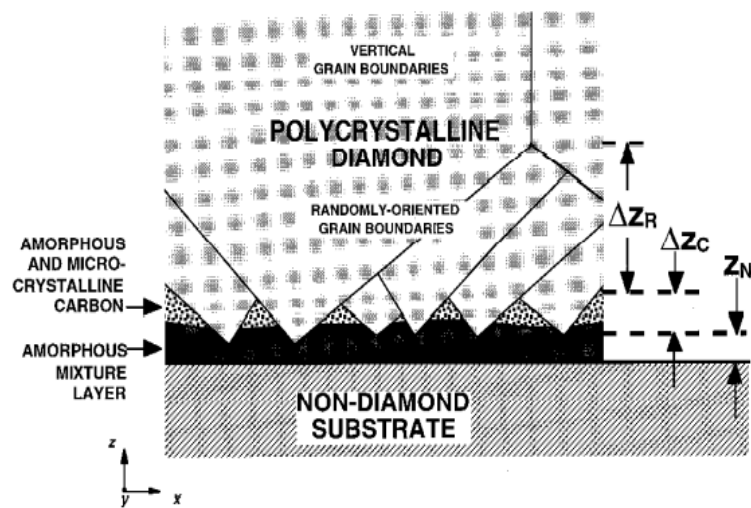


Figure 1.6. Subdivision of the disordered region near diamond interface with non-diamond substrates [24].

The nucleation density is an important factor in determining the diamond-substrate interface resistance [26]. Figure 1.6 shows the impact of nucleation density on the interface resistance at different depths within the diamond film. It shows that the initial diamond growth regime of an amorphous layer of mixed stoichiometry of thickness comparable to $Z_N \sim 50 \text{ \AA}$. The layer consists of nanocrystalline and nanocrystalline combination of carbon and substrate atoms. These layers are important for the nucleation. As the layer grows, an increasing fraction of incident atoms remain at the surface, forms clusters, and provide nucleation sites for diamond grains. In the second region, $Z_N < Z < Z_N + Z_C$, the nucleated grains grow in lateral dimension, with increasing distance from the substrate. The region between grains is filled with amorphous and graphitic carbon, increasingly dominated by sp^3 carbon with increasing Z . The thickness Z_C depends on the nucleation density and the crystal growth angle. This angle describes the departure of opposing grain walls from one another with increasing Z and is approximately 90° for grains with $\{100\}$ orientation. In the third region, $Z > Z_N + Z_C$, the grains cannot continue to grow freely in the lateral dimension. Some of the grains terminate, while others grow larger. The resulting orientation of grain boundaries is practically random. While the thermal conductivity of this region is considerably larger than that of the regions below the closure height, which contains amorphous material, it is much less than that of bulk diamond because of the small grain size [26].

It is reported that higher nucleation density results in lower thermal resistance [26]. The size of the grains at the interface depends on the nucleation density and initial size in turns depends on the subsequent development of the columnar structure. With a high seed density and a smaller diamond film thickness during the early

growth regime, a continuous diamond film at the shortest distance from the interface is preferable, which minimizes phonon scattering and allows for faster lateral column development. But a low nucleation density can lower the direct contact area between diamond crystallites and the substrate, as well as increase the volume percentage of amorphous materials near the interface, increasing the final thermal boundary resistance.

Stress in diamond film. Residual stress is one of the key aspects of a diamond coating as it influences the stability of the film on the non-diamond substrate. The residual stress is normally composed of thermal stress and intrinsic stress [40,41]. The thermal stress is caused by the difference between the coefficient of thermal expansion between the diamond film and substrate material during diamond deposition. Depending upon the nature of the substrate, the thermal stress generated within the diamond film may be compressive ($\sigma < 0$) or tensile ($\sigma > 0$). Most commonly, the substrate coefficient of thermal expansion (CTE) is much larger than the diamond film, so the diamond film prefers to shrink more after post growth cooling and thus a large compressive stress builds within the diamond film. The intrinsic stress is generally caused by the structural defects associated with the interfacial mismatch between the film and the substrates [41]. The overall stress on the diamond film depends on the growth temperature, gas flow rates, structural and morphological characteristics of the film.

Wide Bandgap Electronics

An ideal semiconductor for power applications should have properties like a high breakdown voltage, excellent thermal transport properties, high thermal conductivity, chemical inertness and mechanical stability. These semiconductors should allow for the fabrication of both unipolar and bipolar devices with low parasitics [23]. Said properties

of commercial wide band gap semiconductors compared to Si and GaAs are shown in Table 2.

Table 2. Semiconductor properties from [42–44].

Property	Si	GaAs	GaN	4H-SiC
E_g (eV)	1.12	1.4	3.4	3.3
ϵ_r	11.8	12.8	9.5	10.0
μ (cm ² /V. s)	1400	8500	1200	900
E_{Br} (MV/cm)	0.3	0.4	5.0	3.0
ϑ_{sat} (10 ⁷ cm/s)	1.0	2.0	2.5	2.0
K (Wm ⁻¹ K ⁻¹)	150	50	130	340

Most power devices today in the market are made from Si and GaAs, and as these materials reached their performance limits, they are being replaced by wider band gap material such as SiC and GaN. The shift can be understood by comparing the various properties between the wide band gap semiconductors with Si and GaAs, shown in Table 2. The band gap of GaN and SiC is almost three times larger than Si that makes them more suitable for high power and high temperature electronics. Hence power devices fabricated with wideband gap materials can tolerate the harsh, hot environment with less cooling issue [45,46]. Furthermore, with a wide band gap comes a high breakdown field, which scales roughly with the square of the energy gap [46]. Therefore, those power devices which has a vertical device structure, can be made thinner than the Si-based counterparts and have a smaller resistance of the drift region when based on wide bandgap semiconductors.

GaN is one of the most important semiconductors among the wide bandgap's materials because of its extraordinary electronic properties such as good mobility, high saturation drift velocity, hence making this material very promising for microwave devices. The devices made of GaN could be switched at higher frequencies, almost double, compared to the device fabricated from Si. Moreover, a higher drift velocity allows faster charge removal and shorter recovery times for power diodes [47].

SiC has a thermal conductivity almost three times compared to Si and nearly one order of magnitude greater than GaAs. High thermal conductivity is important for the thermal management of electronic devices. Although bulk GaN has similar thermal conductivity as Si [48,49], the hetero-epitaxial layers used in the actual device include defects, doping and oxygen impurities, which reduces the heat transport capabilities and make them comparable to GaAs. GaN supports a heterostructure technology compared to SiC when alloyed within the III-nitrides material system. Quantum wells, modulation-doped heterointerface, and heterojunction structures can all be made with III-nitrides, thus leading to new device concepts for electronic applications.

III-Nitrides Heterostructures

Group III nitride comprises AlN, GaN, InN and their ternary and quaternary alloys, which are all wide band gap materials and can crystallize in both wurtzite and zinc blende crystal structure. In wurtzite crystal structure for GaN, AlN and InN, these materials have direct bandgaps of 3.4, 6.2 and 0.7 eV, respectively [46]. They are polar materials and have high electronegativity with the nitrogen atoms inside the crystals. The direction of the polarization depends on the crystal orientation and its polarity [1].

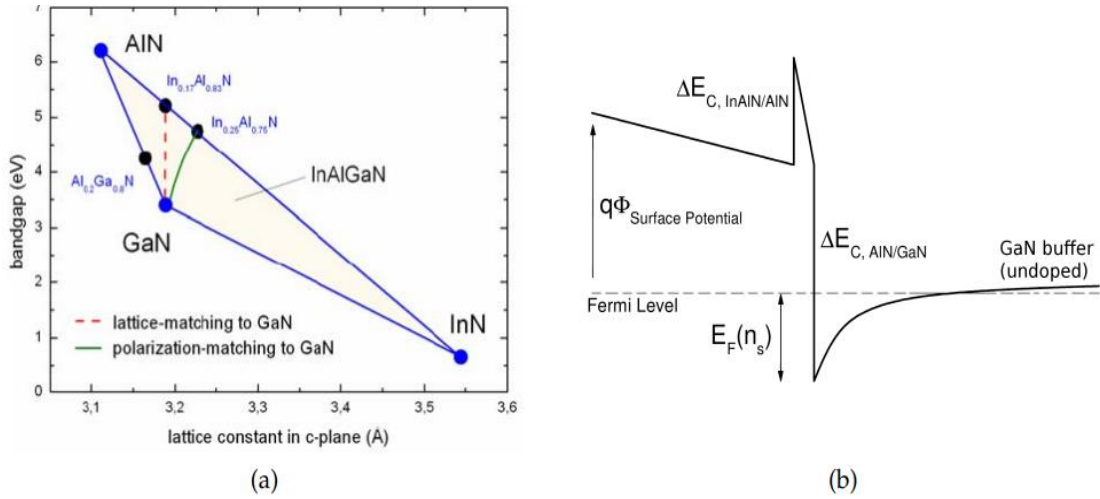


Figure 1.7.(a) Bandgap versus lattice constant of III-N semiconductors [23]. (b) Band structure of the InAlN/GaN heterostructure.

The diagram of bandgap versus lattice constant for the III-nitrides system with wurtzite lattice taken from [23] is shown in Figure 1.7(a). The most common heterostructure in this system consist of a ternary alloy, the “barriers layer”, grown on top of a relaxed GaN buffer layer, with the interface between the two being the channel. There are two distinct polarizations between these two at the boundary; spontaneous polarization between GaN/barrier and piezo-electric polarization induced by the strain due to lattice mismatch, give rise to an electrically charged region [1]. Due to band offset and conduction band discontinuity between these two semiconductors, the electron (holes) diffusing into the ternary alloy into the GaN buffer layer are confined in the 2-dimensional confined quantum wells at the interface. This 2-dimensional electron gas (2-DEG) has very high mobility that can be exploited to fabricate lateral conduction devices. A common barrier layer used in these heterostructures of III-nitrides is an alloy of $\text{Al}_x\text{Ga}_{1-x}\text{N}$, which has larger bandgap than GaN. A schematic representation of band

structure for GaN/InAlN heterostructure is shown in Figure 1.7(b). Typically, a 20-30 nm AlGa_N layer is grown on top of GaN with an Al content between 20-30 % to limit the tensile stress induced due to lattice mismatch with GaN. Such Al-content AlGa_N as a barrier layer in GaN/AlGa_N HEMTs produce spontaneous polarization in the heterointerface which induces a large carrier charge density in the 2-DEG channel and produces very high output current densities.

Ultra-Wide Bandgap Semiconductors

The ultra-wide bandgap semiconductors include AlGa_N/AlN, diamond, Ga₂O₃ and cubic BN, which have bandgap significantly wider than the 3.4 eV of GaN; in the case of AlN as wide as ~6 eV. Ultra-wide bandgap materials have the potential for far superior performance than the conventional wide bandgap semiconductors. These materials have higher Baliga figure of merits (BFOM) ~34 and band gap of nearly two times that of conventional wide bandgap semiconductors [50]. So, these semiconductors have significantly better performance compared to other wide band gap materials. The materials properties of ultra-wide bandgap semiconductors compared to the wide bandgap semiconductor, are shown in Table 3.

Table 3. Material properties of wide bandgap (WBG) and ultra-wide bandgap (UWBG) semiconductors [46].

Material	WBG		UWBG		
	GaN	4H-SiC	AlGaN/AlN	β -Ga ₂ O ₃	Diamond
Bandgap (eV)	3.4	3.3	Up to 6.0	4.9	5.5
Thermal Conductivity (W m ⁻¹ K ⁻¹)	253	370	253–319	11–27	2290–3450
State-of-the-art substrate quality (dislocations per cm ²)	=10 ⁴	=10 ²	=10 ⁴	=10 ⁴	=10 ⁵
State-of-the-art substrate diameter (inches)	8 (on Si)	8	2	4	1
Demonstrated p-type dopability	Good	Good	Poor	No	Good
Demonstrated n-type dopability	Good	Good	Moderate	Good	Moderate

AlGaN alloys are ultra-wide bandgap semiconductors with outstanding fundamental properties. From an electronic prospective [46], they have (1) direct bandgaps spanning a wide range (3.4 to ~6 eV), (2) high breakdown fields (> 10 MV cm⁻¹ for AlN), (3) high electron mobility (bulk mobility up to 1000 cm² V⁻¹ S⁻¹), (4) high saturation velocity up to 10⁷ cms⁻¹, and (5) relative ease of n-type doping with Si, which has relatively small donor ionization energy up to ~80-85% Al content. AlGaN has the same crystal structure as InGaN. Thus, it can take the advantage of replacing the InGaN for the applications in the field of optoelectronic devices such as light emitting diodes (LEDs). However, there are several challenges associated with growth of AlGaN alloys such as difficulties to control over doping, absence of available single-crystal substrate with quality necessary for epitaxial growth and the immaturity of the scientific understanding required for the control of heteroepitaxy on such substrates.

Research Motivations

As the size of the electronic devices become smaller and more powerful, the main issue is ever greater difficulty managing the heat. Almost 50 % of electronic failure occur because of heat related issues [51]. So, there is the need for advanced thermal management solutions. This is particularly crucial for gallium nitride (GaN) based RF devices which is used in mobile base stations or RADAR, where the thermal obstacles have limited the ability to achieve GaN's intrinsic performance potential [52]. GaN based devices basically produce heat in extremely small and concentrated areas and create higher operating temperature which negatively impact the device power performance and endurance. Also, the average device lifetime can be degraded if the heat is not removed properly from the device active channel. So, proper thermal management is necessary to gain full advantage of these devices on electronic applications. One possible way to reduce temperature on GaN devices is integration of high thermal conductivity materials such as diamond near the device active region. Owing to the outstanding bulk thermal conductivity of diamond, chemical vapor deposition polycrystalline diamond is a superior choice for a heat spreading material compared to common GaN-based substrates such as Si, 6H-SiC, and Al₂O₃ [53]. It has been found that GaN/diamond has ~ 2.7× reduction in the thermal resistivity and 3× increase in device areal density compared to the GaN device fabricated on SiC substrates [54].

Synthetic diamond has a thermal conductivity that is more than five times higher than the best metal's values [55]. Diamond has other properties such as mechanical stiffness, chemical inertness and low density which are also very desirable in applications in diverse environments. CVD diamond has shown substantial value as a heat spreader

due to its status as the highest known thermally conductive material, low density and low thermal expansion coefficient. Since diamond has a thermal conductivity almost four times higher than copper, these heat spreaders enable support of larger mechanical and thermal load in thermal management applications, enabling system operation at elevated temperatures, enhanced heat removal capability and, crucially, reduced overall system cost [56]. Diamond's exceptional thermal conductivity and electrically insulating properties make it an ideal choice to reduce thermal resistance in a variety of electronic applications. CVD diamond is available in different grades with thermal conductivity ranges from 1-2200 W/mK [57,58]. Also, CVD diamond is isotropic in nature, which enables enhanced heat spreading over all the directions diamond can be grown with tightly controlled growth conditions which enables chemical impurities and enhanced various properties of diamond materials. The production of such highly consistent materials with predictable properties and behaviors enables the diverse range of applications, including heat spreaders for high power and high frequency applications.

Research Problems and Solution

The motivation behind this dissertation project is to utilize the tremendous thermal conductivity of diamond on III-Nitride-based devices. But there are several challenges and problems associated during heterogenous integration of diamond on non-diamond semiconductors. For better thermal management, diamond should have superior crystal quality, reduced defect density as well as superior thermal conductivity. Also, the interface thermal boundary conductance should be maximized. Thermal boundary conductance (TBC) is a measure of the ability of a material to transfer heat per unit time, given one unit area of the material and a temperature gradient through the thickness of

the material [59]. Mathematically, it is given as; $TBC = \frac{Q}{A\Delta T}$, where Q is heat flow across an interface, A is the area that the heat is passing through, and ΔT is the temperature difference between the two sides of the interface.

Graphitic content in the diamond nucleation layer during growth of diamond on non-diamond substrate is one of the challenges faced during integration of diamond on non-diamond substrates. As previously discussed, diamond grows via a nano-crystalline phase through a complex nucleation process where diamond seed grows laterally and vertically to develop into the thicker film. Not all diamond seeds participate in the diamond nucleation process to develop into the diamond nuclei or some of them have their growth terminated during the early nucleation phase. Such underdeveloped diamond seeds may be the source of the non-diamond carbon or graphitic phase. Also, the diamond growth mechanism depends on the number of available nucleation sites during the early growth stages. Such nucleation sites are provided through nano diamond seeding prior to diamond growth. Poor diamond nucleation with low seed density may cause voids near or at the diamond-semiconductor interface [39]. Such voids may be a possible source for non-diamond carbon. In a recent study, Nazari et. al. [60] reported 10% disordered carbon or diamond like carbon (DLC) in diamond at the GaN-diamond interface where average particle size was less than 20 nm. These non-diamond carbon phases have very low thermal conductivity and create significant thermal impedance for GaN on diamond devices [61].

In order to minimize the challenge associated with the graphitic content during diamond growth on non-diamond substrates, this dissertation effort is aimed to improve the diamond nucleation process by introducing an innovative electrostatic diamond

seeding approach. This approach can achieve the diamond seeding density on any generic semiconductor substrates $>10^{12} \text{ cm}^{-2}$. Also, precise control over the diamond seed density from sparse to dense range can be achieved through this approach. The following advantages are expected with integrating diamond film with this dense seeding approach:

- i. Diamond coalescence will occur via quick lateral coverage during the diamond nucleation period. Such a thinner diamond film due to quick lateral coverage helps to minimize the non-diamond carbon phase near the diamond-semiconductor interface.
- ii. Dense diamond seeds provide more nucleation sites for the diamond growth with improved diamond nucleation. Diamond grains with desired grain sizes, minimum surface roughness and less defects can be grown with dense diamond seeding.
- iii. Less voids and spaces between the diamond grains near or at the interface can be achieved with dense diamond seeding density. Reduced non-diamond carbon, diamond like carbon and amorphous carbon will increase the thermal boundary conductance (TBC) between the diamond-semiconductor interface as well as the thermal conductivity of resultant diamond film.

Dissertation Outline

The first half of this dissertation project encompassed significant effort in the optimization of diamond seeding density on Si substrate. Optimization of an electrostatic seeding approach to achieve seeding density from the range 10^8 cm^{-2} to $>10^{12} \text{ cm}^{-2}$ was performed. Seeding recipes were extended to achieve dense diamond seed density on materials other than Si, including different nitride semiconductors such as GaN, AlN and

Al(Ga)N for heterogenous integration of diamond on nitride based devices. The effect of seeding density on the growth of diamond films by hot-filament chemical vapor deposition from sparse to dense range were studied. Using the dense diamond seeding approach, direct integration of diamond on the different nitride semiconductors is studied. The effects of diamond seeding density on growth, morphology, quality and interfacial/material thermal properties were studied using scanning electron microscope (SEM), atomic force microscope (AFM), Raman spectroscopy, x-ray diffraction and steady state thermo-reflectance (SSTR) techniques.

In chapter two, various growth and characterization technique used in this dissertation is discussed in detail. The basics chemical vapor deposition (CVD) and metal organic CVD have been presented along with a brief description of specific tools used for this research. Physical principles of various characterizations technique along with a brief tool specific description have also been presented.

In chapter three, optimization of diamond seed density on various semiconductors using electrostatic seeding approach is discussed. The basic principle for the seeding approach is presented while discussing dip electrostatic seeding. Later, the limitations of dip electrostatic seeding technique were optimized with an innovative seeding approach to obtain diamond seed density ranges from 10^8 cm^{-2} to 10^{12} cm^{-2} . An innovative diamond seeding recipe along with state of characterization technique such as AFM to determine the diamond seed density accurately, is discussed.

In chapter four, the effects of diamond seed density on the growth of diamond film by hot filament chemical vapor deposition from sparse to dense range is presented. A multistep growth was performed to understand the growth kinetics of diamond film

with different seed density. Scanning electron microscopy (SEM) and Raman spectroscopy is used to study the morphology, interface, and quality of diamond film. The effect of diamond seeding density on interfacial and material thermal properties are also discussed.

In chapter five, the effect of seed density with diamond growth on gallium nitride without dielectric adhesion layer is presented. The quality of diamond and gallium nitride material quality before and after the diamond growth is studied in detail and presented.

In chapter six, the effect of diamond seed density on the quality, morphology and interface properties of diamond film grown on aluminum nitride is presented. Structural, morphological and thermal properties of thick diamond film grown with sparse to dense diamond seeding density is discussed on detail.

Finally, chapter seven provides a summary of the dissertation, addresses conclusion of this work and suggested possible future works.

II. CHEMICAL VAPOR DEPOSITION PROCESSES AND CHARACTERIZATION TECHNIQUES

In this chapter, a brief overview of the two main deposition system used for this dissertation; hot filament chemical vapor deposition (HFCVD) and metal-organic chemical vapor deposition (MOCVD) is described. Also, details of the other instruments and characterization tools used for this research is presented. A brief discussion on the general physics and working principle of each of the characterization tools is presented.

Hot Filament Chemical Vapor Deposition

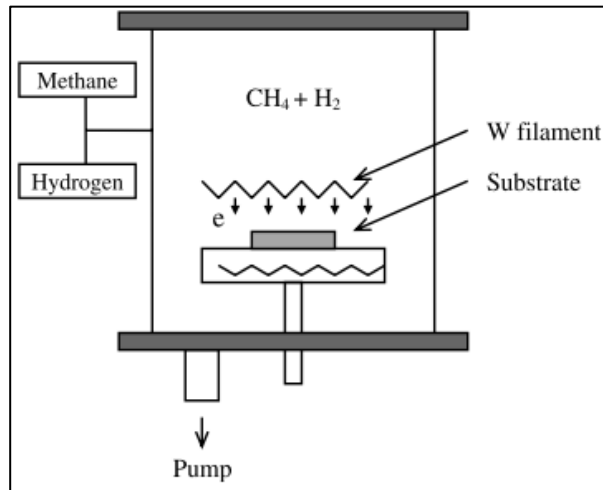


Figure 2.1. Schematic representation of HFCVD process for diamond deposition [20].

Hot filament CVD is the oldest and one of the most widely used techniques for diamond deposition and was first developed by Matsumoto and co-workers at NIRIM, Japan [18,20]. A systematic representation of the HFCVD system is shown in Figure 2.1. In this method, diamond particles or films are deposited on a heated substrate from a mixture of methane and hydrogen dissociated by hot tungsten, or another high-melting-

point metal filament placed close to the substrate. The filament temperature may reach around 2200 °C during this process [18]. The main role of the hot filament is to dissociate molecular hydrogen into atomic hydrogen. At higher pressures (3–4 kPa) the dissociation occurs mainly near the filament (without adsorption and desorption) due to the high gas temperature. At lower pressures the filament surface acts as a catalyst for adsorption of molecular hydrogen and desorption of atomic hydrogen. The dissociation equilibrium is governed by thermodynamics [62].

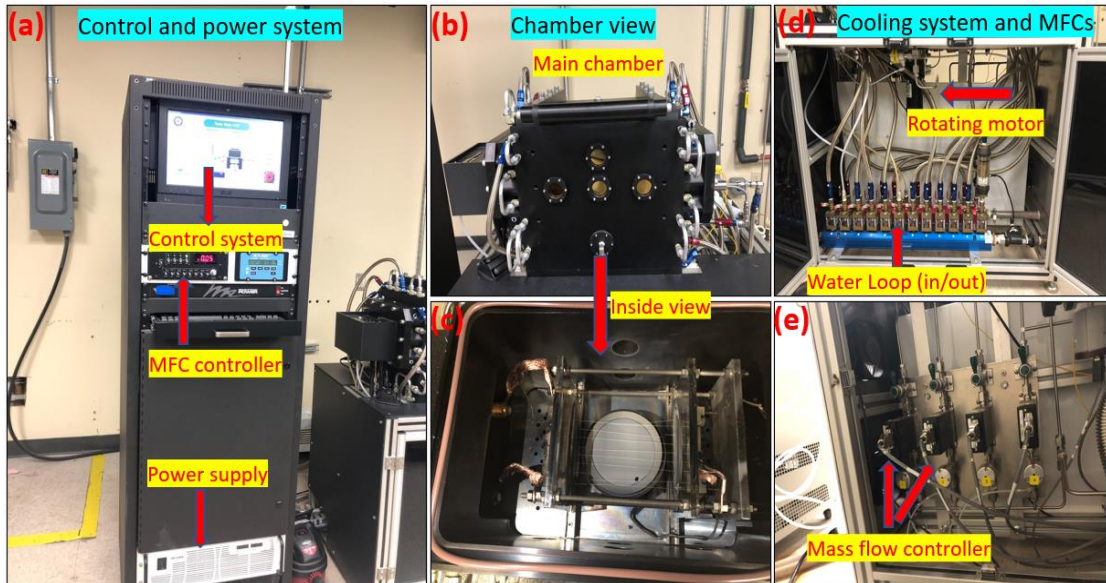


Figure 2.2. Different parts of the Hot Filament CVD reactor at Texas State University (a) Computer control system and power supply, (b)-(c) front side of chamber and inside the chamber, (d)-(e) Chamber cooling water loop and Mass flow controllers.

During diamond deposition, the tungsten filaments react with methane and undergo carburization [21]. This results in the consumption of carbon from the methane, and thus specific incubation is needed for the diamond nucleation. This process may

affect the early stages of diamond growth. In addition, the resistance of the filament should be monitored and adjustments to the supplied voltage and current made in order to keep the temperature of the filament constant [21]. A set of new wires is required for each deposition because metal carbides are extremely brittle and tend to break off from the array during wafer unloading.

For this dissertation research, the Texas State Hot Filament CVD system was used, which was originally manufactured by Crystallume Inc. The various parts of the system are shown in Figure 2.2(a)-(e). The recipe for the growth can be optimized by using custom built Opto 22 software, shown in Figure 2.2(a). A water-cooled substrate holder connected to a rotating motor is used to maintain uniformity during diamond deposition. The whole chamber is connected to the building chilled water loop to maintain the temperature during the growth, shown in Figure 2.2(d). For diamond deposition, we vary the precursor concentration for desired thickness and quality of diamond. In general, we supply (1-3) % of CH₄ with 3 standard cubic centimeter per minute (sccms) of oxygen. The gas inside the chamber is controlled by Mass Flow Controllers (MFCs). The diamond growth process for this dissertation was optimized using nine tungsten wires of diameter 0.25 mm separated by 1 mm. The array is visible over a nano-diamond seeded 100 mm wafer, shown in Figure 2.2(c). The HFCVD reactor is capable of depositing diamond with maximum current of 107 A current and a voltage of 66 V. The pyrometer reads the surface temperature through the quartz window on the back side of the reactor. Increasing pressure increases the growth rate due to increased resident time of the reactants. The main knobs to increase the growth rate and affect film quality are precursor concentrations i.e., methane concentration, deposition pressure and

growth temperature. Substrate to wire distance and wire temperature basically control the surface temperature and thereby growth rate. The HFCVD reactor used for this research was capable of growing diamond with 0.5-4.5% (10-90 sccm) methane in hydrogen (2 SLM). Under these conditions the diamond growth can be varied between 0.2 $\mu\text{m}/\text{hour}$ and 1.5 $\mu\text{m}/\text{hour}$ [22].

Metal-Organic CVD for III-Nitride Deposition

MOCVD is a chemical vapor deposition technique that can be used to make single or polycrystalline thin films. It's a method for creating a complicated multilayer semiconductor structure. It's a non-equilibrium thin film deposition process that utilizes gas phase transport of metal-organic precursors (OMs), hydrides (nitrogen sources like ammonia), and carrier gases onto a heated substrate, where the precursors are pyrolyzed and a film is deposited [61]. This method is preferred for fabricating devices with thermodynamically metastable alloys, and it has become a key step in the production of optoelectronics like UV to visible light-emitting diodes.

The components of a general MOCVD reactor system can be grouped into the several parts. A systematic representation of a MOCVD system is shown in Figure 2.3. The reactor system is categorized into three major sections: (1) the gas delivery system (2) the reactor growth chamber and (3) the exhaust system. The detailed chemical reactions occurring in MOCVD are very complicated; however, the process can be represented by a very simple formula for a reaction of III-V employing metal-organic precursors [63] and hydride precursors [63],



Where M is a Group III metal atom, e.g., Ga, Al or In; R is an organic radical,

typically CH_3 (methyl) or C_2H_5 (ethyl); E is a Group V atom e.g., As, P or N; and H is atomic hydrogen. While this simplified net reaction ignores the intermediate reactions or additional by-product formation that may occur in the gas phase and on the surface, it provides a basic framework that can be used to describe the more complicated cases where more than one metal-organic and/or hydride precursors are involved. In MOCVD of group III-Nitrides, precursors and their transports are completely different than conventional CVD. MOCVD of III-V compound semiconductors generally employs mixtures of Group III metal-organic and Group V hydride precursors in a carrier gas. Typical carrier gases are H_2 , N_2 , or mixture of H_2 and N_2 , and the precursors are transported by one or more carrier gases and injected into an open-tube process chamber.

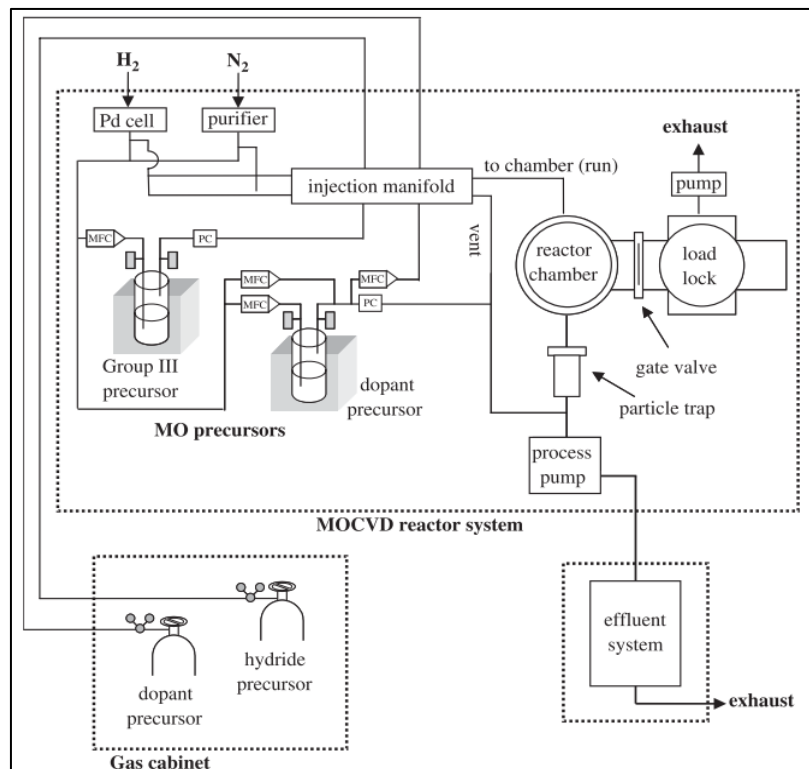


Figure 2.3. Schematic diagram of an MOCVD reactor system [63].

The reactant gases are mixed in the reactor at high temperatures to generate a chemical reaction that results in the deposition of materials on the substrate in the MOCVD process. A reactor chamber is often made of materials that do not react with the chemical in use. The reactor walls, liner, susceptor, gas injector system, and temperature-controlled devices make up the chamber. Cooling water must flow via the channels within the reactor walls to avoid overheating during the growth process. A substrate is placed on a temperature-controlled susceptor. Graphite is commonly used as the susceptor. To prevent ammonia corrosion, a special coating, typically silicon nitride, is applied to the graphite susceptor while growing III-nitrides and similar materials [64]. Alternatively, a solid silicon carbide susceptor may be employed.

Ammonia is a common hydride source for the growth of III-nitrides because it is liquid at room temperature and has a high vapor pressure and can be delivered directly into the reaction chamber. N_2 and H_2 are the carrier gases used. Trimethyl aluminum (liquid at room temperature), trimethyl gallium (liquid at room temperature), and trimethyl indium are the most commonly used organometallic (OM) sources (solid at room temperature). Because the OM precursors are pyrophoric in nature, they are kept in metal-sealed containers known as "Bubblers." Because OM precursors are either liquid or solid at room temperature, they are kept in temperature-controlled baths, and a carrier gas is flowed into the bubblers through a dip tube submerged in the organometallic. After the carrier gas bubbles through the OM liquid precursor, they become saturated with the vapor phase of the OM above the liquid surface. Unless the gas flow rate is too high, the bubbling action sets up an equilibrium between the condensed phase and the vapor phase. The equilibrium vapor pressure, p_{eq} , is normally given by [63],

$$\ln P_{eq,T} = -\frac{A}{T} + B \quad (3)$$

where T is the absolute temperature (K) and A, and B are constants. Equation (3) shows that the equilibrium vapor pressure is strongly dependent on the temperature; therefore, source bubblers should be kept at a precisely controlled constant temperature. The molar flow rate of a metal-organic precursor, $Q_{\text{metal-organic}}$ (mol min^{-1}), is calculated from:

$$Q_{\text{metal-organic}} = \frac{P_{(Eq,T)}}{P - P_{(Eq,T)}} \times \frac{F_{\text{bubbling-gas}}}{C_{STP}} \quad (4)$$

where $F_{\text{bubbling-gas}}$ is the flow rate of the gas flowing through the bubbler (in standard cubic centimeters per min, sccm), P is the bubbler pressure (Torr), $P_{Eq,T}$ is the vapor pressure of metal-organic precursors (Torr) and C_{STP} is a constant for the molar volume of an ideal gas at standard temperature (298.15K) and pressure (760 Torr), i.e., $22\,406 \text{ cc mol}^{-1}$. Precise control of the molar flow rates of Group III precursors is crucial, since in most cases of MOCVD growth the Group III molar flow rates govern the growth rate and composition (solid mole fraction) of the epitaxial layers. Therefore, precise control of the gas flow rate, bubbler total pressure, and temperature of the precursor (and thus the bubbler itself) are important for the controllability and repeatability of the growth; the required precision control is carried out by mass flow controllers, pressure controllers and isothermal baths, respectively [22].

The hydride (Ammonia) can be treated as an ideal gas and the flow rate is calculated using following simple equation:

$$Q_{\text{NH}_3} = \frac{F_{\text{NH}_3}}{C_{STP}} \times \frac{\text{Mixture \%}}{100} \quad (5)$$

The ratio $Q_{\text{NH}_3} / Q_{\text{OM}}$ calculated from equations (4) and (5) is called the well-known ‘V/III ratio’ for MOCVD of any III-V semiconductor. V/III is a universal representation of the molar ratio of OM and hydride which affects the properties of deposited film. However, the V/III value for any specific material is reactor specific and the same value may not always result in similar film properties.

The MOCVD reactor used for this dissertation research was installed at Texas State University in 2014. The common thin films deposited were AlN, GaN and AlGaIn on Si. To achieve high quality III-nitride films, a process has been developed through previous research efforts to deposit on Si. The growth parameters for various III-nitride semiconductor alloys are different in terms of V/III, pressure, and temperature.

Characterization Techniques

Experimental samples for this research were characterized using several morphological and structural characterization tools. A brief discussion on each of the tools are presented in following sections.

Dynamic light scattering. Dynamic light scattering (DLS) is a technique for determine the size distribution profile of small particles or polymer in a suspension [4]. This technique is also known as Photon Correlation Spectroscopy. This is one of the most widely used methods for determining particles size. When a monochromatic beam of light, such as a laser, is shone onto a solution containing spherical particles in Brownian motion, Doppler Shift occurs when the light hits the moving particles, changing the wavelength of the incoming light. This variation is caused by particle size. It is possible to compute the sphere size distribution and give a description of the particle’s motion in the medium, measuring the diffusion coefficient of the particle and using the

autocorrelation function. In DLS, the fluctuation is usually analyzed by means of the intensity of photon auto-correlation function. In the time domain analysis, the autocorrelation function (ACF) usually decays starting from zero delay time, and faster dynamics due to smaller particles lead to faster decorrelation of scattered intensity trace. It has been shown that the intensity ACF is the Fourier transformation of the power spectrum and therefore the DLS measurements can be equally well performed in the spectral domain [65,66]. DLS can also be used to probe the behavior of complex fluids such as concentrated polymer solutions.

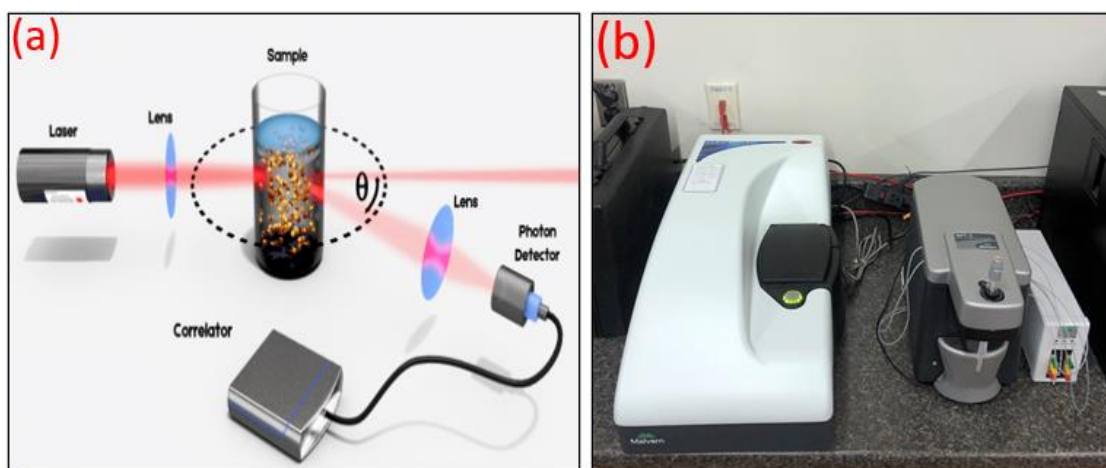


Figure 2.4. (a) Dynamic light scattering technique to measure size and zeta-potential of nanoparticles (b) Malvern Zeta-sizer equipment used for this dissertation.

The basic principle of DLS is straightforward: a laser beam illuminates the sample, and the fluctuations of scattered light are detected by a fast photon detector at a known scattering angle. The basic set up for the dynamic light scattering technique is shown in Figure 2.4(a). Simple DLS instruments that measure at a fixed angle can determine the mean particle size over a narrow size range. More sophisticated multi-

angle instruments can determine the entire particle size distribution. From a microscopic perspective, the particles scatter light, imprinting information about their motion. The fluctuation of the scattered light can thus be used to learn more about the particles. The intensity fluctuations $g_2(t)$ are experimentally characterized, and their analysis yields the particle diffusion coefficient (also known as diffusion constant). The diffusion coefficient D is then related to the radius R of the particles by means of the Stokes-Einstein Equation [67],

$$D = \frac{k_B T}{6\pi\eta R} \quad (6)$$

Where k_B is the Boltzmann-Constant, T the temperature, and η the viscosity.

The correlation of the intensity can be performed by electronic hardware (digital correlator) or software analysis of the photon statistics. Because fluctuation is typically in the range of nanoseconds to milliseconds, electronic hardware is typically faster and more reliable at this job. For this dissertation, a Melvern zeta-sizer equipment was used, shown in Figure 2.4(b), for the measurement of diamond nano-particles size, distribution, and zeta-potential for both polymer and seeds.

Zeta-potential and measurement technique. The charge that arises at the interface between a solid surface and its liquid medium is known as the zeta potential [68]. I.e., the surface charge of nanoparticles in solution, to put it simply. It's a useful technique for determining the status of a nanoparticle's surface and estimating a colloidal dispersion's long-term stability. The unit for Zeta Potential is millivolt (mV).

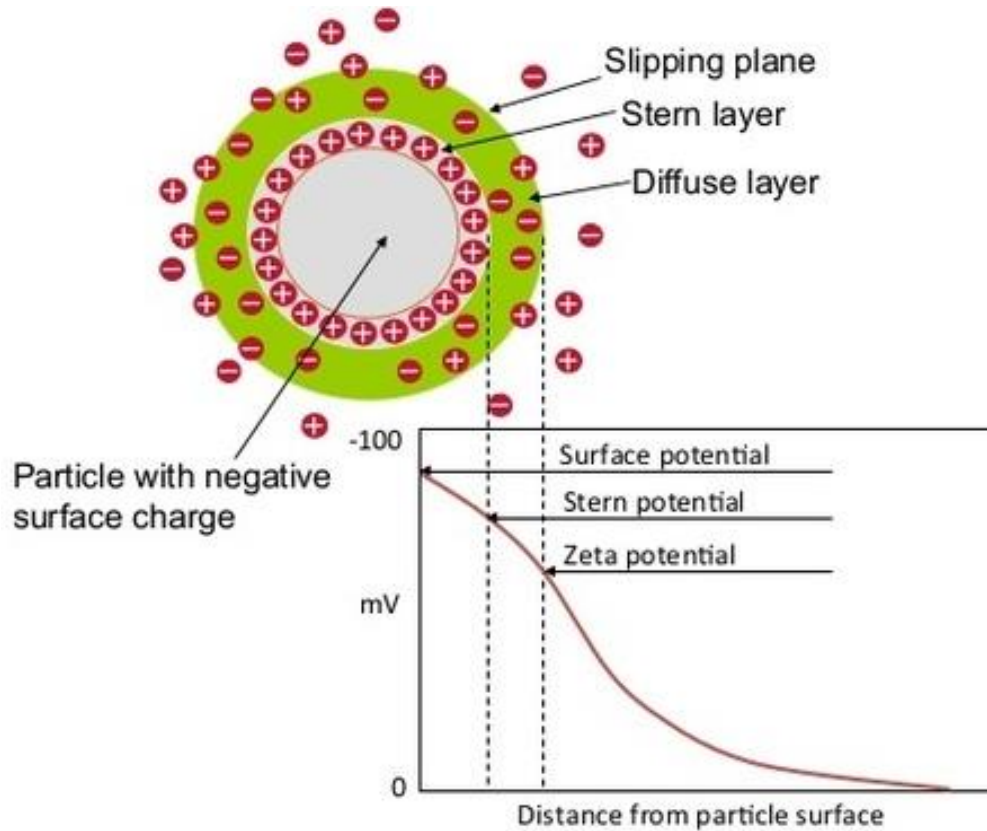


Figure 2.5. Systematic of electric double layer (stern and diffuse) formed on the surface of charged nanoparticle [68].

The functional groups on a particle's surface react with the surrounding medium when it is disseminated in a liquid. A surface charge is created because of this action which draws the aggregation of oppositely charged ions. The stern (ions strongly bonded) and diffuse layers of oppositely charged ions on the surface of scattered particles in a colloidal system (ions loosely bound) [69], are shown in Figure 2.5. The voltage at the diffuse layer's edge where it touches the surrounding liquid is known as the Zeta potential (slipping plane). Due to a lack of repulsive forces, the colloid will start to flocculate, conjugate, and eventually sediment if the charge of nanoparticles falls below a specific

level, creating instability.

Zeta-potential is measured using the electrophoresis principle [69]. Sample particles are suspended in a solvent of known refractive index, viscosity, and dielectric constant. The sample is irradiated with a laser of specific wavelength and an electric field is applied. Due to the electric field the particles are in motion and scatter the laser light. The angle for the scattered light as well as the mobility of the particles are used to calculate the zeta-potential using Smulochowski model [69].

Atomic force microscope. Atomic force microscopy (AFM) belongs to the group of scanning probe microscopy techniques in which the resolution can be down to the atomic scale if careful sample preparation and measurement conditions are fulfilled [70]. The working principle for AFM is based upon the repulsive forces formed between two objects when they are brought closer. An AFM consists of a scanning probe which consists of a cantilever. Figure 2.6(a) show a general block diagram of AFM working principle. A sharp tip, typically made up of different metals, is in continuous or intermittent contact with the sample during the scan depending on the choice of the scanning mode. A laser beam is focused on the back of the cantilever tip and deflected from the cantilever tip toward a four-quadrant optical detector [71]. For optimum detection surface morphology, the laser beam should be aligned appropriately. AFM has three primary modes, force measurement, imaging, and manipulation [71]. The force between the tip and the sample as a function of separation distance is considered for the force measurement mode. The force between tip and sample can be used to control the scan resolution of the sample.

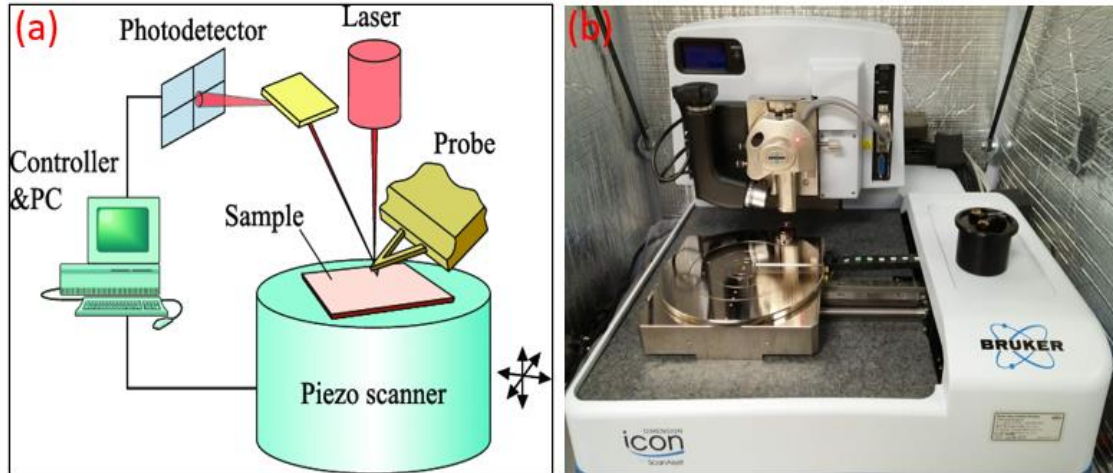


Figure 2.6. (a) Schematic diagram of an AFM system [72] (b) The Bruker dimension ICON AFM at Texas State University.

The AFM used for this dissertation was a Bruker dimension ICON as shown in Figure 2.6(b). Most of the measurements were performed in tapping mode. Various parameters can be controlled before and during AFM measurement. The most important parameters affecting quality of AFM imaging are the feedback parameters: amplitude set point, and proportional/integral gains. The gain parameters determine the sensitivity of control over the surface features. For example, high gain parameters result in high noise. These parameters were varied in order to maximize the agreement between the trace and retrace lines. The lines must directly overlap as much as possible, and all the parameters are considered only when the lines are overlapped. Cantilever tuning is another important factor that affects the measurement accuracy. However, the scan assist mode of the ICON AFM was very robust in terms of optimization. In this mode, no parameter except the spring constant and peak force are required to change. These parameters too are automatically optimized resulting in faster imaging. The most important parameter

obtained from an AFM image for the present studies is the root mean square roughness given by [73],

$$R_q = \sqrt{\frac{1}{L} \int_0^L |Z^2(x)| dx} \quad (7)$$

where, $Z(x)$ is the function that describe the surface profile analyzed in terms of height (Z) and position (x) over the evaluation length L . In addition to RMS roughness, AFM was used for determining seeding density, determining defect in nitride semiconductor, measuring small step height on sample surface etc.

Scanning electron microscope. Scanning Electron Microscopy (SEM) is an essential tool for the study of the surface and the near surface regions of thin films. The electron gun emits a beam of electrons which are accelerated by the presence of an anode. The electron beam is focused by a set of electromagnetic lenses which are controlled by a magnetic coil. The electron beam accelerating voltage is typically in the range of 1- 30 keV and, among other things, determine the beam size and resolution of the microscope. The scan coils divert the beams to form a scanning pattern on the surface. The electrons impact the surface and the near surface region of the sample and react with the atoms within the sample under study. A variety of interactions can be used as a signature providing information about the sample. The interactions of the electron beam with the sample's atoms produce many secondary electrons such as auger electrons, cathodoluminescence, secondary electrons, backscattering electrons, and x-rays [74,75]. The schematic view of an SEM chamber is shown in Figure 2.7(a).

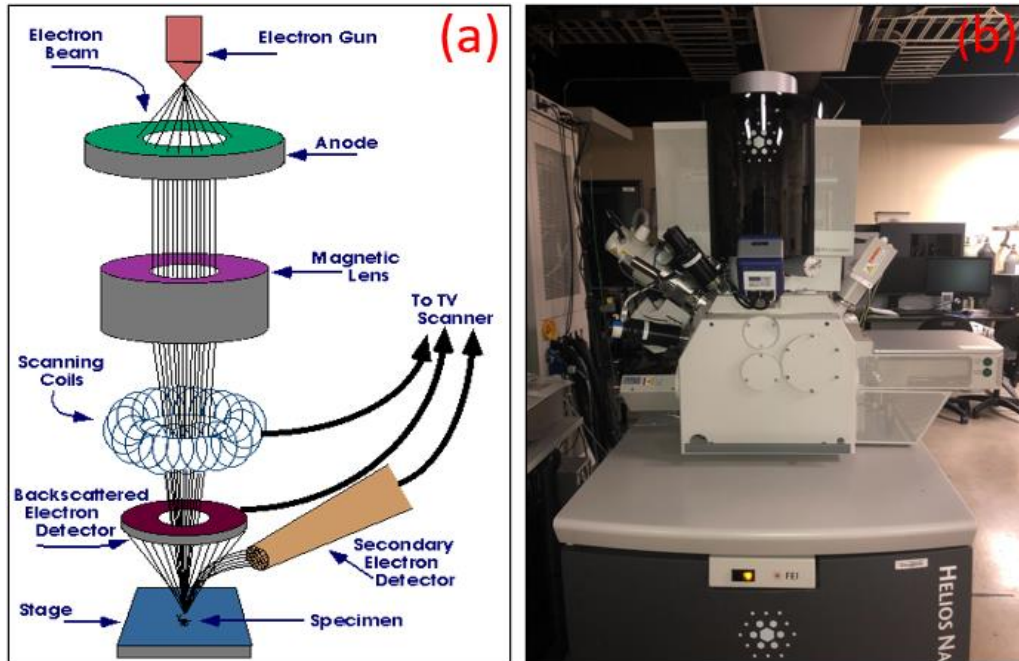


Figure 2.7. (a) Schematic view of an SEM chamber [76] and (b) FEI HELIOS Nano Lab SEM at Texas State University.

SEM can also be used for chemical analysis of the sample. There are two types of instruments being used for the chemical analysis using X-rays: Energy Dispersive Spectroscopy (EDS) and Wavelength Dispersive Spectroscopy (WDS). Both EDS and WDS measure the x-rays emitted from the sample. EDS uses an energy height detector that can determine the number of photons per second in a certain energy range. WDS uses a diffraction device to separate out photons with different wavelength. The resolution of WDS is significantly better than that of EDS. EDS can measure all arriving energy x-rays from the sample at the same time, but the WDS can measure the counts for the arriving x-rays for specific wavelengths. The depth of focus of the scanning electron microscope is far better than another optical microscope [75]. For high laterals

and spatial resolution images, scanning electron microscope with minimum electron wavelength is used.

Figure 2.7(b) shows the FEI HELIOS Nano Lab SEM at Texas State University. Two dedicated detectors namely Everhart-Thornley detector (ETD) and through the lens (TLD) are mainly used for topographical imaging and they can detect both secondary electrons (SEs) and backscattered electrons (BSEs). Usually, for lower resolution imaging in field free mode, the ETD is employed. For high resolution imaging TLD is always used in immersion mode of the SEM [77]. The images produced by detecting SEs provide valuable information about the topography of the sample whereas the image produced by detecting BSEs give much more information about the composition of the sample. Each of the detectors has its own application in specific samples. Some advanced detecting option such as solid-state detector (vCD), down hole visibility is also available in SEM to image at low accelerating voltage. With the SEM shown in Figure 2.7(b), with electron beam energy as low as 1.5kV is capable of yielding operation resolution down to 1 nm given that any insulating sample is properly grounded. In addition to general imaging, this SEM is equipped with Energy dispersive X-ray (EDX) capability. Electron beam deposition, Electron beam lithography, focus ion beam (FIB) are some other capabilities. This SEM was the primary tool for the characterization of deposited diamond and III-nitride films. In addition, FIB cross section of the deposited films was also performed using this tool.

Raman spectroscopy. Raman spectroscopy is a spectroscopic technique typically used to determine the vibrational modes of molecules, although rotational and other low frequency may also be observed. Raman spectroscopy relies on inelastic scattering of photons that involves absorption of incident high intensity laser light by a polarizable sample and causes a transition from the ground electronic state to an excited or virtual state. The energetic system then goes through a radiative relaxation via a transition from the virtual state to a lower energy electronic state by spontaneous emission of a photon and either creating (Stokes's process) or absorbing (anti-Stokes's process) a vibrational quantum of energy (a phonon in crystals) [78]. The emitted photon has a shifted energy from the incident excitation photon energy ($\hbar\omega_L$) by the phonon energy. In conventional Raman spectroscopy, only Stokes processes are studied because of their higher intensities. The Raman spectra of intensity versus emission photon energy exhibits peaks at energy $E_s = \hbar\omega_s$ which corresponds to the vibrational energies involved in the process [79]. Note that in Raman spectroscopy, change in vibration energy is written as inverse of wavelength as $1/\lambda \text{ (cm}^{-1}\text{)} = \Delta E / hc$ where $\Delta E = \hbar\omega_L - \hbar\omega_s$. Not all the vibrations give Raman peaks. This is dictated by Raman selection rule. The Raman selection rule can be derived from the kinematics of inelastic scattering of light in term of conservation of energy and momentum as [79,80];

$$\hbar\omega_s = \hbar\omega_L - \hbar\omega_p \quad (8)$$

$$\hbar\mathbf{k}_s = \hbar\mathbf{k}_L + \hbar\mathbf{k}_p \pm \hbar\mathbf{K} \quad (9)$$

Where, \hbar is Planck's constant and $\hbar\omega$ is the energy of the laser (L) excitation photon, scattered (S) photon, or phonon(P) either created (-, Stokes) or annihilated (+, anti-stokes) in the Raman process. The $\hbar\mathbf{k}$ momentum term in equation (9) are

analogously labelled with the last term accounting for a reciprocal lattice vector (K). The nearly vertical dispersion of light, relative to the size of first Brillion zone, result in the important $K_p=0$ selection rule for the first order Raman scattering in the crystals. The other selection rule is derived from the polarization of the incident and scattered light, $e_{L(S)}$, and the propagation and polarization properties of phonon in particular crystal symmetry according to [80],

$$I_A, I_{AS} \} I_0 V \omega_L \omega_s^3 \sum |e_L \cdot R_j \cdot e_s|^2 \begin{cases} n_B(\omega_p, T) + 1, & \text{Stokes} \\ n_B(\omega_p, T), & \text{anti-Stokes} \end{cases} \quad (10)$$

Where, I_0 is the intensity of incident laser, V is the scattering volume, and R_j is the Raman Tensor for the phonon of the crystal structure being measured with j displacement direction. I_s is the Stokes (S), and I_{AS} is the anti-Stokes (AS) scattering intensity. The quantity $n_B(\omega, T)$ is Bose function at energy $\hbar\omega$ and absolute temperature T .

The Raman spectrum of single-crystal diamond is dominated by the first-order Raman line at 1332 cm^{-1} , which corresponds to the vibrations of the two-interpenetrating cubic sublattices. For an infinite lattice only the zone-center phonon modes are observed in the first-order spectrum, a requirement which is relaxed when the crystallite size is reduced. The first-order Raman modes are triply degenerate TO(X) phonons of F2g symmetry [81]. In an isotropic diamond crystal, they consist of one longitudinal mode (singlet) relative to the direction of propagation and two degenerate transverse (doublet) modes.

Raman spectroscopy is a powerful technique often used to study CVD diamond films [18,21]. Excitation using laser wavelengths in the UV and visible regions are most used, and for diamond films these typically produce spectra with a limited number of

characteristic peaks, including the diamond peak ($\sim 1332 \text{ cm}^{-1}$), the D and G bands from graphitic impurities, and sometimes the 1150 and 1450 cm^{-1} bands from sp^2 carbon impurities at the grain boundaries of nanophase diamond [82]. This technique can be used to assess several properties such as stress, crystallite perfection, phase purity, crystallite size and thermal conductivity of diamond films. The sharp Raman lines can be used to recognize cubic diamond against a background of graphitic carbon and also to characterize the graphitic carbon. Trends in the diamond volume fraction were obtained by calculating the ratio of integrated intensities (area under the curve after background correction) of diamond peak, I_D , to the total intensity from diamond plus that from the non-diamond carbon, I_{NDC} . This is expressed as $I_D / (I_D + I_{NDC})$. The phase purity (sp^3/sp^2 ratio) of the diamond layer can be calculated using equation [83]:

$$PP = (75 \times A_d) / (75 \times A_d + \sum A_{ndc}) \times 100\% \quad (11)$$

where, PP is the phase purity, A_d is the diamond peak area, which was fitted with a Lorentz profile, $\sum A_{ndc}$ is the sum of all non-diamond peaks area including D- and G-peaks, which were fitted with a Gaussian profile. The small shift in the diamond peak wave number have been related to the stress state of deposited films [81]. Several researchers have reported various equation for the stress measurements [22,82]. It is important to note that the biaxial stress depends on the orientation of the polycrystalline diamond. According to Praver et al. [81] the biaxial stress can be given by,

$$\sigma_{xx}(\text{GPa}) = k \Delta\omega \quad (12)$$

where, $\Delta\omega$ represents the diamond peak shift from single crystalline diamond peak ω and k is the Raman stress factor.

Ultraviolet micro-Raman spectroscopy. The systematic representation of the UV Raman system at the optical characterization lab at Texas State University is shown in Figure 2.8. A laser beam is used on this system to scan the samples instead of a point. The laser excitation for the micro-Raman system used for characterizing the present samples was 363.8 nm excitation from an argon-ion laser focused on the sample through a Powell lens. The Powell lens can be visualized as a prism with a small radius at one edge, which operates as a cylinder lens with radius of curvature decreasing from center to edge. Due to such a geometry, a monotonic decrease in divergence takes place from center to edge of the lens resulting in a uniform intensity along its length. The non-uniformity in beam intensity along the line can be less than 10%. Powell lens converts the point beam into a laser line and Raman measurements were carried out using a 10× objective for a nominal line size of ~192 μm. This laser line corresponds to 400 pixels in the charged coupled device (CCD) detector and each pixel corresponds to one Raman spectra.

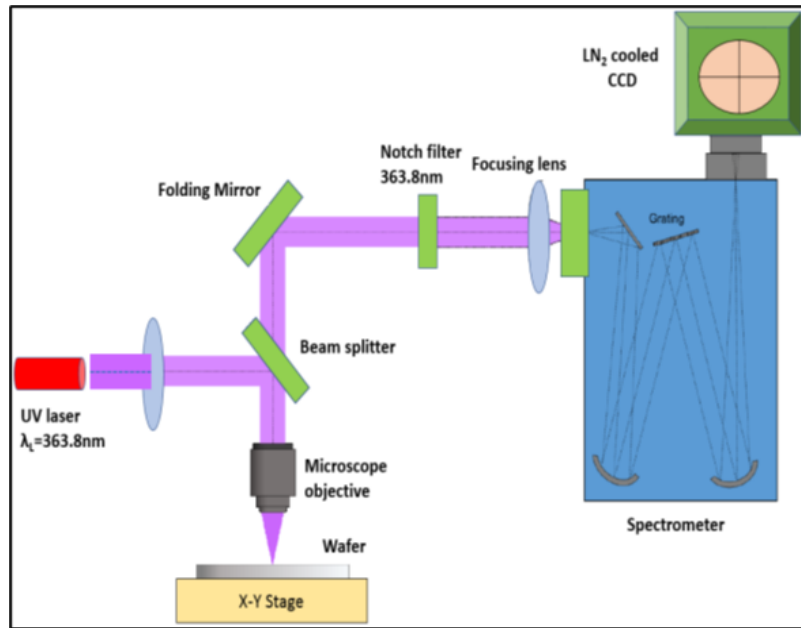


Figure 2.8. Schematic diagram of the UV Raman set-up at the optical characterization laboratory, Texas State University [22].

For this project, the Raman system was calibrated at the beginning of the measurement with both Neon and Argon lamps. The wave number calibration was made using a diamond anvil cell prior to measurement with the Raman shift of 1330.9 cm^{-1} . The laser power for the UV excitation was $\sim 50 \mu\text{W}$, acquisition time for Raman spectra collection was 60 sec. Lorentzian peak fitting was performed for all spectra collected across diamond samples and peak position, width, diamond/non-diamond phase volume fraction and intensity were recorded for them.

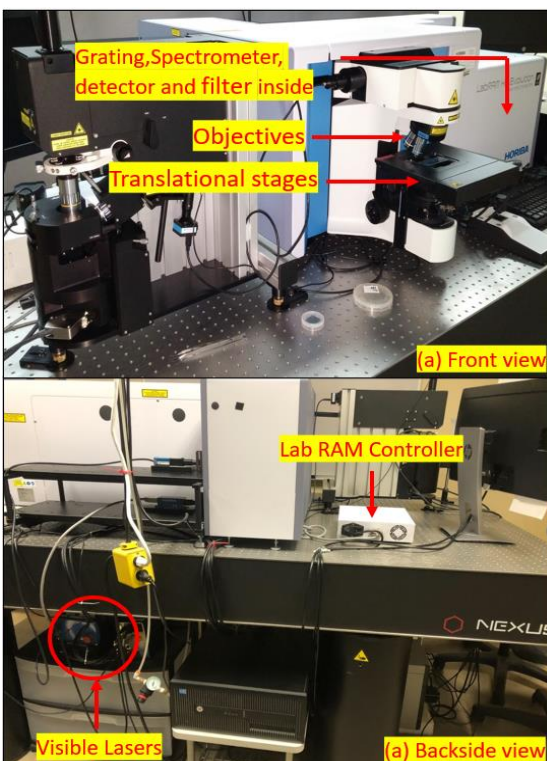


Figure 2.9. The Lab RAM HR evolution visible Raman system (HORIBA scientific) of ARSC at Texas State University (a) Front view and (b) Backside view.

Visible micro-Raman spectroscopy. In addition to UV-micro-Raman spectroscopy, the diamond samples were also scanned from the visible Raman spectroscopy using HORIBA scientific (Lab RAM HR Evolution) at Texas State University. Figure 2.9 shows the image of the visible Raman system at Texas State University. The visible system works within the same principles as UV with only a difference in laser wavelength. Three excitation lasers 532 nm, 633 nm and 785 nm are available on this system. For visible Raman measurements on the present samples, 532 nm laser excitation was used. This system has the capability to measure spectra with high resolution $< 0.5 \text{ cm}^{-1}$. The system is equipped with motorized XYZ stage for optical

mapping. Figure 2.9(a) represent the front view of the system showing objective, translational stage and a set up box containing the spectrometer, grating, detector and filter. The visible lasers and Lab Ram controller is shown in the backside view of the system in Figure 2.9(b).

X-ray photoelectron spectroscopy. X-ray photoelectron spectroscopy (XPS) is a surface-sensitive quantitative spectroscopic technique based on the photoelectric effect that can identify the elements present in a material (elemental composition) or on its surface, as well as their chemical states, and the overall electronic structure and density of the electronic states in the material. XPS is a useful measurement method since it displays not only what components are there, but also what other elements they are bound to. When combined with ion-beam etching, the process can be utilized for line profiling of the elemental composition over the surface or in-depth profiling. It's frequently used to investigate chemical reactions in materials in their natural condition or after cleavage, scraping, heat exposure, reactive gasses, or solutions[81].

XPS is a type of photoemission spectroscopy in which electron population spectra are obtained by irradiating a material with an x-ray beam. Chemical states are deduced from measurements of kinetic energy and the number of electrons ejected. XPS requires high vacuum (residual gas pressure $p \sim 10^6$ Pa) or ultra-high vacuum ($p < 10^7$ Pa) conditions, though ambient-pressure XPS, in which samples are analyzed at pressures of a few tens of millibars, is a current area of development.

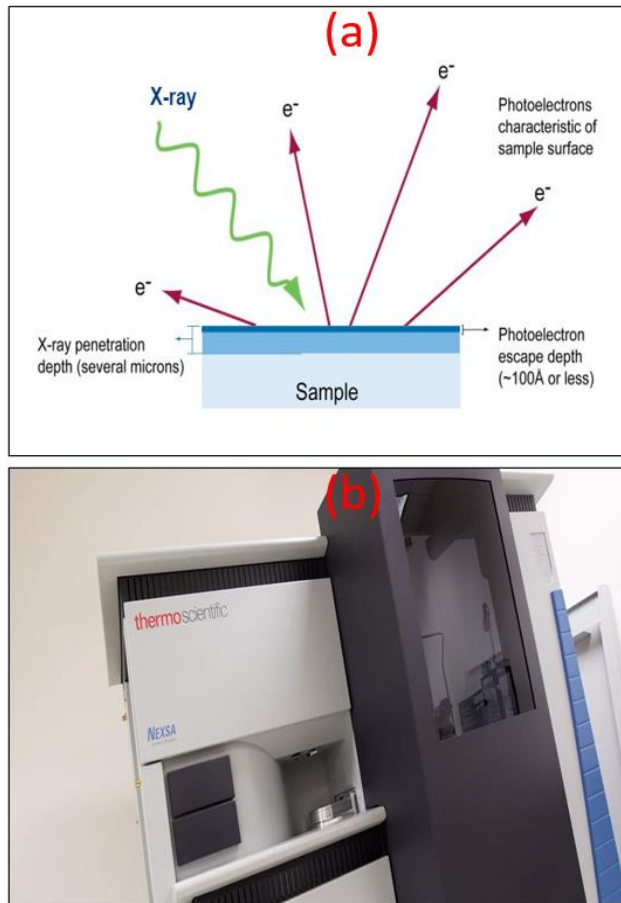


Figure 2.10. (a) Basic principle for XPS [85] (b) Nexsa photoelectron spectroscopy at Texas State University.

XPS works based on photo-electric effect principle, shown in Figure 2.10(a). Because the energy of an x-ray with particular wavelength is known (for Al K α x-rays, $E_{\text{photon}} = 1486.7 \text{ eV}$), and because the emitted electrons' kinetic energies are measured, the electron binding energy of each of the emitted electrons can be determined by using the photoelectric effect equation [84,86];

$$E_{\text{binding}} = E_{\text{photon}} - (E_{\text{kinetic}} + \phi) \quad (13)$$

where E_{binding} is the binding energy (BE) of the electron measured relative to the chemical potential, E_{photon} is the energy of the x-ray photons being used, E_{kinetic} is the kinetic energy of the electron as measured by the instrument and ϕ is a work function-like term for the specific surface of the material, which in real measurements includes a small correction by the instrument's work function because of the contact potential. This equation is essentially a conservation of energy equation. The work function-like term ϕ can be thought of as an adjustable instrumental correction factor that accounts for the few eV of kinetic energy given up by the photoelectron as it gets emitted from the bulk and absorbed by the detector. For this dissertation, we used Thermo Fisher Scientific Nexsa x-ray photoelectron spectrometer (XPS) shown in Figure 2.10(b) to characterize diamond phase.

Surface profilometer. A profilometer is a highly specific metrological measurement device that is used for the determination of the thickness and roughness of a thin film. It is a very precise instrument as it is expected to have the ability to find or quantify small-scale surface features. The primary uses of the surface profilometer are focused on characterizing a surface's profile to quantify its roughness. Critical dimensions such as step size, curvature, and flatness are computed from the measured surface profile [87]. A typical profilometer requires the probe tip to be in direct contact with the sample surface, thus making it potentially a destructive measurement technique [87]. A systematic diagram of a simple stylus profilometer measurement set up is shown in Figure 2.11(a). For this dissertation, the profilometer used was a Dektak XT surface profile meter, shown in Figure 2.11(b). The instrument was used to determine the surface roughness and the thickness of the diamond films at a different position on the samples. The Dektak XT

profilometer is an advanced thin and thick film step height measurement tool which can measure the roughness on the nanometer scale. It can provide the step-height with repeatability of 5 Å. It is equipped with an automatic X-Y plus theta stage which allows 2D as well as 3D scans. The principle of the profilometer is based upon the surface contact measurement technique where a deficient force (1-15 mg) stylus is dragged across the sample surface.

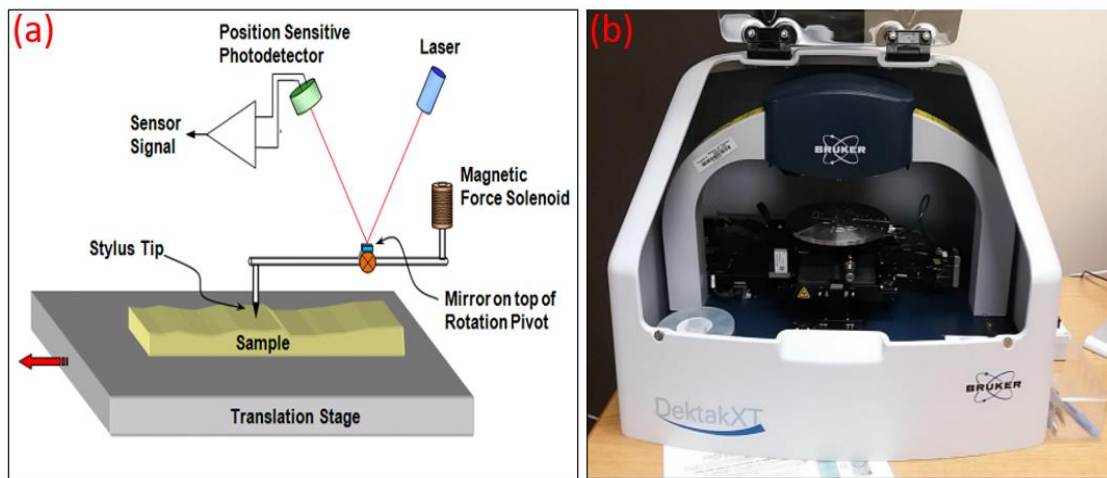


Figure 2.11. (a) A schematic diagram of the stylus profilometer measurement set up [87] (b) The Dektak XT stylus profilometer of ARSC at Texas State University.

X-ray diffraction. All materials have unique properties such as structural, physical, mechanical, thermal, and electrical properties. These properties must be investigated in order to gain a better understanding of how different materials can be meaningfully applied in semiconductor devices. Analytical tools for studying structural, physical, morphological, optical, and electrical properties, among other things, have been developed. The study of structural properties is important because it determines the

remaining properties of the materials. X-ray diffraction is a technique used to study the order of atoms in materials and to determine the crystal structure and quality of the material.

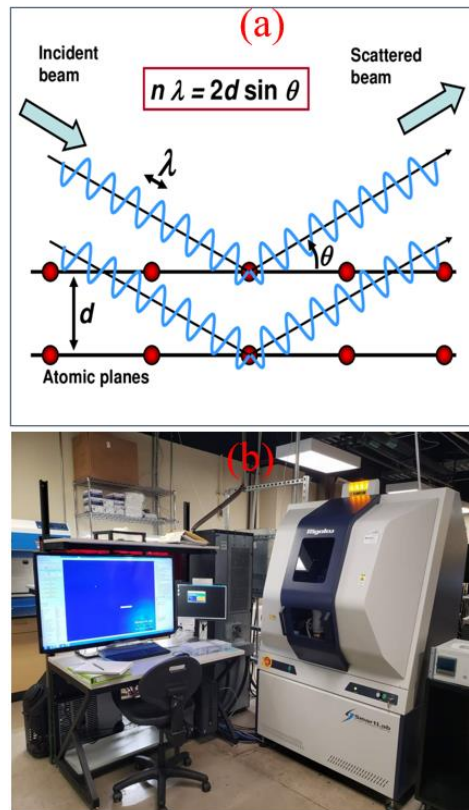


Figure 2.12. (a) Schematic representation of Bragg's law where λ is x-ray wavelength, n is an integer, θ is the incident angle and d_{hkl} is the lattice spacing of the (hkl) crystal plane and (b) Rigaku Smart Lab XRD system at Texas State University.

The method employs a monochromatic x-ray beam that is directed at a precise angle onto the sample surface. The x-ray interacts with the sample in the same way that a light beam interacts with a grating, and the diffraction effect discloses the crystal structure of the materials under investigation. The x-rays are constructively reflected and detected by the XRD apparatus in the case of a suitable orientation of crystallographic

planes within the sample. The intensity of an x-ray beam diminishes as it travels through a substance, and this decline is proportional to the distance traveled through the substance. Only a small number of distinct x-rays are commonly employed for diffraction. X-rays are created with an x-ray tube, in which an electron beam is accelerated towards a target by a high electric potential. Upon impact, the electrons will excite and ionize the target atoms creating element-specific x-rays of specific wavelengths. When the voltage on an x-ray tube is increased above a specific value, then the wavelengths of characteristic lines of target metal are obtained. These characteristic lines are denoted by K_{α} , K_{β} , and K_{γ} . These characteristic lines were discovered by W.H. Bragg. He and his son W.L. Bragg pioneered determining the crystal structures of NaCl, KCl and KBr, etc. [88]. The famous Bragg's law was formulated based on the conditions of constructively diffracting x-rays [88,89];

$$2d_{hkl}\sin\theta=n\lambda \quad (14)$$

Where, ' λ ' is the wavelength of incident radiation, ' Θ ' is the angle of incidence, ' d_{hkl} ' is interplanar spacing between two adjacent crystallographic planes and ' n ' is an integer. The integers should be whole numbers in order for x-rays to be diffracted constructively. The schematic representation of Bragg's law is shown in Figure 2.12(a). Bragg's law suggests that diffraction is only possible when $\lambda \leq 2d$. The X-ray spectrum for any material is plotted as x-ray intensity versus 2θ graph. The obtained spectrum is analyzed by comparing with the x-ray crystallographic library or database to obtain the orientation and composition of the layers in the grown structure. The lattice constants and many other structural properties such as crystal quality, strain, defect etc. can be accurately evaluated using XRD.

To study the structural properties of the films deposited during this dissertation research a Rigaku Smart Lab XRD system was employed as shown in Figure 2.12(b). The wavelength used for the measurements was Cu K α , $\lambda = 1.5418 \text{ \AA}$ and the x-ray tube operated at 40 kV and 44 mA. In addition to standard $\theta/2\theta$ scan, other types of scans were employed to study the diamond and III-nitride semiconductors. To study the quality of crystal and defect in crystal, a rocking curve (ω scan of a specific plane), reciprocal space mapping (RSM) was performed. An extended rocking curve between $2\theta = 33.5^\circ$ and 37° of AlGaIn/GaN revealed the (0002) planes of these materials which was often used as a quick determination of crystal quality.

Steady state thermo-reflectance. With steady state thermo reflectance (SSTR), one can measure the thermal conductivity of a variety of materials over a wide range. It is a radial heat flow technique based on a continuous wave pump and probe laser [90]. The SSTR is robust and is capable of measuring materials whose thermal conductivities range from 1 to $>2000 \text{ W m}^{-1} \text{ K}^{-1}$, showing excellent agreement with literature values. The SSTR technique has key advantages compared to conventional steady-state techniques like time and frequency domain thermo-reflection. First, it can measure high throughput, usually within 10 minutes depending on resolution requirements. Second, SSTR is non-contact, requiring no attached thermocouple. Compared to TDTR and FDTR, SSTR is facilitated with the deposition of thin metal film transducers. Due to the time scales associated with SSTR measurements (i.e., $>$ tens of microseconds) being much longer than the lifetimes of photoexcited carriers, an additional transducer may not be required. In addition, steady-state techniques require large thermal resistances for accurate measurements so that the minimum sample volume required scales with the

sample's thermal conductivity. Unlike SSTR, thermal penetration depth in SteadyState laser heating is solely governed by the pump radius. In this sense, the measurement volume of SSTR is independent of the material's thermal properties.

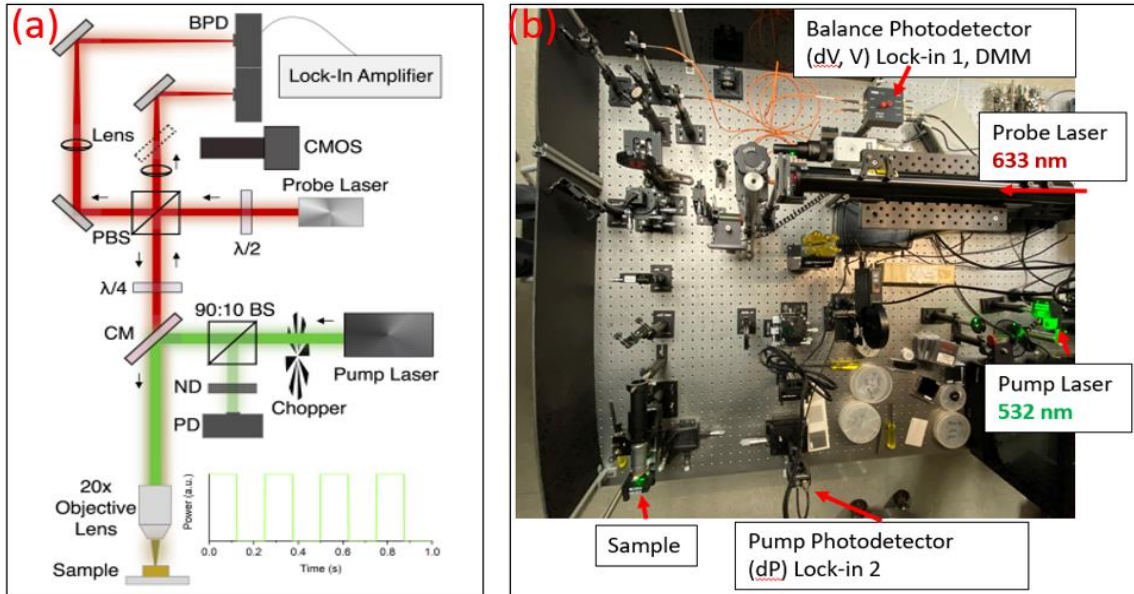


Figure 2.13. (a) Schematic of the Steady-State Thermo Reflectance (SSTR) experiment [84] (b) Texas State SSTR set up.

A schematic diagram of steady state thermo reflectance (SSTR) experiment is shown in Figure 2.13(a). The principle of SSTR is based on detection of reflectivity (R) due to an induced temperature(T) rise in the materials. In some cases, the reflectivity changes due to induced temperature is very small and in the order of 10^{-5} to 10^{-4} K^{-1} [90]. This issue can be overcome by using a periodic heat source with lock-in amplification (LIA) techniques by amplification and electronic filtering. In addition, a periodic waveform analyzer (PWA) with a boxcar average can be used with large enough sampling time to extract a periodic signal. A constant heat flux is typically used in

steady-state techniques to induce a transient temperature rise followed by a steady-state temperature rise. The transient portion of the temperature rise, which can last for hours in bulk techniques, is ignored, and only measurements in the steady-state regime are taken. Thus, the idea behind SSTR is to modulate the pump beam with a square wave at a low enough frequency to allow for an "on" and a "off" state to achieve the steady-state temperature rise. We can control the temperature rise of the "on" state by varying the power (heat flux) of the pump beam. We can use Fourier's law to determine thermal conductivity based on the linear relationship between heat flux and temperature by measuring the corresponding change in reflectivity (temperature) [90].

Figure 2.13(b) depicts a general experimental setup for SSTR at Texas State University's optical characterization lab. It is made up of a probe laser with a wavelength of 633 nm and an output power of up to 21 mW and a pump laser with a wavelength of 532 nm and an output power of up to 4W. To modulate the pump, a mechanical chopper is used. A balance photodetector with a beam splitter is used to monitor the pump waveform and power. To avoid detector saturation, a neutral density filter is placed in front of the pump photodetector. The transmitted power is then reflected by a cold mirror and focused on the sample by an objective lens. The probe travels through the cold mirror and is detected. For this research, a pump laser of power 600 mW and probe laser with 21 mW was used. A transducer layer comprised of aluminum is deposited on top of diamond film via e-beam deposition for the measurements. The beam was focused using 10X objective with approximate beam size of $\sim 40 \mu\text{m}$. The data were analyzed by a python-based program built by the optical characterization lab at Texas State University.

III. STUDY OF AND OPTIMIZED NANO-DIAMOND SEEDING ON SEMICONDUCTORS

Nano-diamond seeding is a well-established route toward the CVD (chemical vapor deposition) synthesis of diamond thin films. The method is based on the deposition onto the substrate of nano-diamond particles which act as a pre-existing sp^3 seed. In this chapter, an innovative approach is presented to disperse nano-diamond seeds on substrate surface coated with a cationic polymer. A dense nano-diamond seed density is obtained on different semiconductors such as Si, AlN and GaN by taking advantage of electrostatic van der Waal force developed between the diamond nanoparticles with the polymer coated substrate. Also, optimized seeding process is presented with thin polymer layer on semiconductor surface with a sonication process to obtain dense diamond seed density over 10^{12} cm^{-2} .

Introduction

On most non-diamond semiconductor substrates, a seeding step is generally needed to grow diamond film prior to diamond deposition. This is because diamonds have a very different surface energy from the substrate. For example, A diamond's surface energy is 9.4 J/m^2 along (100) whereas Si has a surface energy of 2.12 J/m^2 , making it hard to nucleate diamond directly on Si without providing nucleation sites [91] through, for example, diamond seeding. So, an enhanced seeding density step is required for the growth of a thick diamond film on a non-diamond substrate.

Various attempts have made to enhance diamond seeding density on non-diamond substrates [28,83,92–97]. Some common diamond seeding techniques are chemical nucleation [98], nucleation through surface damage [99], bias enhanced nucleation [100],

nucleation through photoresist [27], electrostatic seeding [28] and mixed diamond seeding [101]. The seeding density by this technique can be obtained in the range of 10^4 to 10^{11} cm^{-2} . Some attempts have been made to get the nucleation density $\sim 10^{12}$ cm^{-2} [57].

The enhancement of diamond seeding density on semiconductor surfaces has been reported by various groups. Williams et al. [24] used a solution of monodispersed nano-diamond seeds prepared by the milling technique to enhance diamond seeding density on Si to $\sim 10^{11}$ cm^{-2} . Mandal et al. [102] showed that the use of hydrogenated seeds on GaN leads to high seeds density $\sim 10^{11}$ cm^{-2} using hydrogenated seeds and low seed density $< 10^{11}$ cm^{-2} using oxygenated diamond seeds. They found that the diamond van der Waal bonding depends on the zeta-potential on the substrate and the diamond seeds. Tiwari et al.[83] used a platinum surface coated with adamantane and found the seeding density $\sim 10^7$ to 10^8 cm^{-2} . The bias enhanced nucleation method described by Arnault et al. [100] showed the maximum seed density of 10^{10} cm^{-2} . Seeding density of $\sim 3 \times 10^{10}$ cm^{-2} has been reported by Barnes et al.[84] by a mixed technique by the use of scratching in combination with carbon deposition or other metal deposition. Sood et al.[81] reported a diamond seed density greater than 10^{12} cm^{-2} by ultra-sonification on ethanol-based nano-diamond slurries. Later, the same seeding technique implemented by Bai et al.[85] found the seeding density of 3×10^{11} cm^{-2} .

There are few reports of achieving seed densities in excess of 10^{12} cm^{-2} with +5 nm ND seeds [81]. Such high-density numbers, in some cases, inferred from diamond grain density after a certain amount of growth. So, it should be taken caution to determine seeding density on such cases since secondary nucleation may also occur during that condition and seems to have enhanced seeding density.

In this chapter, an innovative approach to obtain dense nano-diamond seeding density on semiconductors is discussed in detail. A straightforward approach is presented to disperse nano-diamond on a substrate by taking advantage of electrostatic van der Waals bonding between the oxygen terminated carboxylate diamond nanoparticles and a cationic polymer. By simple dipping of the polymer coated substrate into the nano-diamond solution, electrostatic interactions ensure a spontaneous grafting of the particles onto the substrate surface. An approach to achieve the dense diamond seed density and following optimization and development of seeding recipe is presented. Later, the technique is used on different semiconductors such as Si, AlN and GaN to obtain maximum diamond seeding density.

Experiment and Results

Size and zeta-potential measurements. For diamond seeding, there were different alternatives for cationic polymers such as poly (ethylenimine), poly (diallyl dimethyl) ammonium chloride, poly (2-dimethyl(aminoethyl)methacrylate, poly (L-lysine), and chitosan. Among these, a cationic poly (diallyl dimethylammonium chloride) or PDDAC polymer with positive zeta-potential was used due to its feasibility as well as substantial cost effectiveness. The PDDAC polymer had a molecular weight of 100,000–200,000 g/mol, 20 wt. % water, pH ~ 7 (Sigma Aldrich, St. Louis, MO, USA). The diamond nanoparticles were commercially available carboxylate nano-diamond (Adamas Nano, Raleigh, NC, USA) and were specified as monodispersed diamond nanoparticles at 1 wt. % in de-ionized (DI) water, with solution pH ~7. Prior to seeding, we measured the size of diamond nanoparticles and zeta-potential for both diamond seeds and PDDAC polymer with a dynamic light scattering (DLS) technique using a Malvern Zetasizer Nano

ZS equipped with a 633 nm laser. The diamond seed size and potential between the seed and polymer plays an important role for the uniformity and distribution of diamond nano seeds during diamond seeding [28]. Backscattering configuration was used to determine the average particle size based on 100×30 s scans and the zeta potential of 300 scans. For polymer zeta-potential measurements, the PDDAC polymers were further diluted with 1 mM aqueous KCl prior to zeta-potential measurement. The small amount of KCl acts as a background electrolyte to ensure that low impurity concentrations do not adversely affect the DLS measurement [105].

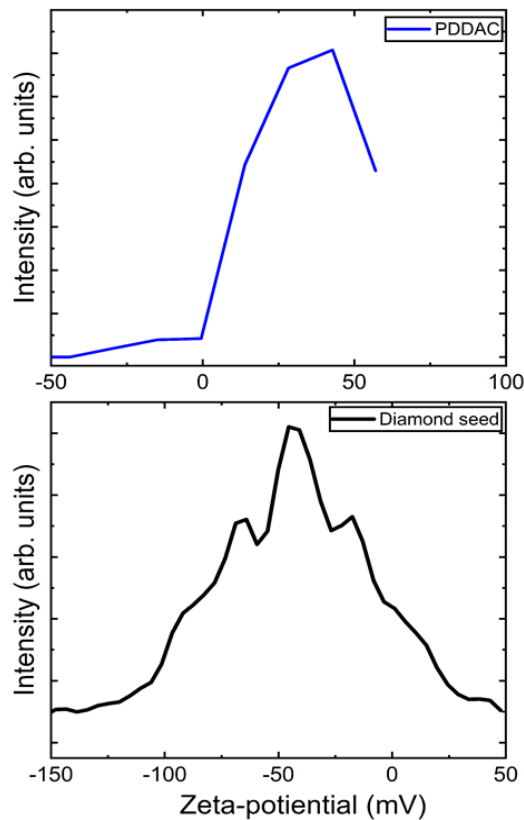


Figure 3.1. Zeta- potential measurement on PDDAC and diamond seeds using dynamic light scattering technique.

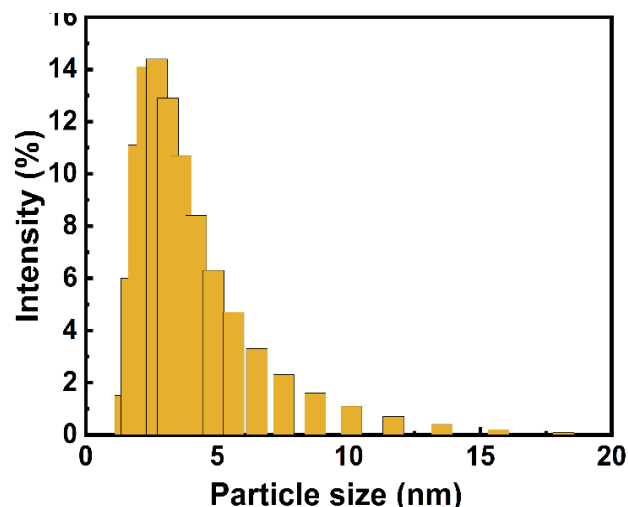


Figure 3.2. Dynamic light scattering data of the diamond nano-particle size distribution in the solution.

The results for measurement on zeta-potential for polymer and diamond seed is shown in Figure 3.1. Based on the measurements, the back scattering intensity for the zeta-potential measured for the diamond seeds and the PDDAC polymer is found maximum at ~51 mV and ~-47 mV, respectively. The average zeta potential calculated based on five different sets of measurements for diamond seeds and PDDAC polymer are -47.0 ± 2.1 mV and 51.2 ± 11.4 mV, respectively. These measurements show that there is a large potential difference between the polymer and the diamond nanoparticles that promotes self-assembly of the nanoparticles on the polymer coating for achieving high diamond seed density. Similarly, the size of the nano-diamond seeds was measured from the back scattering technique using Malvern Zeta-sizer. The result is shown in Figure 3.2. The diamond particle sizes are tightly clustered below ~15 nm with the maximum in the distribution occurring at the hydrodynamic size of ~3 nm.

Dip electrostatic seeding process. For the process development, the dip electrostatic seeding approach developed by Girard et al.[28] was the starting reference point. The principle for the electrostatic seeding approach is to bond diamond nano-seeds on the polymer coated substrate by weak van-der Waals force to achieve a dense nano-diamond seed density. The basic steps for the electrostatic dip seeding approach used for this project is shown in Figure 3.3.

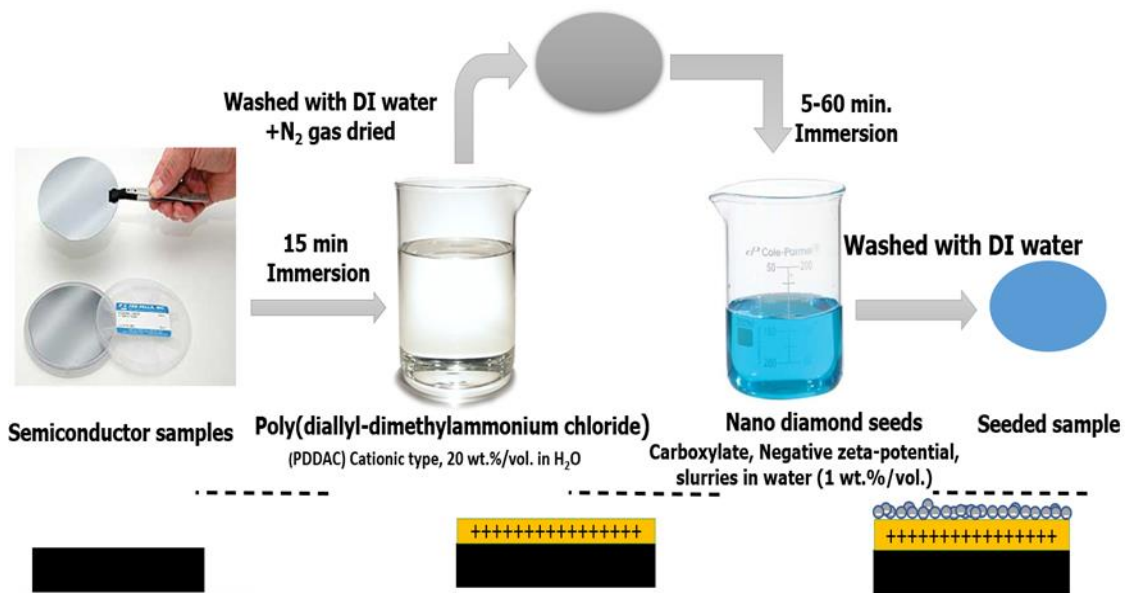


Figure 3.3. Dip electrostatic seeding approach for diamond seeding on non-diamond semiconductors.

First, the semiconductor samples were rinsed with acetone, methanol, and isopropanol prior to diamond seeding to remove any organic contaminants on the surface. The cleaned sample was then dipped on the PDDAC polymers for ~5-15 min to make a uniform polymer coating and functionalize the semiconductor surface with positive charge. The polymer coated samples were flushed with de-ionized water to remove the

thick polymer layers. The thickness of the polymer was not considered for this seeding approach. The wafers were then dried with N₂ gas and then dipped in the nano-diamond slurries with negative zeta-potential. Here the zetapotential difference was maintained between the polymer (positive) and the nano-diamond slurries (negative). The immersion time in the nano-diamond slurry was varied between 5-60 min. The samples were then flushed with water in order to remove the weakly bonded nano-diamond seeds from the surface and again dried with N₂ gas. The seeded sample was characterized with atomic force microscopy (AFM) using tapping mode with a Pt-tip to determine the diamond seeding density and surface morphology.

Figure 3.4(a) represent the (5×5) μm² scan for the seeded Si substrate from dip electrostatic seeding process explained earlier. Nano diamond seed clustering was observed on the seeded sample. The cluster size varies non-uniformly from a minimum 10 nm to maximum 150 nm as seen from the line profile on the AFM image shown in Figure 3.4(b). The nano-diamond seed clusters are due to the polymer peeling from the substrate surface due to its water solubility during the seeding process. The polymer that has peeled then forms a three-dimensional island where nano diamond seeds attach electrostatically to form clusters.

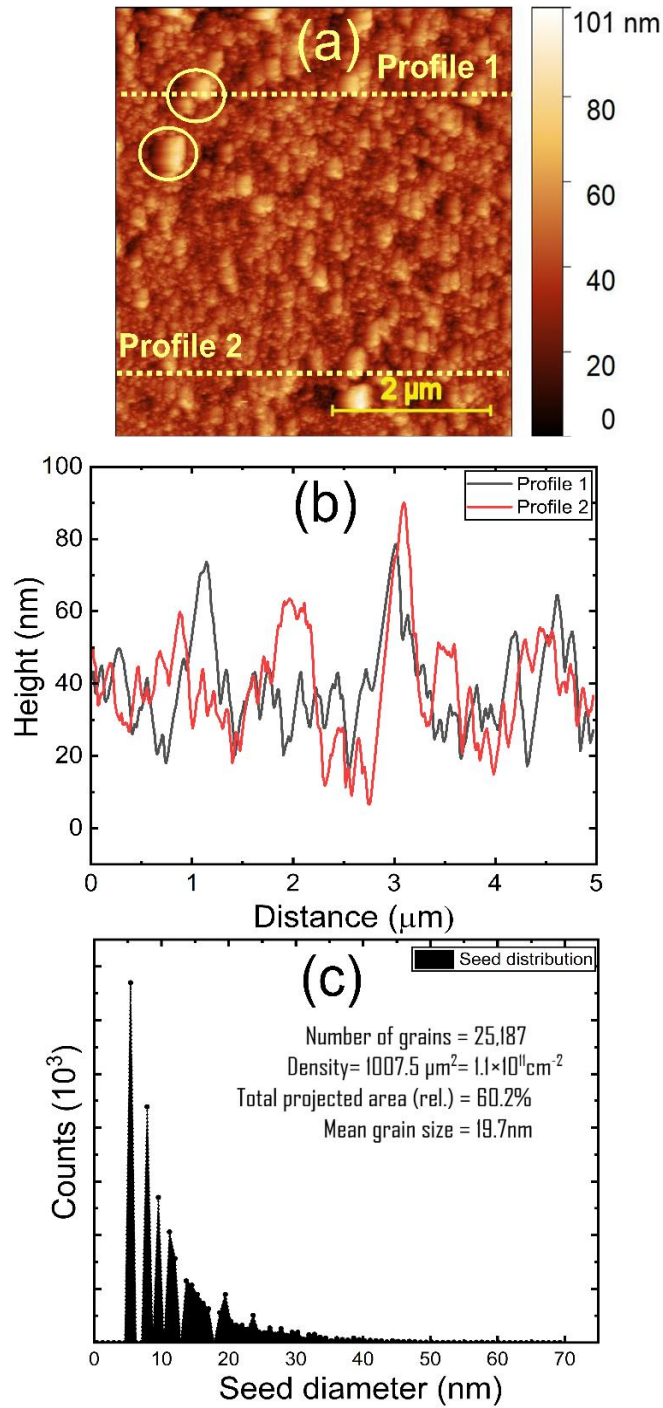


Figure 3.4. (a) $(5 \times 5) \mu\text{m}^2$ AFM scan from the seeded Si substrate from dip electrostatic seeding approach (b) Line profile from AFM images shown in (a) and (c) Diamond nano-seeds distribution from AFM images measured from scanning probe microscope image processing software Gwyddion.

The statistical data for size, density, number, and total projected area covered by nano-diamond seeds on the seeded samples were analyzed by using scanning probe microscopy (SPM) data analysis software Gwyddion [106]. It's a multiplatform software for SPM data analysis. It allows users to execute all of the essential actions required for a proper examination of SPM data. Basic visualization of SPM data, such as false color representation, shading, edge detection, profile extraction and treatment, data filtering, and so on, are among the many capabilities available. For our samples, we used Gwyddion to create a mask for identifying each individual nano-diamond seeds from seeded substrate. The marking of grains was properly adjusted by removing the defects on the scans such as outliers and scars/ strokes based on water shield algorithm [28]. The operation of masked data was converted into the statistical data to calculate the mean grain size, total area covered by the seeds, nano-seed counts and density.

Figure 3.4(c) show the diamond nano-seed distribution from $(5 \times 5) \mu\text{m}^2$ AFM scan, shown in Figure 3.4(a), analyzed using Gwyddion software. From analysis, we found that the seed density calculated was $\sim 10^{11} \text{ cm}^{-2}$ with $\sim 60\%$ projected area covered by the diamond seeds. We achieve dense seed density on the substrate by this approach, but the clustering of nano-diamond seeds on the seeded substrate is expected to impact uniform nucleation of diamond during HFCVD growth. Thus, this approach was modified by developing an innovative approach called the mixed electrostatic seeding process.

Mixed electrostatic seeding process. Based on the analysis of the dip electrostatic seeding process; it was concluded that the clustering of nano-diamond seeds on the seeded substrate should be minimized in order to improve the diamond nucleation process during HFCVD growth. The possible cause of seed clustering on seeded substrate was hypothesized to be the water solubility of PDDAC polymer causing polymer peeling during diamond seeding. The dip electrostatic seeding approach was modified, as shown in Figure 3.5.

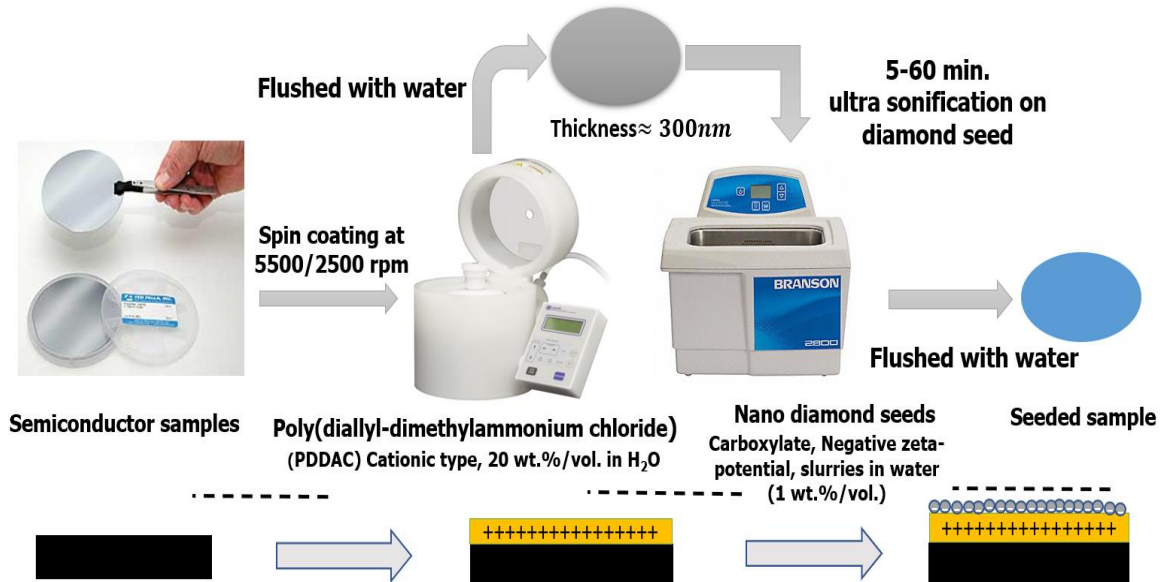


Figure 3.5. Modified dip electrostatic seeding approach for diamond seeding on non-diamond semiconductors.

For this seeding process, the polymer thickness on the substrate is optimized prior to diamond seeding. A thin uniform polymer is coated on the substrate by the spin coating technique. ~ 2.5 ml of PDDAC polymer was dispensed on the substrate and

coated uniformly by spin coater with spin parameter of 5500 rpm speed and 2500 rpm acceleration. The polymer thickness after coating was $\sim 1.9 \mu\text{m}$. The polymer thickness could then be reduced layer by layer by $\sim 300 \text{ nm}$ by multistep water flush. The substrate was then soft baked at $50 \text{ }^\circ\text{C}$ for 10 sec. The polymer coated substrate was immersed in the nano-diamond seed slurry and sonicated for 5-60 min. The sonication process is expected to reduce aggregation and potential void formation due to peeling of nano-diamond patches after prolonged seeding times. Following the seeding, all samples were rinsed with water and lightly dried with N_2 gas to remove poorly attached seeds from the substrate surface.

The seed coverage on the Si substrate with different submerging/sonication on the nano-diamond slurries were analyzed by varying the sonication time from 5-60 min with 5 min time interval. The AFM morphology for the diamond seed coverage with different sonication is shown in Figure 3.6(a)-(l). The seed coverage on the Si substrate increases continuously with increasing the submerging and sonication time on nano-diamond slurries. The seed clustering was found to be minimized significantly with this approach, using the sonication process. A few nano-diamond agglomerates can still be observed across a few positions within the seeded samples. The increasing seed coverage with increasing sonication indicates the change of seeding density on the samples. The profile height for the seeded samples measured by AFM increases continuously with increasing sonication time. After 40 min of sonication, the sample surface was found to be completely covered with diamond nano-seeds and no significant change of surface morphology was observed by AFM.

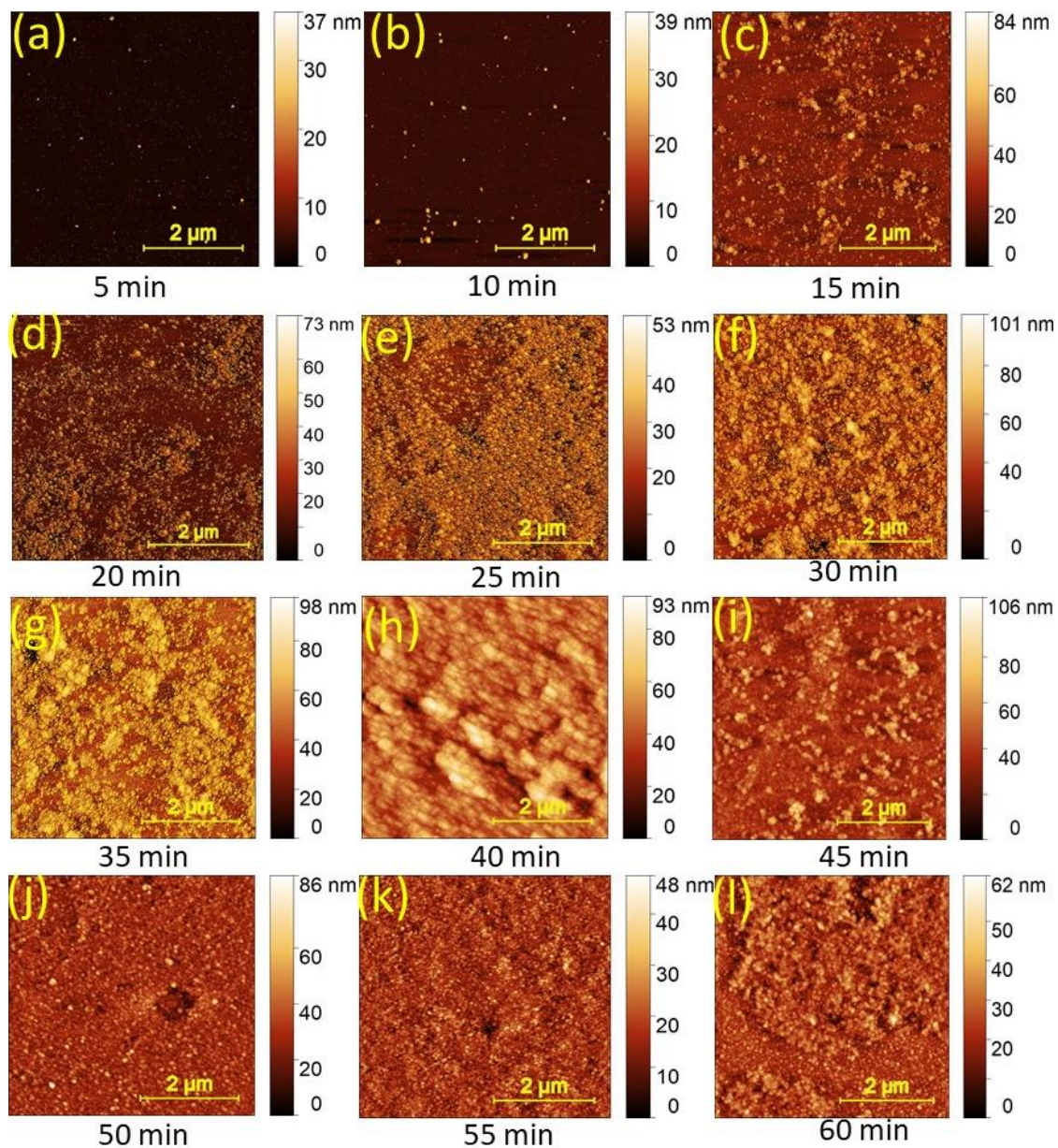


Figure 3.6. AFM morphology of seeded Si substrate showing variation on nano-diamond seed coverage on Si substrate with different sonication time.

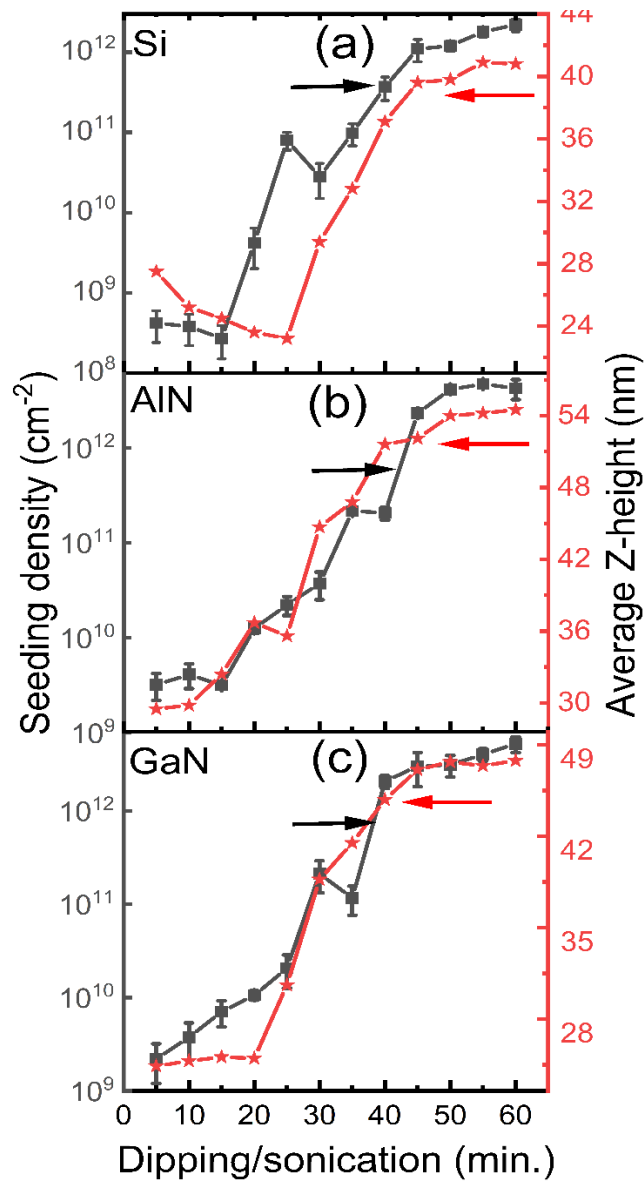


Figure 3.7. Seeding density variation with sonication time on nano-diamond slurries on (a) Si, (b) AlN and (c) GaN.

Seeding density was calculated from AFM images over at least three different positions on the samples by using SPM image processing Gwyddion software, explained earlier. Figure 3.7(a) show the variation of nano-diamond seeding density on Si with changing sonication time from 5-60 min in the nano-diamond slurry. Based on the

observations from AFM of surface morphology, shown in Figure 3.6, and seed density calculation, the nano-diamond seed density increases with increasing sonication time. The seed density changes continuously from $\sim 10^8 \text{ cm}^{-2}$ to $\sim 10^{12} \text{ cm}^{-2}$. The seed density change is linear until 45 min sonication. After 45 min the seed density remained nearly constant at $\sim 10^{12} \text{ cm}^{-2}$. It is deduced that the nano-diamond seeds have saturated the Si substrate resulting in maximum seed density. The AFM profile height also increased with increasing sonication time and then remained constant after 45 min. The seeding process was then optimized for surfaces such as AlN and GaN, with results for the seeding density as was found for Si substrate. The results for seeding density measured with sonication time is shown in Figure 3.7(b) and (c). These data indicate that the seeding process is also applicable for other substrates and independent of its surface charge and morphology.

Figure 3.8 show the morphology of Si, AlN and AlN surface before and after the diamond seeding. All samples before the diamond seeding were smooth with average surface roughness $< 1 \text{ nm}$, as shown in Figure 3.8(a)-(c). The surface was completely and uniformly covered with nano diamond seeds without voids or space, shown in Figure 3.8(d)-(f). The measured seed density for Si, AlN and GaN is found to be $2 \times 10^{12} \text{ cm}^{-2}$, $3.2 \times 10^{12} \text{ cm}^{-2}$ and $3.1 \times 10^{12} \text{ cm}^{-2}$, respectively. This seeding density is maximized and achieved for first time with this approach.

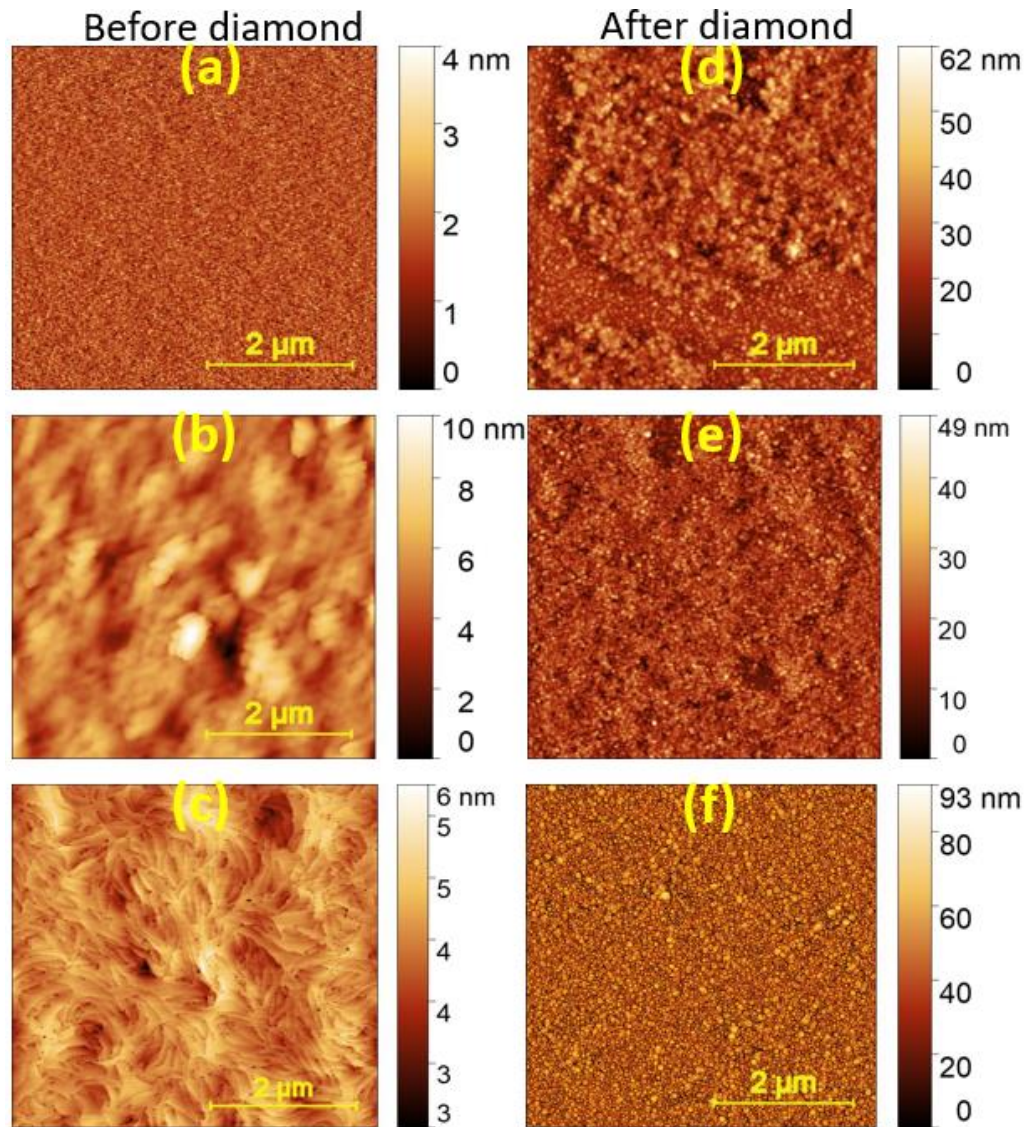


Figure 3.8. (a)-(c) Morphology of Si, AlN and GaN surface respectively prior to diamond seeding (d)-(f). Morphology of Si, AlN and GaN surface after diamond seeding with mixed electrostatic approach with 60 min sonication.

Summary

Diamond seeding density is optimized on different semiconductor substrates by an electrostatic seeding process. Dip electrostatic seeding helps to bond diamond nano-seeds on the polymer coated substrate electro statistically. A maximum seeding density of

$\sim 1 \times 10^{11} \text{ cm}^{-2}$ on Si substrate was achieved using the dip electrostatic seeding approach. The clustering of nano-diamond seeds due to polymer peeling during seeding was found to be a major problem with this seeding process. Subsequently, the seeding process was modified and optimized by first coating a thin polymer on the semiconductor surface and then sonication for diamond seeding, thereby substantially reducing seed clustering and the problem of polymer peeling during seeding. The optimized seeding process achieved the maximum seeding density of over $\sim 10^{12} \text{ cm}^{-2}$ on different semiconductor surfaces such as Si, AlN and GaN.

IV. EFFECT OF SEEDING DENSITY ON THE GROWTH OF DIAMOND FILMS BY HOT-FILAMENT CHEMICAL VAPOR DEPOSITION FROM SPARSE TO DENSE RANGE

In this chapter, a systematic study is reported of the effects of nano-diamond seeding density on the growth, quality, and morphology of diamond films. A process is described to examine nano-diamond seeding densities 4×10^8 , 8×10^{10} and 2×10^{12} cm^{-2} on silicon wafers. The diamond film is grown using hot-filament chemical vapor deposition with $\text{CH}_4/\text{H}_2/\text{O}_2$ feed gases and varying growth time to determine properties at coalescence and as thickness increases. Polycrystalline morphology is examined by scanning electron and atomic force microscopy. Both vertical and lateral growth rates are found to be higher for sparse seeding prior to coalescence. Following coalescence, the growth rate is similar for all densities. Development of polycrystals is found to be influenced by the initial growth with smaller mean lateral size at higher seeding density and reduced surface roughness that also improves with thickness to reach $\lesssim 90$ nm at a thickness of $6.4 \mu\text{m}$. Crystal quality is examined by micro-Raman spectroscopy from the sample surfaces and line images from cross-sections. Narrowing of the diamond phonon peak show material quality to improve with thickness, at a given seed density, and as density increases. Concomitant improvements are seen from the relative intensity of the diamond phonon and Raman bands from non-diamond carbon. Cross-section micro-Raman results suggest improved diamond film quality and crystallinity near the substrate interface as well as at the growth surface for the film grown with 2×10^{12} cm^{-2} seed density compared to 4×10^8 and 8×10^{10} cm^{-2} . X-ray photoelectron spectroscopy confirms these trends at the diamond surface.

Introduction

The continued development of methods for growing diamond films by chemical vapor deposition (CVD) is important for applying key material properties including ultra-wide band gap, high hardness, chemical inertness, and high thermal conductivity [10,45]. The CVD method generally starts with a process in which diamond seeds are distributed across a substrate and serve as growth initiation sites, as discussed in previous chapters. The uniformity of diamond films, with acceptable surface roughness, desired grain size, and other properties, depends strongly on the initial seeding density [95]. Surface pretreatments to achieve high seeding density have also been reported [28,83,94,96,102].

The hot filament CVD (HFCVD) method for growing diamond films involves dissociation of methane (CH_4) in the presence of energetic hydrogen atoms, both activated by high filament temperature and at low chamber pressure (5-100 torr) [20,62]. Control variables in this method are precursor concentration (CH_4 , H_2 , or O_2), temperature, pressure, and separation distance from filament array to substrate. Seeding density also plays a crucial role for determining the growth morphology and film quality in the diamond film [107–109].

The diamond film growth mode depends on seeding density [10,95]. At low seeding density (10^4 - 10^6 cm^{-2}), with high surface energy, the diamond films grow three dimensionally in a Volmer-Weber growth mode [110]. However, for high seeding density ($>10^8$ cm^{-2}), the diamond exhibits van der Drift competitive growth during coalescence into thicker films [111]. There are few reports comparing growth for diamond at very high seeding density. Tang et al. [95] studied the effect of diamond seeding density (10^4 to 10^{10} cm^{-2}) on the morphology, growth, and texture of diamond film. They report that

high seeding density plays a role in improving quality and texture on diamond film.

Sarangi et al. [109] studied the growth mechanism of diamond film with different seeding density using metal nano-seeds and other diamond seeding process, but they did not extensively study the impact on film morphology, growth rate, and quality of diamond.

Gilbert et al. [112] studied the effect of seeding density (from 10^8 to 10^{10} cm^{-2}) on the quality of thin films ($< 1 \mu\text{m}$) grown by electron–cyclotron resonance plasma at low pressure.

We present here a comparative study of the growth rate, grain size, and quality of diamond films grown at seed densities 4×10^8 , 8×10^{10} , and 2×10^{12} cm^{-2} . High seeding density is achieved using a polymer coating followed by either dip coating, for the two low densities, or extended sonication in the nano diamond solution to achieve the high seeding density. Here, the polymer adheres to the substrate and the nanoparticles adhere to the polymer due to their large zeta-potential difference. The approach requires no functionalization of either the seeds or the substrate. Sequential growth is carried out to allow the study of the diamond films in the early stages (30 min) and after total growth times of 6 and 16 h. Physical properties are characterized using scanning electron microscopy (SEM), transmission electron microscopy (TEM), atomic force microscopy (AFM), micro-Raman spectroscopy, and X-ray photoelectron spectroscopy (XPS). The growth, morphology, and quality of diamond film is analyzed across the entirety of the film thickness from the substrate interface region to the diamond surface.

Experiment and Results

Seeding, diamond growth, and characterization methods. A 100 mm (111)-oriented, p-type silicon substrate was used for these experiments. The substrate was cleaved into four pieces for sample preparation. The detail of diamond seeding process is explained on Chapter III. For diamond seeding, a cationic poly (diallyl dimethylammonium chloride) or PDDAC polymer with positive zeta-potential and nano-diamond slurries with negative zeta potential are employed. The PDDAC polymer had molecular weight 100,000-200,000 g/mol, 20 wt.% water, pH ~ 7 (Sigma Aldrich, St. Louis, MO, USA). The diamond nanoparticles were commercially available carboxylate nano-diamond (Adamas Nano, Raleigh, NC, USA) and was specified as monodispersed diamond nano particles at 1 wt.% in deionized (DI) water, with solution pH ~ 7. To obtain different diamond seeding densities, a modified polymer assisted dip seeding technique reported by Girard et al. [28] was developed.

Prior to seeding, the size of diamond nanoparticles and zeta-potential for both diamond seeds and PDDAC polymer were measured with a dynamic light scattering (DLS) technique using a Malvern Zetasizer Nano ZS equipped with a 633 nm laser. Back scattering configuration was used to determine average particle size based on 100×30 s scans and zeta potential of 300 scans. Results are shown as a histogram in Figure 4.1(a). The diamond particle sizes are tightly clustered below ~ 15 nm with the maximum in the distribution occurring at hydrodynamic size ~ 3 nm. The average zeta-potential measured for nano-diamond particles was -47.0 ± 2.1 mV.

Three samples (S-1, S-2, and S-3) were seeded with two different procedures to achieve different seeding densities. The silicon was rinsed in isopropyl alcohol and dried in nitrogen gas. All samples were then coated with PDDAC polymer by spin coating at 5500 rpm for 30 s. Following this, the polymer thickness was $\sim 1.9 \mu\text{m}$. S-1 and S-2 were then submerged in nano-diamond seeds solution for 5 and 25 min, respectively. In contrast to the procedure used for S-1 and S-2, the PDDAC-coated sample S-3 was gently flushed with DI water (room temperature) several times to reduce the polymer thickness to $\sim 250 \text{ nm}$. The sample was then ultrasonicated in the nano-diamond slurry for 60 min. The ultrasonication reduces aggregation and potential void formation due to peeling of nano-diamond patches at prolonged seeding times. Following the seeding, all samples were rinsed with water and lightly dried with N_2 gas to remove poorly attached seeds from the substrate surface. For DLS measurements, the PDDAC polymers was further diluted with 1 mM aqueous KCl prior to zeta-potential measurement. The small amount of KCl acts as a background electrolyte to ensure that low impurity concentrations do not adversely affect the DLS measurement [105]. The average zeta-potential for the PDDAC polymer was $51.2 \pm 11.4 \text{ mV}$. This verifies the large potential difference, between the polymer and the diamond nanoparticles, that promotes self-assembly of nanoparticles on the polymer coating for achieving high diamond seed density [96].

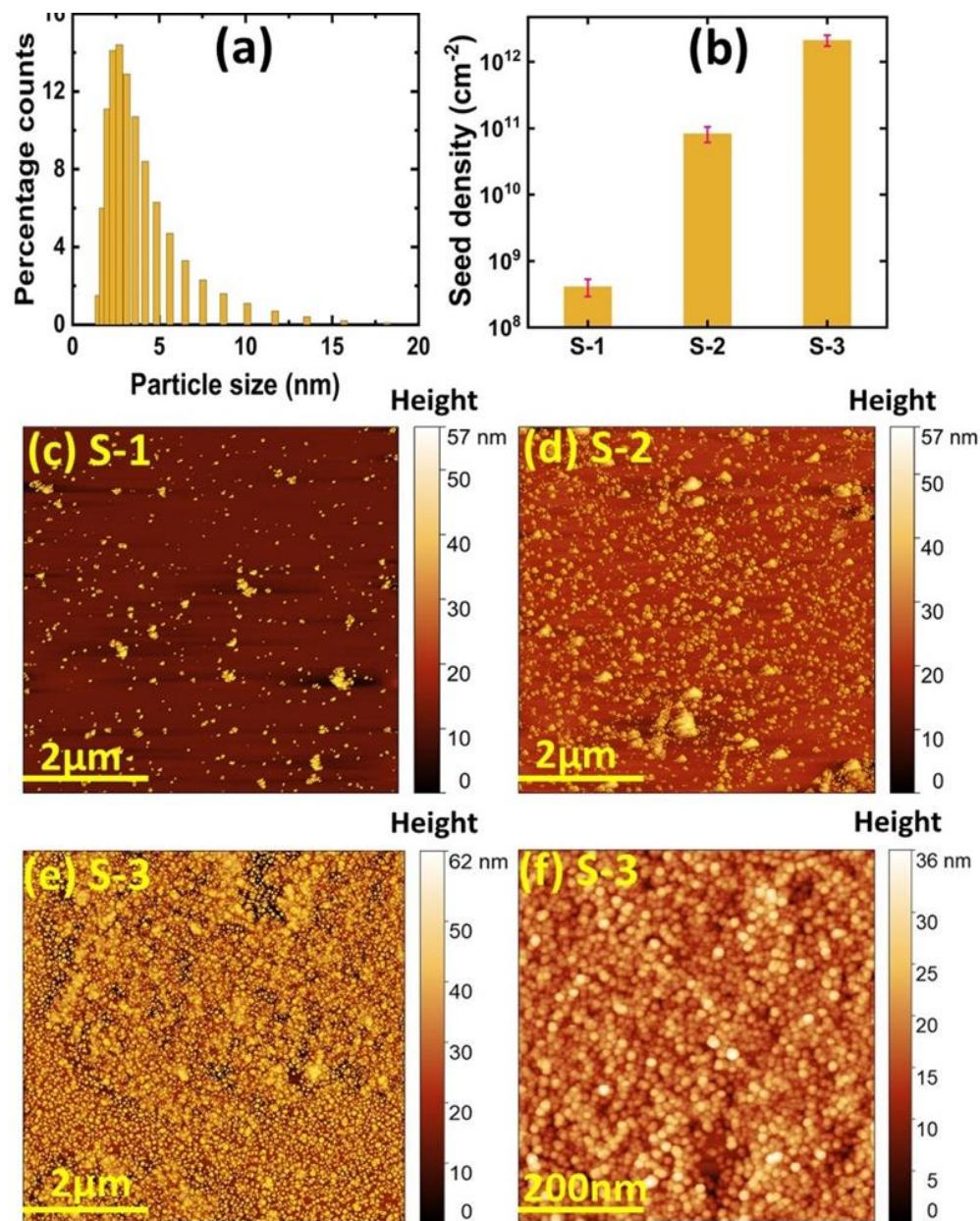


Figure 4.1. (a) Dynamic light scattering data of particle size distribution in solution. (b) Average diamond seed density based on analysis of at least three AFM images for each sample. Uncertainty ranges are standard deviations from analysis of multiple AFM scans. (c)-(e) AFM images of seeded Si samples S-1, S-2, and S-3, respectively. (f) AFM image of S-3 over smaller range.

The diamond seed density was measured using AFM images identifying particles on the surface using the Gwyddion scanning probe microscopy (SPM) analysis software [106] following the approach described in previous chapters for determining diamond seeding densities [96]. Results are summarized in Figure 4.1(b) based on a minimum of three individual $5 \times 5 \mu\text{m}^2$ AFM scans from each sample, such as what is shown in Figure 4.1(c)-(e). Additionally, images using smaller scan ranges, $500 \times 500 \text{ nm}^2$ as shown in Figure 4.1(f), were analyzed and good agreement for particle densities was verified. The AFM images clearly show diamond seed coverage is far lower on S-1 and maximum on S-3 with average seed density of approximately 4×10^8 , 8×10^{10} , and $2 \times 10^{12} \text{ cm}^{-2}$, for the three samples. Even with the ultrasonication process, there is evidence for some seed clustering on the surfaces. One possible reason is the water solubility of PDDAC, that may cause some peeling thereby resulting in larger polymer particles adhering to the surface when the samples are dipped in the diamond slurry. The diamond seeds attached to those polymer particles may then appear as nano-particle agglomerates. The formation of such nano-particle agglomerates of size $42.2 \pm 21.4 \text{ nm}$ can be seen from the AFM images in Figure 4.1(c) and (d) for S-1 and S-2, respectively. In contrast, we find the S-3 seeding to be more uniformly distributed and denser with only small clusters, as shown in Figure 4.1(e). In all cases, the measured seed density obtained from AFM scans is less than the maximum $4.6 \times 10^{12} \text{ cm}^{-2}$ predicted with a seed diameter of 5 nm using an idealized close-packing approach [87].

For the diamond growth, all samples were simultaneously positioned inside the HFCVD system. Power (6 kW) driven through the array of nine tungsten wires—24 cm long and 0.25 mm diameter— resulted in a 2200 °C filament temperature. The water-cooled rotating substrate holder was positioned 6 mm from the tungsten wire array to produce a substrate temperature of 720–750 °C as measured by IR pyrometer. Source gases were 60 sccm CH₄ (3%), 2000 sccm H₂, and 3 sccm O₂, with chamber pressure maintained at 2773 Pa (20.8 Torr). The growth comprised sequential steps to determine time to coalescence and for extensive characterization at total growth times of 30 min, 6 h, and 16 h.

After each growth step, the samples were characterized by SEM (FEI Helios 400) in-plane and cross-section views to assess the film uniformity, layer thickness, and to examine the diamond/Si interface. Cross-sectional TEM (Thermo Fischer Talos 200i) was used to study the interface between the diamond/Si for sample S-3. Samples were prepared for TEM by focused ion beam milling operating at 200 kV. AFM (Bruker Dimension ICON) was used in tapping mode to check the seeding density prior to growth and to evaluate the root-mean square (RMS) roughness and grain size following diamond growth.

Diamond phase purity and quality across the diamond film was ascertained by micro-Raman measurements with ultraviolet (UV) excitation wavelength 363.8 nm [80,113]. At this excitation wavelength, the diamond fluorescence is lower than when measuring in the standard visible-wavelength range. The laser excitation was focused into a line approximately 10- μ m long and 2- μ m wide using a 100 \times objective (NA 0.40) and acquisition time of 60 s to collect the spectra. Visible micro-Raman spectra (excitation

wavelength 532 nm) were used to measure the samples along cross-section planes using a Horiba (Lab RAM) system. The nominal spot diameter was $\sim 2 \mu\text{m}$ utilizing a $\times 100$ objective lens with NA 0.90. For all micro-Raman cross-section measurements, a coupon $\sim 10 \text{ mm} \times 3 \text{ mm}$ was vertically affixed on a translational stage illuminating the freshly cleaved edge with the excitation. The sample position was stepped every $1 \mu\text{m}$ along the growth direction to obtain line images. In all cases, spectra were collected to capture the silicon and diamond $O(\Gamma)$ -symmetry phonon lines and the broad non-diamond carbon (NDC) bands in the $1450\text{--}1600 \text{ cm}^{-1}$ range. The visible cross-section data were cross checked by measuring the samples by UV micro-Raman spectroscopy using point focus along the cross-section plane for diamond film. A natural diamond was measured for reference [113]. Quantitative information was obtained by fitting the diamond Raman band using a Lorentzian line shape. Intensities from the disordered carbon were obtained by integrating from 1000 to 1700 cm^{-1} with background subtracted and eliminating the diamond phonon intensity using the fit results.

XPS (Thermo Fisher Scientific Nexsa) measurements were carried out using an Al $K\alpha$ source (photon energy 1486.6 eV) at ultra-high vacuum (base pressure $\sim 2 \times 10^{-9}$ mbar) to analyze the diamond surface quality. Measurements were taken with and without an argon-ion etch clean of the diamond surface. High resolution spectra were collected with pass energy of $\Delta E = 50 \text{ meV}$ and step size of 100 meV . Deconvolution of the C $1s$ peak was performed by fitting a mixture of 70:30 Gaussian and Lorentzian peaks after background subtraction [114].

Diamond morphology, thickness, and grain size. Presented in Figure 4.2 are representative SEM images for the different seeding densities studied (columns) and HFCVD growth times (rows). Note that scale bars within rows are identical but vary down the columns. Coverage for samples S-1, S-2, and S-3, respectively, is examined using images such as those shown in Figure 4.2(a)-(c) following 30 min of growth. Well separated diamond crystallites are seen for sample S-1, Figure 4.2(a), with mean lateral size $\sim 0.1 \mu\text{m}$ for an approximate initial lateral growth rate of $\sim 0.1 \mu\text{m/h}$. Assuming the initial lateral growth rate for each sample is the same as what may be estimated for S-1, $\sim 0.1 \mu\text{m/h}$, the seeding density needed to achieve coalescence in 30 min growth time is estimated to be $\sim 4 \times 10^{10} \text{ cm}^{-2}$. At the intermediate seeding density of $8 \times 10^{10} \text{ cm}^{-2}$ for S-2 the diamond crystals are seen in Figure 4.2(b) to partially coalesce, presumably where seeds were higher in density as was seen in Figure 4.2(d). The mean lateral size of these diamonds is estimated to be $\sim 0.09 \mu\text{m}$. Full coalescence of diamond crystals is seen for S-3 at high seeding density $2 \times 10^{12} \text{ cm}^{-2}$ with mean grain size $\sim 0.08 \mu\text{m}$ in Figure 4.2(c). When considering the lateral growth rate above, for isolated crystals, the $0.08\text{-}\mu\text{m}$ grain size here suggests coalescence in the very early stages of growth for this high seeding density.

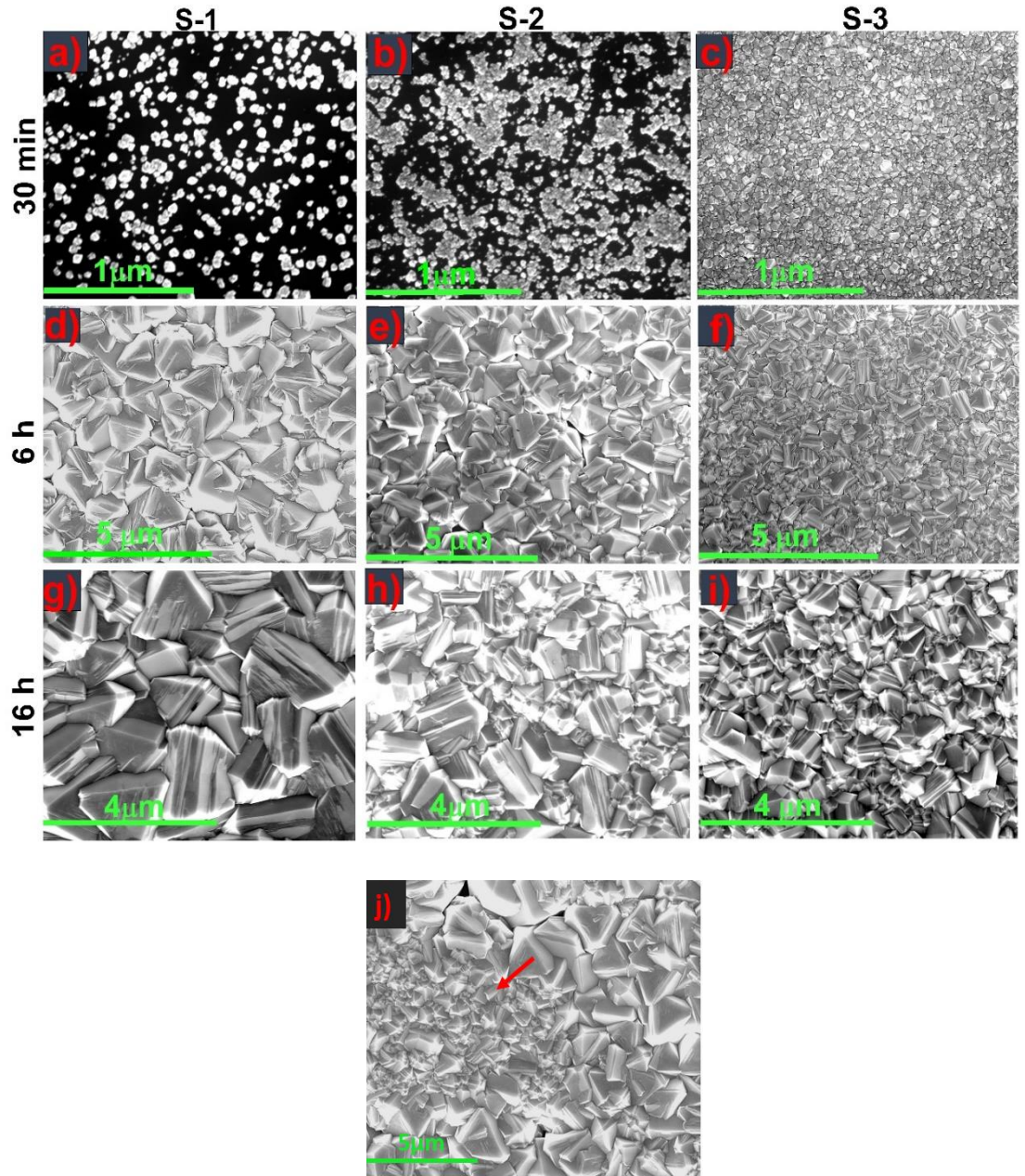


Figure 4.2. SEM images for diamond film grown on sample S-1, S-2, and S-3, respectively after (a)-(c) 30 min (d)-(f) additional 5.5 h (total 6 h) and (g)-(i) additional 10 h (total 16 h). (j) Region with smaller grains seen on S-1 after 6 h.

Figure 4.2(d)-(f) show the corresponding SEM images for S-1, S-2, and S-3, respectively, following total growth time of 6 h. Well-developed diamond crystals having the stable octahedral, rhombic dodecahedron, and truncated octahedron shapes [18] were formed on all samples, but with variations in morphology for the different seed densities. The lower density diamond seeds on S-1 permit diamond crystals to develop three dimensionally in a Volmer-Weber growth mode [115,116] to produce large ($\sim 1 \mu\text{m}$) diamond crystals, Figure 4.2(d). Regions with fewer diamond grains and smaller size, shown by red arrow in Figure 4.2(j), were found in some regions of S-1. This is attributed to slow development of diamond grains on sparsely seeded areas or nano-particle clusters, as described earlier. Once coalescence takes place, individual crystal sizes are expected to grow according to the van der Drift model. The diamond grains in Figure 4.2(e) for sample S-2 are substantially larger than following 30 min. However, even after 6-h growth the diamond crystals on S-2 remain noticeably smaller than for S-1. Growth at the intermediate seeding density represents, after 6-h growth time, a transition from the early three-dimensional Volmer-Weber conditions to van der Drift mode. The diamond film shown in Figure 4.2(f), for S-3, is found to be more uniform and compact with smaller grains, a result we attribute to the dense seeding, and corresponds to a situation dominated by early van der Drift mode.

Following the full 16-h growth time, we see in Figure 4.2(g)-(i) development of larger diamond crystals for each seeding density when compared with the corresponding shorter growth durations. Large and faceted diamond grains are present for S-1, in some cases exhibiting lateral dimensions in excess of $2 \mu\text{m}$. In transitioning to the higher seeding densities for samples S-2 and S-3, the average crystal size is successively

smaller. Since the growth chamber conditions were identical in all cases, the variations seen in crystal size stem from differences in seeding density and its impact on the ensuing growth mode.

Analysis from AFM images are shown in Figure 4.3(a) and (b). The diamond lateral grain sizes are summarized in Figure 4.3(a) for the 6- and 16-h growth experiments. The mean grain size is seen to decrease as seeding density increases, consistent with the discussion above based on SEM data. The increase in lateral grain size, with growth time, takes place in all samples. The lateral diamond grain size is maximum for sample S-1 due to the longer development of three-dimensional grains, as described earlier. The uncertainties shown correspond to standard deviations in grain sizes. The variation is maximum for S-1 and decreases with increasing diamond seeding density. This is due to earlier coalescence of diamond particles and slow transformation to van der Drift growth with increasing seed density. RMS roughness values, from the AFM scans, are shown in Figure 4.3(b) following 6- and 16-h growth. The overall trend is decreasing RMS roughness as seed density increases. Higher surface roughness is related to large grain size, for example in S-1. Sample S-3 is found to exhibit the best uniformity in grain size and lowest surface roughness compared to the samples grown using lower and intermediate seeding densities.

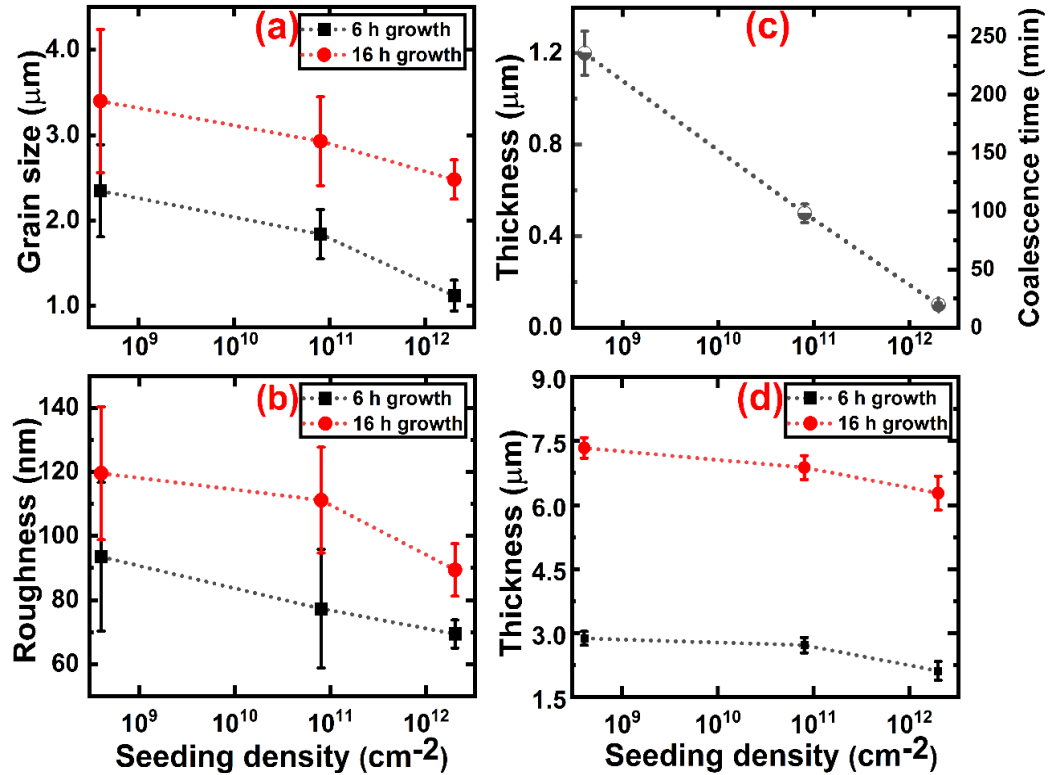


Figure 4.3. Average for at least three images of (a) grain size and (b) RMS roughness from AFM scans of diamond film on samples S-1, S-2 & S-3 after 6 h and 16 h growth. (c) Approximate coalescence time and measured thickness for diamond film at the point of coalescence with different seeding density grown with 3% methane. (d) Thickness of diamond film after 6 and 16 h growth taken from cleaved cross section SEM.

The time needed to achieve fully coalesced diamond film with different seeding density was also studied as shown in Figure 4.3(c). Establishing these factors in HFCVD is challenging since initial chamber conditions differ from what is achieved for the longer growth duration. It takes 240 min to obtain a coalesced polycrystalline diamond film on sample S-1. The thickness at full coalescence for S-1 is $1.2 \mu\text{m}$ implying a vertical growth rate of $0.30 \mu\text{m/h}$ when computed simply using total thickness and growth time. The nominal lateral growth rate is found to be comparable at $\sim 0.35 \mu\text{m/h}$. These rates are

relevant beyond the initial growth regime, discussed above, and correspond to pre-coalescence for which the Volmer-Weber model applies [117]. For S-2, it takes 120 min to obtain coalesced polycrystalline film with slightly lower vertical and lateral growth rates of $\sim 0.25 \mu\text{m/h}$ and $\sim 0.21 \mu\text{m/h}$, respectively. The slower rates for S-2 indicate that the van der Drift growth model [112] is applicable, as expected particularly close to coalescence. Micro-loading may also be a factor reducing the growth rate. For S-3 it took just 30 min to reach coalescence, at diamond thickness $\sim 100 \text{ nm}$, with a nominal vertical growth rate at the point of coalescence of $\sim 0.20 \mu\text{m/h}$ and lateral growth rate of $\sim 0.16 \mu\text{m/h}$. For this case, nearly the entire growth process is in the vertical van der Drift regime. The outcome of this analysis is the observation that the growth mode transitions from three- to one-dimensional (vertical) over the range of seed densities investigated and a relationship describing a decrease in thickness at coalescence with seeding density, as previously reported [95], but over a lower range of seed densities 10^4 to 10^{10} cm^{-2} . The coalescence properties will differ based on diamond growth conditions and deposition methods.

Diamond film thickness, based on SEM cross-sections, are shown in Figure 4.3(d) for the different seeding densities after 6 and 16 h growth. We observe that the grain size and roughness follow an increasing trend with diamond film thickness. The corresponding average growth rates, for respective samples S-1, S-2, and S-3, are determined to be 0.48, 0.45, and $0.33 \mu\text{m/h}$ following 6 h, and 0.52, 0.45, and $0.38 \mu\text{m/h}$ after 16 h growth. The higher growth rate for the samples with lower seed density is attributed to the early growth regime, as discussed in the previous paragraph. When considering the growth rates over the final 10-h time, between 6 and 16 h, the growth

rates are consistently $\sim 0.45 \mu\text{m/h}$. This is expected since, at this stage, the diamond surface present during the growth and the HFCVD conditions are consistent.

The post-coalescence growth rates for each seeding density can be explained according to the van der Drift evolutionary selection model [111]. For lower seed density sample, S-1, there is no, or less, competition between the grains during the early growth stage before coalescence and less competition and inter grain stress after they coalesce compared to samples with high seed density, S-2 and S-3. This allows the grains to grow randomly faster and more freely in both parallel and perpendicular directions on the silicon substrate. This leads to larger grain size and a thicker diamond film. However, there is substantial impingement and competition between the grains during the early growth stages for densely seeded surfaces. Generally, grains tend to grow along crystallographic planes at different rates [34] that, when coupled with random initial seed orientation, produces random normal and off-normal growth rates to the substrate direction. Thus, grains that are oriented predominately normal to the substrate propagate and survive while those that are oriented off-normal to the substrate are subsequently buried and their growth terminated. This explains the lower thickness and smaller grain size of the final film with higher seed density.

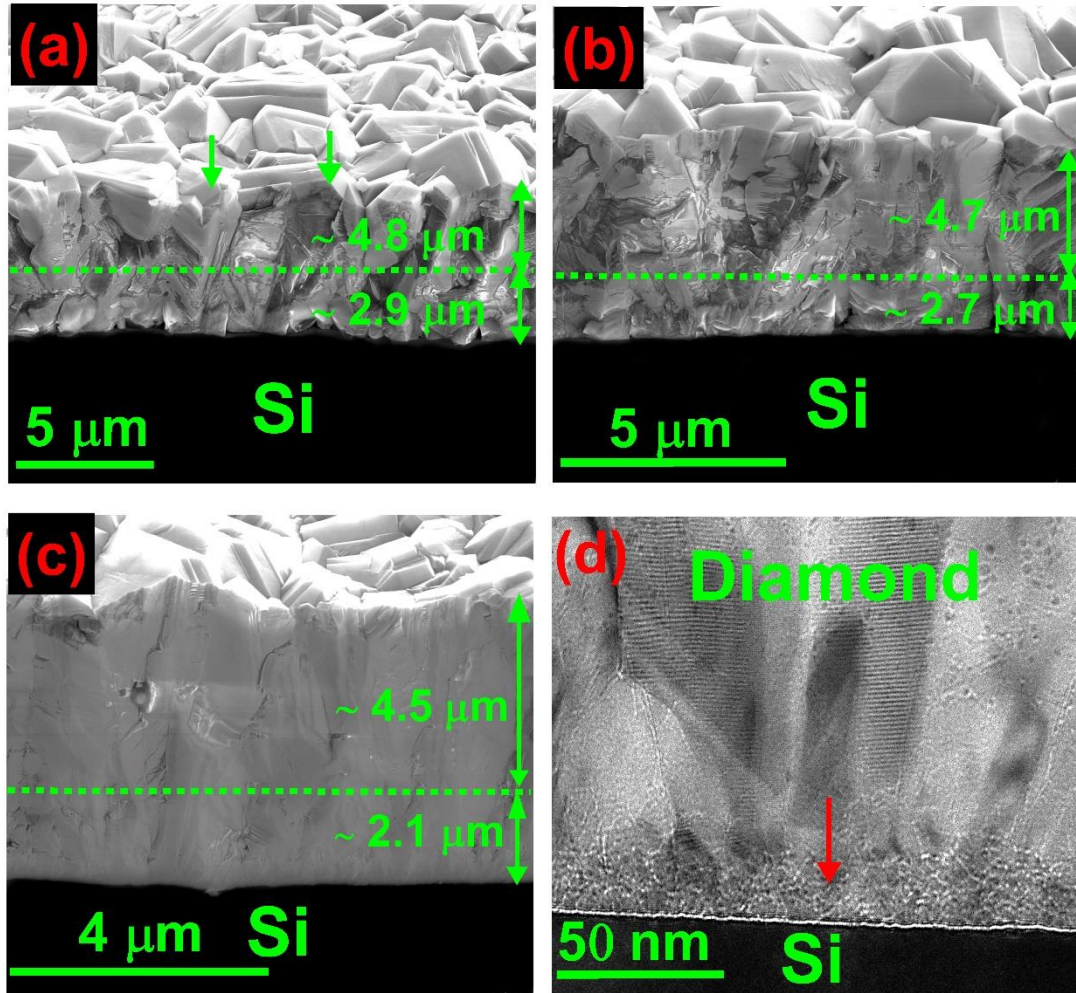


Figure 4.4. (a)-(c) Cross-sectional SEM images for samples S-1, S-2 and S-3, respectively, taken from cleaved samples. The arrows in (a) indicate columnar structure perpendicular to substrate surface. Horizontal dashed lines in (a)-(c) are corresponding thickness of diamond following 6-h growth and additional 10 h at each seeding density. (d) TEM cross-section for S-3 at the diamond/substrate interface.

Cross-section SEM measurements from cleaved samples were used to investigate the diamond morphology along the growth direction following 16-h growth. SEM images are shown in Figure 4.4(a)-(c) for, respectively, S-1, S-2 and S-3. A columnar structure perpendicular to the substrate is apparent in the upper portion of sample S-1 and indicated

by the arrows in Figure 4.4(a). These are due to the development of diamond crystals into larger grains with increasing thickness. The interface with silicon appears to be poorly developed, with the possibility of voids, that we believe to be formed when the isolated large grains coalesced for sample S-1. In contrast to S-1, the interface is improved on sample S-2 with better uniformity and little evidence of pores at the interface as shown in Figure 4.4(b). Figure 4.4(c) shows S-3 conditions result in an abrupt interface without the voids that appear in the other two samples. A cross-sectional TEM image for S-3 is shown in Figure 4.4(d). The image reveals the presence of small features, shown by the red arrow on Figure 4.4(d), approximately 3 nm in size and having total thickness ranging from 21 to 26 nm in this image. These small features are associated with diamond seeds. This suggests that the diamond seeding process does not form a monolayer. The uniform diamond growth and improved interface without pores is attributed to the dense diamond seeding of S-3. This dense seeding also leads to improved diamond properties, discussed next.

Crystallinity, quality, and stress on diamond film. The crystalline quality of diamond film was characterized using Raman spectroscopy through the plane and cross-section measurements.

In-plane Raman spectroscopy. Figure 4.5 shows the UV micro-Raman results collected for samples after different growth stages, i.e., 30 min., 6 h, and 16 h. For all samples, the sharp O(Γ)-symmetry phonon for diamond is seen with varying blue shifts [118] relative to the reference value we measure at 1331.9 cm^{-1} . The broad features from 1350 to 1450 cm^{-1} and 1500 to 1620 cm^{-1} correspond to the “D” and “G” bands that are present in non-diamond carbon (NDC) when present in either diamond-like or

graphitic phase [30,81]. The NDC may be composed of various disordered carbon having mixed sp^2 and sp^3 bonding configurations and is considered to degrade thermal conductivity of diamond films [118].

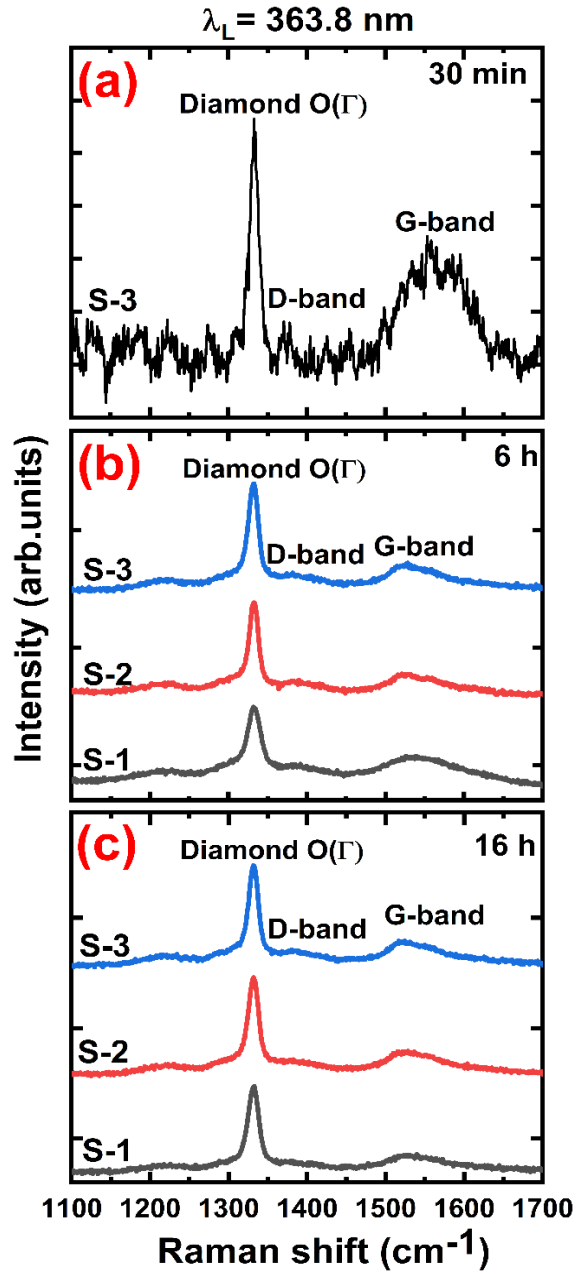


Figure 4.5. UV Raman spectra. (a) Diamond film grown on S-3 for 30 min. (b)-(c) Diamond film after 6 h and 16 h growth, respectively.

Figure 4.5(a) shows the Raman spectra of diamond film grown on sample S-3 for 30 min. The diamond peak is seen at 1333.3 cm^{-1} with full width at half maximum (FWHM) of 19.1 cm^{-1} . This is broad in comparison to the reference value of 6.3 cm^{-1} which may be the result of poor crystal quality in the initial growth stages and local variations in stress. The overall biaxial stress σ in the diamond film can be estimated from the Raman data using

$$\sigma = -k_R(\omega - \omega_0) \quad (15)$$

where $k_R = 0.567 \text{ GPa/cm}^{-1}$, [40,41,83] ω is the measured Raman frequency, and ω_0 is from the diamond reference at 1331.9 cm^{-1} . The stress value for the early growth data in Figure 4.5(a) correspond to stress of -0.79 GPa . Also observed is a broad NDC band that is commonly referred to as “G”. It is interesting that we see the broad “G” band in this spectrum with little evidence of a “D” band. This suggests that the NDC in S-3, at this stage of growth, is predominantly tetrahedral amorphous carbon [119]. Due to lack of diamond coalescence on samples S-1 & S-2, we were not able to measure the corresponding Raman spectra after 30-min growth to compare with S-3. The corresponding Raman spectra after the total 6-h diamond growth are shown in Figure 4.5(b), for S-1, S-2, and S-3, and in Figure 4.5(c) following 16-h. Prior to quantitative analysis, it may be observed that the spectra are consistent and that the “D” band of NDC is present along with the “G” band.

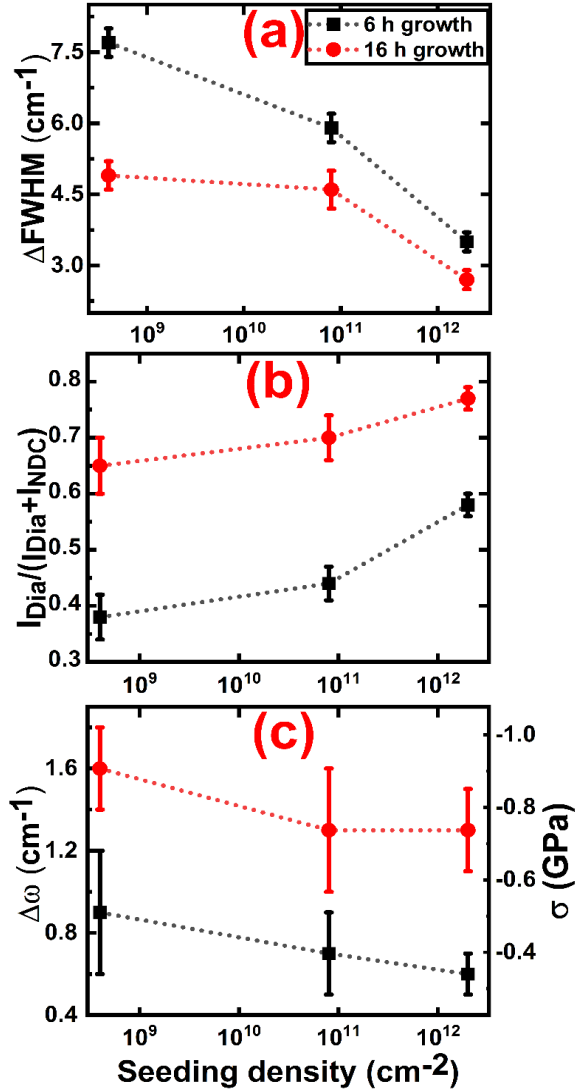


Figure 4.6. Analysis of UV Raman spectra, as a function of seeding density, following 6 and 16 h growth. (a) Relative FWHM, (b) ratio of integrated intensities, and (c) relative peak shift and corresponding stress.

The upper panel of Figure 4.6(a) shows the increase in diamond phonon line width relative to reference diamond. Narrowing of the diamond line is observed with increasing growth time for each seeding density. This narrowing is consistent with improvement in the diamond for greater thickness, i.e., distance from the initial growth

regime, that is commonly observed [28]. We also see narrowing with higher seed density at either growth time 6 or 16 h. Trends in relative volume fraction for diamond can be examined through $I_{Dia}/(I_{Dia} + I_{NDC})$, the ratio of integrated intensities of the diamond peak (I_{Dia}) to the total Raman intensity, where the I_{NDC} term is from the NDC bands, and following background subtraction [113]. Higher values (approaching unity) of this intensity ratio are indicative of better diamond quality. Trends for the samples are shown in the lower panel of Figure 4.6(b). The results confirm the expected improvement in the HFCVD layer with growth time. Moreover, the relative intensity increases systematically for the seeding densities studied here. The results in Figure 4.6(a) and (b) quantitatively show improvements in diamond quality and volume fraction, respectively, due to higher seeding density.

The presence of residual stress in the diamond may also be studied by examining the shift in the diamond phonon energy, shown in Figure 4.6(c). Intrinsic and thermal stresses are generated between the diamond film and substrate and may also be due to non-uniform development of diamond grains [120]. Intrinsic stress may originate from bonding at the diamond/silicon interface and also from the incorporation of defects and impurities in the diamond. Thermal stress is caused by the difference in the coefficient of thermal expansion (CTE) between diamond and Si substrate during the cooling cycle from growth temperature (720-750 °C) to room temperature. The CTEs are temperature dependent for diamond, $\alpha_D(T)$ [121], and silicon, $\alpha_{Si}(T)$ [122]. Stress from the CTE mismatch is calculated using

$$\sigma_{th} = \frac{E}{1 - \nu} \int_{T_i}^{T_f} (\alpha_D(T) - \alpha_{Si}(T)) dT \quad (16)$$

and found to be ~ -0.95 GPa when assuming the thin diamond layer experiences the full contraction imposed by the much thicker silicon. The $\sigma < 0$ denotes biaxial compressive stress on the diamond film. Based on this analysis, stresses in the diamond films are -0.5 ± 0.2 , -0.4 ± 0.1 and -0.4 ± 0.1 GPa, respectively, for S-1, S-2, and S-3 after 6 h growth. The corresponding stresses increased to -0.9 ± 0.3 , -0.7 ± 0.2 , and -0.7 ± 0.1 GPa after 16 h growth. The uncertainty values are calculated by measuring the stress at different positions across the samples and taking standard deviation. In each case the measured stresses are lower than the substrate-induced value computed above. Relaxation within the diamond may be due to the presence of voids and disorder including other carbon phases that are present. The observed increase in stress, from 6 h to 16 h growth, seen for each seeding density, is attributed to the evolution of bulk stresses in the diamond as the film continues to grow vertically through competitive growth (van der Drift) to produce a more contiguous layer, as evidenced in Figure 4.4. This does not account for contributions to the stress due to defects at grain boundaries. It is possible that the film is now moving into a regime where the intrinsic growth stresses dominate over any stress at the diamond/substrate interface.

Cross-section micro-Raman spectroscopy. The diamond film quality of each sample, with thickness ~ 7 μm , was also characterized by cross-section Raman spectroscopy. A series of cross-section micro-Raman spectra from measurements in the visible and UV are presented and compare below fitting summaries for these data. Spectra are shown from near the interface to the growth surface for each sample in Figure 4.7(a)-(c) from visible and (d)-(f) from UV micro-Raman measurements. For each sample the visible and UV spectra in Figure 4.7 were obtained from the same region but

not identical positions. All spectra exhibit the narrow diamond and broad NDC bands. The scans for each sample were taken starting near the substrate interface (denoted 0 μm) to near growth surface (5 μm) with step size of 1 μm . Prior to each measurement, a diamond reference sample was checked with O (Γ) phonon peak at 1331.4 cm^{-1} and FWHM of 6.3 cm^{-1} (visible) and 5.9 cm^{-1} (UV). For all samples, the NDC intensity decreases as we scan from the near interface (initial growth) region to the surface. This confirms that the non-diamond phase in all samples is highest in the initial growth regime and decreases with increasing thickness of the diamond film.

The broad Raman feature at 1460 cm^{-1} for sample S-1 near to the interface shown in Figure 4.7(a) has been attributed to a mixture of sp^3 diamond-like and sp^2 graphitic amorphous carbon [81]. The appearance of the amorphous carbon bands is generally associated with the interface regions between polycrystals in the film. It is, therefore, expected that the intensity of these features to be higher where the diamond crystals are small, such as in the initial growth region, as is observed here. The presence of smaller crystals, and possibly porous morphology, is also seen in the SEM cross sections in Figure 4.4. The intensity of such carbon features decreases as the thickness of the diamond film increases. The broad non-diamond carbon features can also be seen near the interface for diamond film grown on S-2, as shown in Figure 4.7(b) but with lower intensity than for S-1. This trend continues in S-3 with less intense NDC scatter near the interface as well as the growth surface as shown in Figure 4.7(c). The lowest variation of diamond to non-diamond peaks intensity from interface to the growth surface is observed on S-3 compared to other samples.

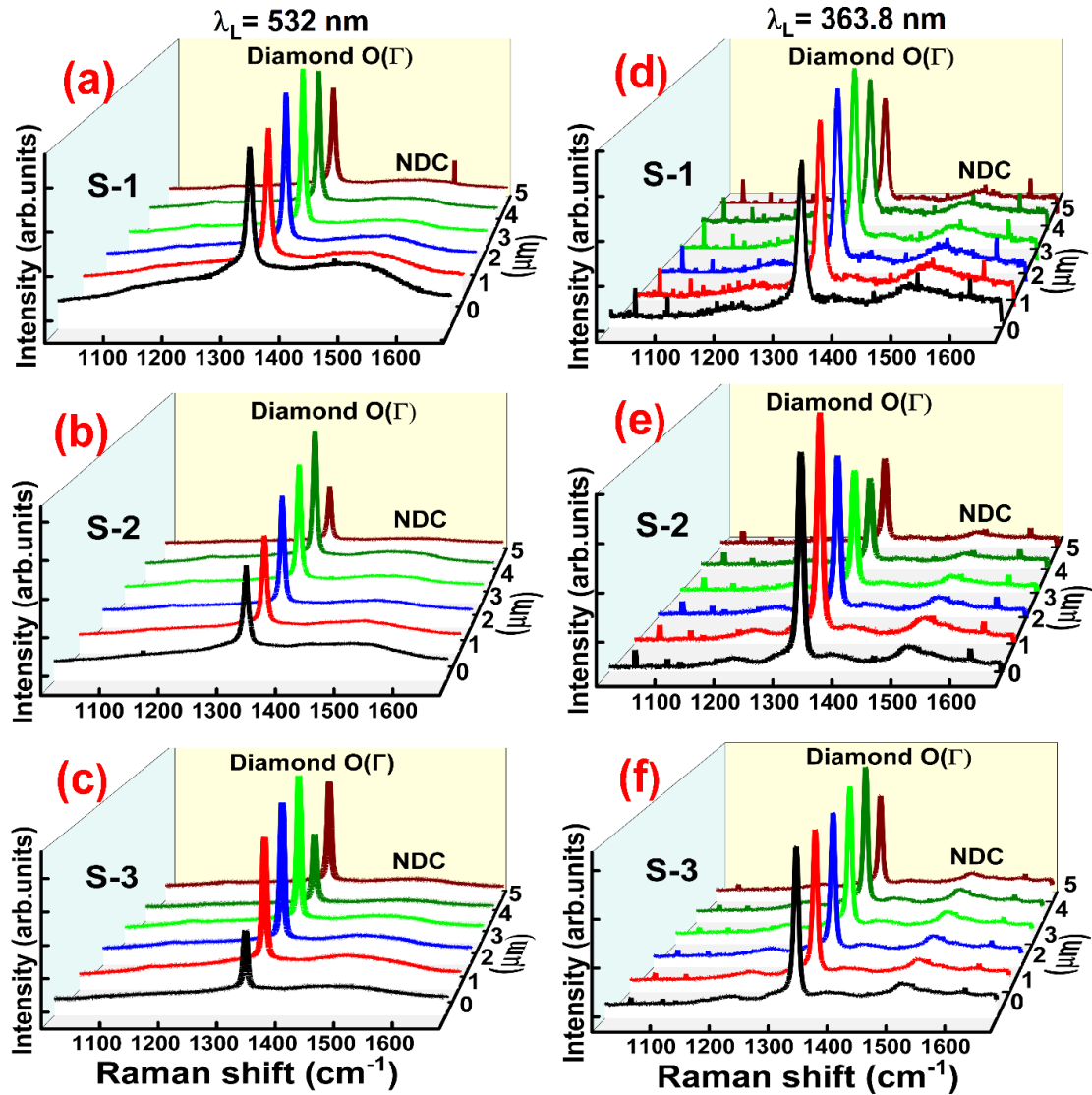


Figure 4.7. Cross-section micro-Raman spectra of diamond from near-interface with Si (0 μm) to near-growth surface (5 μm) for samples S-1, S-2 & S-3, respectively. (a)-(c) 532-nm visible excitation. (d)-(f) 363.8-nm UV excitation.

Similar trends for the variation on NDC intensity is observed for the samples when measuring using UV micro-Raman spectroscopy. The broader NDC features $\sim 1450\text{-}1550\text{ cm}^{-1}$ is seen for sample S-1 near the interface between diamond and silicon

and its intensity decreases with thickness farther from the interface, as seen in Figure 4.7(d). The intensity of such features is found to decrease for S-2 shown in Figure 4.7(e). In contrast to S-1 and S-2, the broad feature NDC is narrower and its intensity lower at the interface and throughout the diamond film for S-3, Figure 4.7(f). The data in Figure 4.8 summarize the diamond phonon line width relative to reference diamond and the diamond volume fraction for all samples from near the interface to the growth surface measured from both visible and UV micro-Raman spectroscopy. When comparing results from the two wavelengths on a given sample, each line scan was obtained from the same region but not from the exact same position.

Figure 4.8(a)-(b) shows the increase in FWHM relative to the reference diamond measured from visible and UV micro-Raman spectroscopy, respectively. Overall agreement is seen in both data sets for a given sample, with differences prospectively coming from the exact location probed during the measurements. Narrower diamond lines, corresponding to improved crystal quality, is seen as the microprobe is positioned farther from the substrate. More important is the improved crystal quality observed with increasing diamond seeding density.

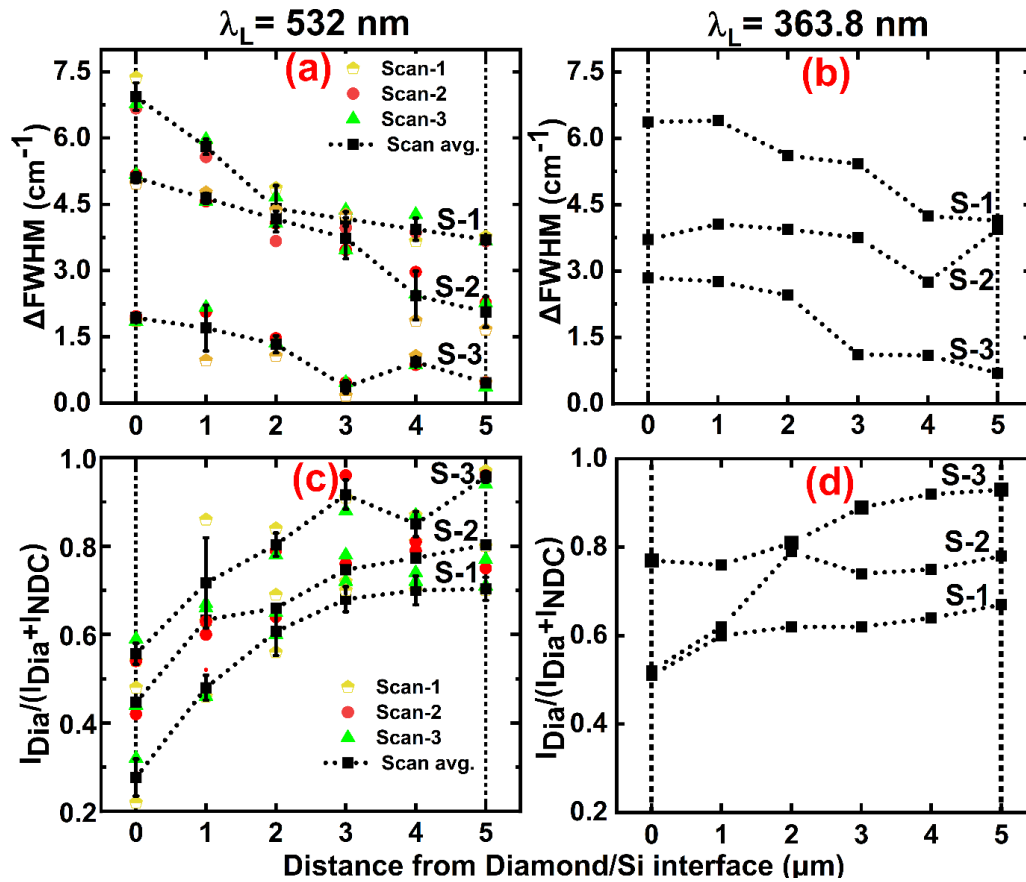


Figure 4.8. Vertical columns are visible (left) and UV (right) micro-Raman results. (a)-(b) Relative FWHM as a function of distance from Si/Diamond interface for all samples measured by visible and UV Raman spectroscopy, respectively. (c)-(d) Relative diamond intensity ratio as a function of distance from Si/Diamond interface for all samples measured by visible and UV Raman spectroscopy, respectively.

The variation in relative diamond volume fraction for all samples from the interface to the growth surface measured from both visible and UV micro-Raman spectroscopy is shown in Figure 4.8(c)-(d), respectively. For all samples, the diamond growth is seen to begin with material that has the lowest diamond phase near the interface and this fraction increases with the diamond thickness toward the growth surface. Furthermore, it is observed that the relative diamond phase volume is enhanced

throughout the layer when seeding at higher density. The highest diamond composition, and lower FWHM, presented in Figure 4.8 from the Raman studies, are attributed to the uniform diamond growth from the early stages following the fast coalescence at high seeding density. Due to high seeds density, the seed layer exposed to hydrogen will undergo transformation with much of the graphitic material (ideally) etched away as growth begins on the diamond seed crystals. The van der Drift growth mechanism will dominate early in the growth period with small crystals and high seeding density to facilitate the formation of high-quality diamond.

The micro-Raman cross-section studies show the seeding density to have a profound impact on diamond film quality. Improved diamond phase purity and crystallinity is observed from the interface to the growth surface with increasing seed density. The improved diamond film quality with highest seed density is attributed to uniformity from the early growth stages, as discussed in the previous paragraph.

XPS study. XPS is used to distinguish the diamond phase of carbon from graphitic and amorphous carbon components, [123,124] with greatest sensitivity at the surface [123]. The chemical states and quantitative information about the various phases of carbon can be found according to the position and intensity of the XPS peaks [125], although it is very difficult to use for diamond films due to various reasons. First, it is difficult to calibrate the energy scale for insulating or semiconducting materials due to charging effects [85,123]. For this reason, the reported value for binding energy for C 1s peak ranges from 283.3 to 285.0 eV [114]. Second, it is challenging to use certain cleaning procedures, such as ion etching or annealing of diamond films, because of possible surface damage, incorporation of etch species (e.g., argon), and irreversible

transformation of sp^3 carbon to sp^2 carbon [114,115]. Third, the measurement is sensitive to contaminants that can adversely affect interpretation of the XPS data [126]. Despite these difficulties in XPS analysis, sample-to-sample comparison is still considered to be informative in the present experiments.

The XPS survey spectrum for diamond sample S-3 at 30 min growth time is shown in Figure 4.9(a). The C 1s spectra can be clearly seen at ~ 285 eV along with evidence of oxygen contamination on the survey scan before Ar ion etching. This contamination is due to exposure of the samples to air. The oxygen peak is reduced after Ar ion etching for 20 s showing this to be an effective clean step for the surface. The high resolution fitted C 1s peak for diamond film grown on sample S-1, S-2, and S-3 for different growth times is shown in Figure 4.9(b-h). The shape of the C1s peak of all samples indicates the presence of several components including diamond (or sp^3 -hybridized carbon) species, graphitic (sp^2 -hybridized C-C bonds) species and, to a lesser extent, hydrogen-carbon bonds. Considering the fitted data, the most intense peak at 284.8 ± 0.2 eV is attributed to the bulk diamond component (sp^3 C-C) with possible contribution from sp^3 CH_1 bonds [114,127]. The less intense peak, shifted by about -0.7 ± 0.2 eV with respect to the diamond peak, may be assigned to graphitic carbon (sp^2 C-C) and, finally, the least intense peak shifted by 1.2 ± 0.3 eV with respect to the sp^2 peak corresponds to C- H_x ($x > 2$) bonds [114]. The FWHM of C1s peaks were found to vary slightly with different samples, probably due to change in morphology and microcrystalline size of diamond films.

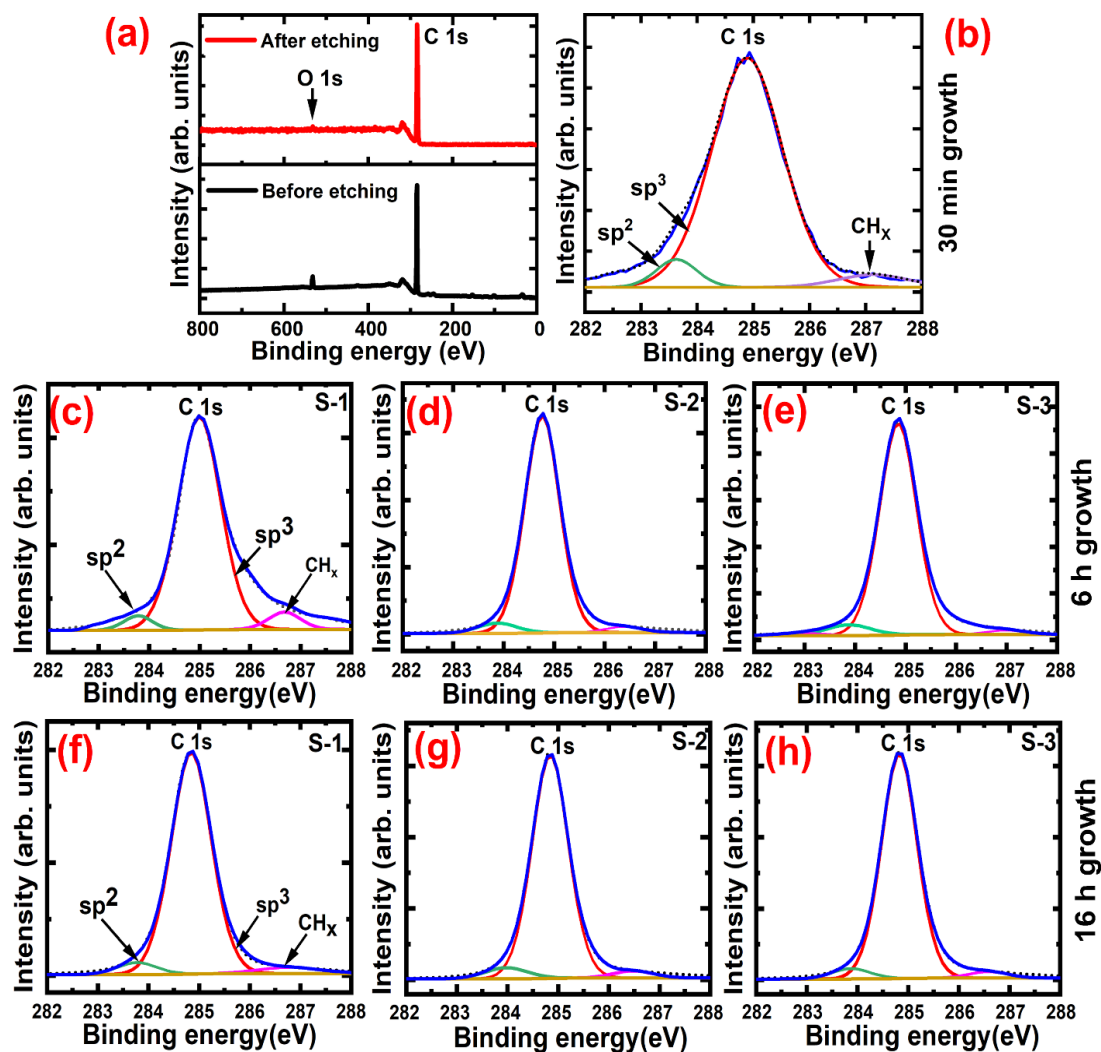


Figure 4.9. XPS results for diamond samples (a) Survey scan before and after Ar ion etching for sample S-3 after 30 min growth (b) C 1s fitted XPS spectra for the diamond grown on S-3 for 30 min. (c)-(e) C 1s fitted spectra for samples S-1, S-2 & S-3, respectively after 6 h growth (f)-(h) C 1s fitted spectra for samples S-1, S-2, and S-3, respectively after 16 h growth.

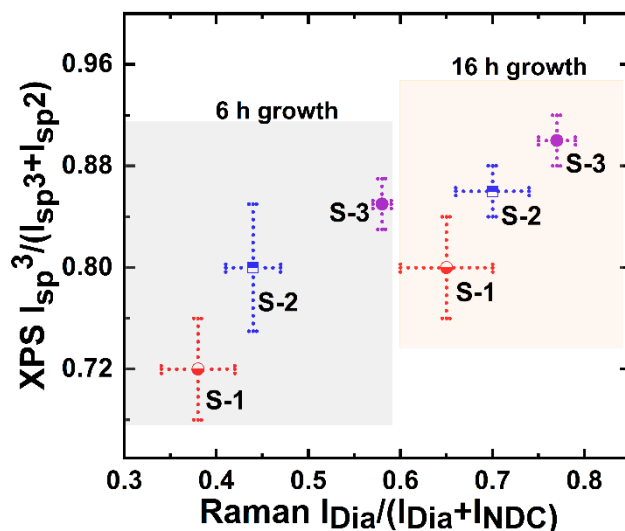


Figure 4.10. The correlation of relative diamond volume fraction from XPS (surface) and UV Raman (volume) data for the diamond samples grow for 6 h and 16 h.

The convolution of the C 1s peaks obtained for diamond films grown on samples S-1, S-2, and S-3 for 6- and 16-h growth facilitates an estimate of the relative volume fraction of sp^3 -bonded C on all samples. This estimate is based on $I_{sp^3}/(I_{sp^3}+I_{sp^2})$, the ratio of integrated intensities of sp^3 -bonded C peak (I_{sp^3}) to the total intensity from sp^3 plus that from the sp^2 -bonded C (I_{sp^2}) [128]. All measurement calculations were done both before and after the Ar ion etching on all samples to confirm that the cleaning process did not substantially change the intensities at the surface. No significant effects due to the etching were found. For both growth series of 6 h and 16 h, the relative volume fraction of sp^3 -C is observed to increase with higher diamond seeding density. This again confirms the improvement of diamond film quality when using high seeding density. The relative volume fraction of diamond obtained from XPS is compared with the $I_{Dia}/(I_{Dia} + I_{NDC})$ from UV Raman spectroscopy discussed earlier with results shown in Figure 4.6. It is not expected that these two measures of diamond fraction to be

numerically the same. In particular, the Raman result depends strongly on scattering efficiencies from the different carbon phases present and is a volume measure, while XPS is surface sensitive. However, it is clear from the results that an increasing trend in sp^3 intensity seen at the diamond surface using XPS is also seen in the Raman data that are sensitive to the overall diamond layer.

Interfacial and material thermal characterization. Steady state thermo-reflectance (SSTR) technique was used to characterize the thermal boundary conductance (TBC) between diamond/Si and thermal conductivity of diamond film. Aluminum thin film ~ 80 nm was used as a transducer layer for the measurement. The measured data was fitted by in house build python program considering three-layer structure, as shown in Figure 4.11(a), with known density, thickness, and specific heat for all three layers.

The thermal conductivity results for all three samples S-1, S-2, and S-3 with different seeding density is shown in Figure 4.11(b). The measured thermal conductivity for samples S-1, S-2, and S-3 are 748.46 ± 35.27 W/m K, 726.93 ± 43.11 W/m K and 734.67 ± 24.70 W/m K, respectively. This is comparable to results expected for polycrystalline diamond of similar thickness [129]. The error value on the thermal conductivity is taken from the standard deviation from ten different measurements, six at same spots and four on different spots on the samples. Based on the data analysis, we found that S-1 has slightly higher thermal conductivity compared to S-2 and S-3. This may be due to higher thickness of diamond film on S-1 compared to S-1 and S-2. Instead of significant difference on thickness and grain size between diamond film on sample S-1 and S-3, the thermal conductivity on S-3 is almost close to S-1. This signifies that the

high seeding density on sample S-3 doesn't have negative impact on the thermal conductivity.

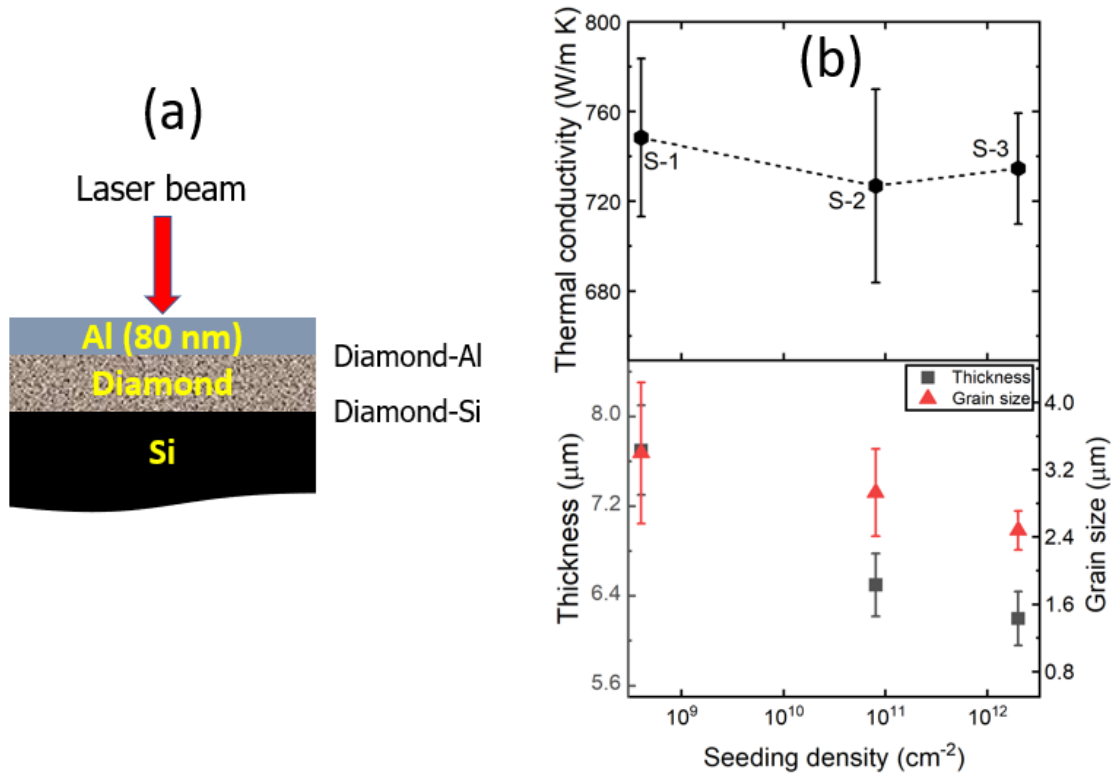


Figure 4.11.(a) Sample layer stack for SSTR measurements (b) Thermal conductivity variation with thickness and grain sizes for sample S-1, S-2, and S-3.

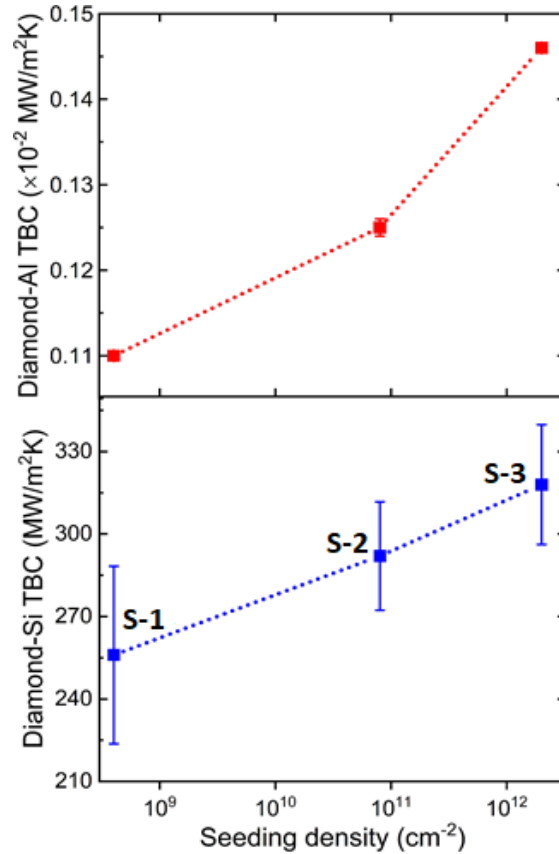


Figure 4.12. Thermal boundary conductance between Diamond-Al and Diamond-Si measured by SSTR.

We found the thermal boundary conductance (TBC) between diamond-Si and diamond -Al increases with increase in seeding density on the samples, as shown in Figure 4.12. The measured diamond-Si TBC for S-1, S-2, and S-3 are 256 ± 32.3 MW/m²K, 292 ± 19.7 MW/m²K and 318 ± 21.8 MW/m²K, respectively. The reported thermal boundary conductance between diamond and Si from published literature is found variation from minimum 66 MW/m²K to maximum 270 MW/m²K for diamond film grown with seeding densities 10^8 - 10^{11} cm⁻² [130,131]. We found improved TBC on our samples compared to previously reported values. The improvement on diamond-Si TBC is due to improvement on diamond film quality near interface with increasing seeding density on the samples. With increasing seeding density, less voids or space

between the diamond grains near interface reduces non-diamond carbon phase, as shown in Figure 4.8. Similarly, the TBC between diamond-Al also increases for the samples with increasing seed density. This is due to enhanced surface quality as well as improved morphology of diamond film grown with increasing seed density, explained earlier in previous section.

Summary

The role of diamond seeding density—spanning the $4 \times 10^8 \text{ cm}^{-2}$ to $2 \times 10^{12} \text{ cm}^{-2}$ range—on the growth, morphology, and quality of diamond films on silicon is studied. The diamond growth is found to vary with seeding density and with total thickness. The diamond films were found to quickly coalesce for the sample with highest seed density. For the lowest seeding density, $\sim 4 \times 10^8 \text{ cm}^{-2}$, the diamond crystals develop three dimensionally via Volmer-Weber growth into large grains, as shown in Figure 4.2(d) and (g), that continue to increase in size with additional HFCVD diamond growth. At the highest seed density, $\sim 2 \times 10^{12} \text{ cm}^{-2}$, coalescence happens within the first 30 minutes of HFCVD growth so that diamond grains are mostly vertical and can be described by the van der Drift growth model. The initial diamond grains are found to be small and more uniform, as shown in Figure 4.2(f) and (i), with a polycrystalline morphology that persists with longer growth time. The slower development of diamond with uniform shape helps to reduce the surface roughness, Figure 4.3(b) and improve diamond film quality. The diamond/Si interface is seen to be porous when isolated diamond grains coalesce for diamond growth with lower seeding density. The relative absence of pores or voids is found with increasing seed density, shown in Figure 4.4(c).

Micro-Raman cross-section images confirm that the diamond phase quality and crystallinity is improved both near the interface and throughout the diamond film thickness for each seeding density, Figure 4.7. Moreover, this improvement in diamond quality is also consistently seen with increasing seed density. From these studies, it is concluded that increasing the diamond seed density to $> 10^{12} \text{ cm}^{-2}$ is important for improving the overall diamond film quality. The uniform diamond growth with high seeding density helps to achieve uniform diamond grains with improved morphology and enhanced diamond film quality. Also, the thermal boundary conductance (TBC) between diamond/Si increases with increase on seeding density.

V. ULTRAHIGH SEEDING DENSITY TO ACHIEVE DIRECT GROWTH OF DIAMOND ON GALLIUM NITRIDE WITHOUT DIELECTRIC ADHESION INTERLAYER

In this chapter, a series of experimental results for diamond growth directly on epitaxial gallium nitride (GaN) with different diamond seeding density is presented. Such coating may be useful to enhance light extraction in GaN LEDs and heat dissipation on GaN based high power and high frequency devices. An electrostatic mixed diamond seeding approach was used to obtain sparse to dense nano-diamond seed density on GaN film prior to diamond deposition. A hot filament CVD reactor utilizing a CH₄/H₂ gas mixture was used to deposit the diamond. It was found that at sparse seed density ~10⁸ cm⁻², the GaN decomposed, which created pinholes in the growing diamond layer or caused it to delaminate. With increasing the seed density >10¹² cm⁻², the quick diamond lateral coverage during the early nucleation step helped to protect the GaN film from decomposition. Physical properties on the sample were characterized using scanning electron microscopy (SEM), atomic force microscopy (AFM), micro-Raman spectroscopy, and X-ray diffraction (XRD). A detailed report on physical properties before and after diamond growth on GaN film with different seed densities is discussed.

Introduction

Gallium nitride (GaN) is a promising material for the high power, high frequency applications [1,2]. In recent years, GaN-based high electron mobility transistors (HEMTs) have attracted attention for use in commercial industries such as transmission base stations and a variety of military systems such as RADAR emitter receiver modules. However, poor thermal management of these devices is preventing them from realizing

their full potential [132]. Significant, localized, Joule heating in the channel of the HEMT results in degradation of device performance and a substantial decrease in their long-term reliability [133,134]. To operate with the power density and lifetime required of a GaN HEMT, enhanced thermal management is necessary [133,135,136]. Attaching the device to a thermal conductivity material that can rapidly transfer the localized heat to an external cooling system is one way to accomplish this. As an example, a microcrystalline CVD diamond with a high thermal conductivity [10]~2000 Wm⁻¹K⁻¹ on the III-Nitride surface would enhance the efficiency and thermal management on a GaN HEMT by dissipating heat from the surface.

Direct diamond deposition on GaN is challenging. GaN, under typical process conditions for CVD diamond growth, does not exhibit good high temperature stability, which poses a major limitation of the CVD diamond growth process. Although GaN has a high melting temperature, atomic hydrogen at high temperature (~800° C) can etch the GaN surface resulting in the formation of NH₃ and liquid Ga [101,137]. Several attempts have been made to deposit diamond on GaN, but they came with mixed results. Oba and Sugino et al. [138] first attempt to deposit diamond films onto hexagonal (0001)-oriented GaN films using microwave plasma CVD. They conducted a carburization process on GaN surface to prevent surface etching. May et al. [127] reported the growth of continuous layers of diamond on GaN using a hot filament CVD technique. They found that there was a competition between the rate of diamond deposition and the rate of GaN decomposition, which determined whether net deposition or etching occurred. When the temperature was higher than 600 °C, the GaN decomposed, evolving gaseous N₂ which created pinholes in the growing diamond layer or caused it to delaminate. Mandal et

al. [102] reported the growth of diamond directly on GaN by an electrostatic diamond seeding approach but there is a lack of extensive studies of the diamond-GaN interface by Raman spectroscopy and microscopy to provide evidence regarding the protection of GaN after diamond deposition.

In this chapter, a mixed-electrostatic seeding approach to obtain sparse to dense nano-diamond seeds on the GaN using a polymer coating followed by sonication in the nano diamond solution is reported. Then, a comparative study for the diamond growth on GaN with low $2.3 \times 10^9 \text{ cm}^{-2}$ and dense $3.1 \times 10^{12} \text{ cm}^{-2}$ seed density is presented. Sequential growth is carried out to allow the study of the diamond films in the early stages (30 min) and after a total growth time of 6 h. This dense seeding approach results in the direct deposition of diamond on GaN and prevents GaN etching via the harsh HFCVD conditions while on the other hand significant GaN etching is found with low seeding density. The repeatability of the experiment is checked by growing different sample with approximately the same seeding densities. Physical properties were characterized using scanning electron microscopy (SEM), atomic force microscopy (AFM), X-ray diffraction and micro-Raman spectroscopy.

Experiment and Results

Seeding, diamond growth, and characterization methods. The $\sim 450 \text{ nm}$ thick GaN thin film samples were deposited on a $\sim 450 \text{ nm}$ graded Al(Ga)N strain-control buffer layer grown onto Si (111) substrate using metal-organic chemical vapour deposition (MOCVD). The GaN layer was (0001)-oriented with a surface RMS roughness of $<1 \text{ nm}$ over $5 \times 5 \mu\text{m}$ regions. For diamond seeding, a cationic poly (diallyl dimethylammonium chloride) or PDDAC polymer with positive zeta-potential $\sim 51.2 \text{ mV}$

and nano-diamond slurries with negative zeta potential ~ -47.0 were used. The polymer assisted dip seeding technique followed by ultrasonication for diamond seeding, explained in Chapter III, was used. To obtain different diamond seed densities, seeding was first optimized on the polymer coated GaN sample with varying sonication time from 5-60 min.

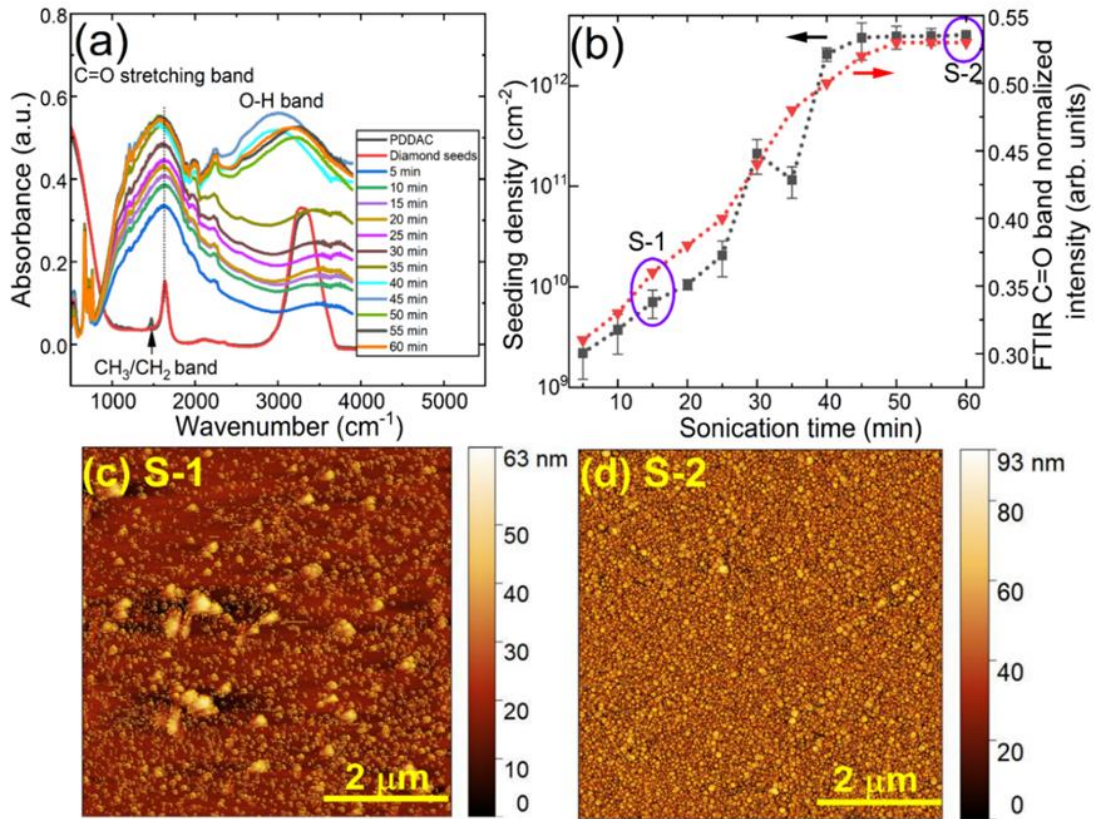


Figure 5.1. Diamond nano-particle signal collected from ATR-FTIR spectra on GaN after nano-diamond solution sonication from 5-60 min.(b) Diamond seed density variation on GaN with different ultrasonication time on nano-diamond slurries and corresponding C=O integrated peak intensity observed from FTIR. (c)-(d) AFM with $(2.3 \pm 0.2) \times 10^9 \text{ cm}^{-2}$ and $(3.1 \pm 2.3) \times 10^{12} \text{ cm}^{-2}$ seed density on sample S-1 and S-2, respectively.

The nano diamond seeding to the PDDAC polymer-coated GaN substrate was monitored by using in-situ ATR-FTIR measurements. The FTIR spectra is shown in Figure 5.1(a). The spectra were recorded using a Bruker Alpha II FTIR Spectrometer equipped with high sensitivity pyroelectric DLaTGS room temperature detector. Spectra were recorded over the 500-4000 cm^{-1} spectral range with a spectral resolution better than 2 cm^{-1} . Prior to sample scans, the FTIR spectrum for diamond seed solution and PDDAC polymer were measured. The sharp peak in the diamond seed spectrum centered at 1650 cm^{-1} (C=O stretching bond) attested to the presence of carboxylic acid group and δ -lactam functional group and the broad strong peak from (2700-3550) cm^{-1} indicated the presence of O-H stretching bonds due to intermolecular forces between the nano diamond seeds and water [139]. Similarly, the small peak centered at 1465 cm^{-1} for PDDAC polymers confirms the presence of C-H bending due to the presence of a methylene group [28].

The FTIR analysis for the seeded GaN sample shows a broad-spectrum peak at (1700-1635) cm^{-1} indicating the C=O stretching band from conjugated acid groups from carboxylic acid present at the diamond surface [129]. The FTIR spectra normalized peak intensity for C=O band is shown in Figure 5.1(b). This shows that the C=O normalized peak intensity increases regularly until 40 min, after which its intensity remains approximately constant. Thus, the maximum constant intensity reached for ATR signal after 40 min represents the uniformly seeded dense nano diamond seeds on the GaN surface. To verify the coverage, the sample was rinsed with water and the peak intensity remained constant. This signifies that the diamond nano seeds were effectively bound to the GaN surface.

The diamond seed density was measured using AFM to identify particles on the surface using the Gwyddion scanning probe microscopy (SPM) analysis software [106] following the approach described in previous chapters for determining diamond seeding densities [96]. Results are summarized in Figure 5.1(b) based on a minimum of three individual $5 \times 5 \mu\text{m}^2$ AFM scans from each sample. The seeding density on the samples were found to increase with increasing sonication time up to 40 min and remains almost constant thereafter, up to 60 min. This is attributed to seed saturation on the sample surface. An almost constant peak intensity for C=O from FTIR spectrum for the seeded samples shown in Figure 5.1(b) after 40 min also confirms the presence of dense diamond seeding on the sample surface. The maximum seeding density measured after 60 min sonication is found to be approximately $3 \times 10^{12} \text{ cm}^{-2}$. In all cases, the measured seed density obtained from AFM scans is less than the maximum $4.6 \times 10^{12} \text{ cm}^{-2}$ predicted with a seed diameter of 5 nm using an idealized close-packing approach [91].

For this study, two samples labeled S-1 and S-2 were seeded with the sonication assisted electrostatic seeding approach. AFM scans for each sample are shown in Figure 5.1(c)-(d). The seeding density measured from AFM images for S-1 and S-2 are found to be $\sim 2 \times 10^9$, and $3 \times 10^{12} \text{ cm}^{-2}$, respectively. For the diamond growth, all samples were simultaneously positioned inside the HFCVD system. Power (6 kW) driven through the array of nine tungsten wires—24 cm long and 0.25 mm diameter—resulted in a 2200 °C filament temperature. The water-cooled rotating substrate holder was positioned 6 mm below the tungsten wire array to produce a substrate temperature of 720–750 °C as measured by IR pyrometer. Source gases were 60 sccm CH₄ (3%), 2000 sccm H₂, and 3 sccm O₂, with the chamber pressure maintained at 2773 Pa (20.8 Torr). The growth

comprised sequential steps in order to determine the time to coalescence and for extensive characterization at total growth times of 30 min and 6 h.

After each growth step, scanning electron microscopy (SEM, FEI Helios 400) was used to characterize in-plane film uniformity and SEM focused ion beam (FIB) milling for cross-sectional views of the samples to assess layer thickness and to examine the diamond/GaN interface. AFM (Bruker Dimension ICON) was used in tapping mode to check the seeding density prior to growth and to evaluate the root-mean square (RMS) roughness and grain size following diamond growth. Diamond phase purity and quality were characterized by using both UV and Visible micro-Raman spectroscopy. UV micro-Raman spectroscopy with excitation wavelength 350 nm with shallow penetration depth was used to characterize the GaN material quality near to diamond and GaN interface. The laser excitation was focused into a point with approximately 2- μm diameter using a x100 objective lens with NA 0.40 and acquisition time of 60 s to collect the spectra. Visible micro-Raman mapping (excitation wavelength 532 nm) with 10 μm \times 10 μm were used to analyze the samples at three different positions before and after the diamond growth.

Morphology and interface analysis. Figure 5.2 shows the representative SEM morphology and cross-section images of S-1 and S-2 grown at different times. Figure 5.2(a)-(b) represent the SEM images for the diamond grown on sample S-1 after 30 min and 6 h, respectively. Well separated diamond crystallites are seen after 30 min growth. Well-developed diamond nuclei with stable equilibrium shapes with a mean lateral size of $\sim 1.5 \mu\text{m}$ can be seen on S-1, Figure 5.2(b), with additional 6 h growth. The lower seeds density diamond on sample S-1 causes the diamond crystals to grow three

dimensionally in a Volmer-Weber growth mode [117]. Due to the sparse seed coverage on sample S-1, hydrogen can easily achieve contact with the GaN surface during HFCVD diamond growth conditions and react and decompose into volatile by-products such as GaH and NH₃. The cross-section SEM image on Figure 5.2(c) shows significant etching and decomposition of GaN near the diamond-GaN interface.

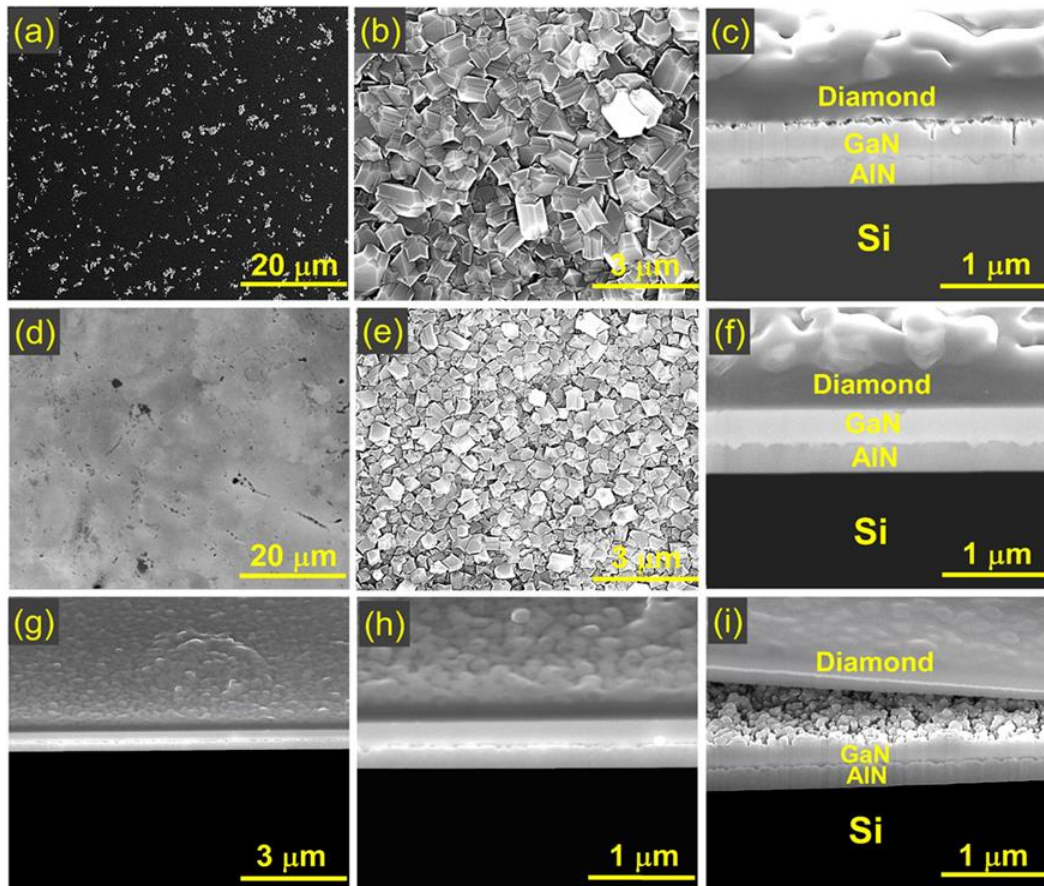


Figure 5.2. SEM images of diamond film grown on sample S-1 (a) after 30 min (b) after 6 h, (c) Focused ion beam (FIB) cross-section SEM image for sample S-1 after 6 h growth. (d)-(e) are SEM images for diamond grown on sample S-2 after 30 min and 6 h respectively, (f) FIB cross-section SEM image for diamond grown on sample S-2 after 6h and (g)-(i) cross-section SEM images for diamond grown on another sample with identical seeding as S-2 from center to edge, respectively.

Figure 5.2(d)-(e) show the corresponding SEM images for the diamond film grown on sample S-2 after 30 min and 6 h, respectively. Full coalescence of the diamond crystals at $\sim 0.06 \mu\text{m}$ in the early growth stage is seen in Figure 5.2(d) with high seeding density. The film is uniform and with higher density diamond crystals after 6 h CVD growth, in Figure 5.2(e), compared to sample S-1, in Figure 5.2(b). This is due to the dense diamond seeding and a process dominated by an early van der Drift growth mode [111,117]. The cross-section SEM image for the diamond film on S-2 after 6 h is shown in Figure 5.2(f). A smooth diamond-GaN interface with minimal to no GaN etching or decomposition can be seen. No delamination of the diamond film from the GaN is observed. Due to the high diamond seed density of sample S-2, quick lateral diamond coverage occurs early in the CVD growth and helps to protect the GaN from etching from the harsh HFCVD environment.

The integration of diamond with high seeding density on GaN was checked for the repeatability of the process on different set of samples by growing diamond with almost same seeding density as S-2. The SEM cross-section images for the sample at three different positions i.e., 15 mm, 30 mm, and 45mm from center of 100 mm diameter wafer, shown in Figure 5.2(g)-(i). A smooth diamond/GaN interface can be observed. In contrast, diamond delamination and etching of the GaN layer was found near the edge of the wafer as shown in Figure 5.2(i). We attribute such delamination is associated with slight variation on the diamond seeding density near at the edge of the sample. Due to non-uniform seeding near at the sample edge, few nanometers of GaN etched away during early diamond growth making the pinholes on GaN and diamond get delaminated during the cooling cycle. Other possible reason for such delamination is the weak van der

Waal force between the diamond and GaN rather than strong covalent bond. GaN has a room temperature thermal expansion coefficient ($5.59 \times 10^{-6} \text{ K}^{-1}$) that is 28% larger than that of diamond ($4.38 \times 10^{-6} \text{ K}^{-1}$) [138]. When cooled, GaN will return to its room temperature volume, while the diamond with which it is bonded will contract far less. A compressive stress is created in the diamond layer, resulting in either bowing of the sample or delamination of the diamond layer [137].

High resolution x-ray diffraction analysis. HRXRD was employed to determine the degree in which the underlying GaN layer has been protected after 6 h of diamond growth. Comparative HRXRD in Figure 5.3(a) shows the q - $2q$ patterns before and after diamond growth. The III-nitride layers, AlN and GaN, with second order (0002) diffraction peaks are present in all samples. (AlN is employed as a nucleation layer between the Si (111) substrate and GaN layer.) The diamond (111) diffraction peak at 43.9° is observed with S-1 and S-2, after the diamond growth. The normalized peak intensity of GaN (0002) with respect to AlN (0002) were compared for all samples before and after diamond growth. The integrated normalized peak intensities, $I_{\text{GaN}} / (I_{\text{GaN}} + I_{\text{AlN}})$, were (0.82 ± 0.03) , (0.48 ± 0.24) and (0.85 ± 0.04) for the samples before diamond growth, S-1, and S-2, respectively. The error value on the integrated peak intensity is calculated based on the standard deviation taken for the samples at three different measurement positions. Based on the integrated peak intensity, the GaN layer has been significantly etched for sample S-1, with low seed density, while it has been protected by the diamond film grown with high seed density on sample S-2.

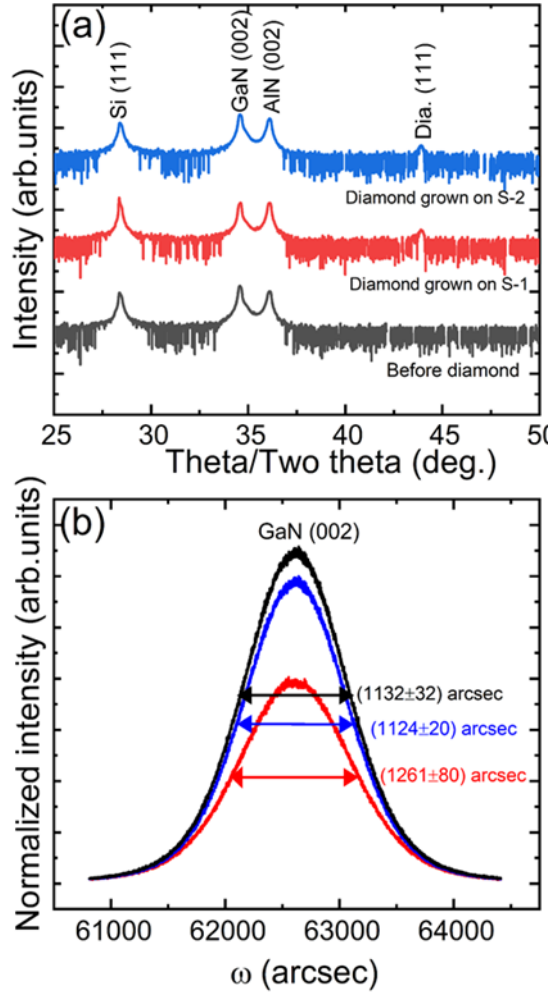


Figure 5.3. (a) HRXRD theta/two theta spectrum for the samples before and after diamond growth and (b) GaN (002) rocking curve for the samples before and after diamond growth.

GaN crystal quality before and after diamond growth were analyzed using rocking curve analysis. Figure 5.3(b) shows the XRD ω scans for the (0002) GaN plane for the three samples. The FWHM was 1132 ± 32 , 1261 ± 80 , and 1124 ± 20 arc sec for before diamond, S-1, and S-2, respectively. The error values represent the standard deviation taken for three different scans at different locations across the samples. The GaN (0002) FWHM for sample S-1 has increased compared to before diamond growth. This indicates

the GaN crystal quality has been negatively impacted due to etching and/or decomposition during the HFCVD diamond growth process. The GaN (0002) FWHM for S-2 is basically unchanged compared to before diamond growth. This indicates that the GaN layer is protected from etching or decomposition during direct diamond integration with the high seed density of S-2.

Micro-Raman results. Figure 5.4 shows UV (a) and Visible (b) micro-Raman spectra for the GaN layer prior and following the diamond growth. Due to the shallow penetration depth (≤ 100 nm) into the GaN [140], the UV spectra exhibits scattering from the GaN layer only. (There is no distinct UV spectral peak for GaN E_2^2 and $A_1(\text{LO})$ for the bare GaN sample, prior to diamond growth, due to high background associated with GaN photoluminescence (PL).) Post diamond deposition, the weak characteristic $O(\Gamma)$ symmetric phonon[89] at ~ 1332 cm^{-1} , weak GaN E_2^2 and $A_1(\text{LO})$ symmetric phonon, along with a second-order quasi- $E_1(\text{LO})$ band at ~ 1475 cm^{-1} is observed [132]. The diamond peak appears relatively weak due to strong resonance with the GaN. The visible micro-Raman spectra is presented in Figure 5.4(b). GaN E_2^2 and $A_1(\text{LO})$ phonon, the AlN E_2^2 band, and, post diamond deposition, the associated $O(\Gamma)$ line are distinguishable.

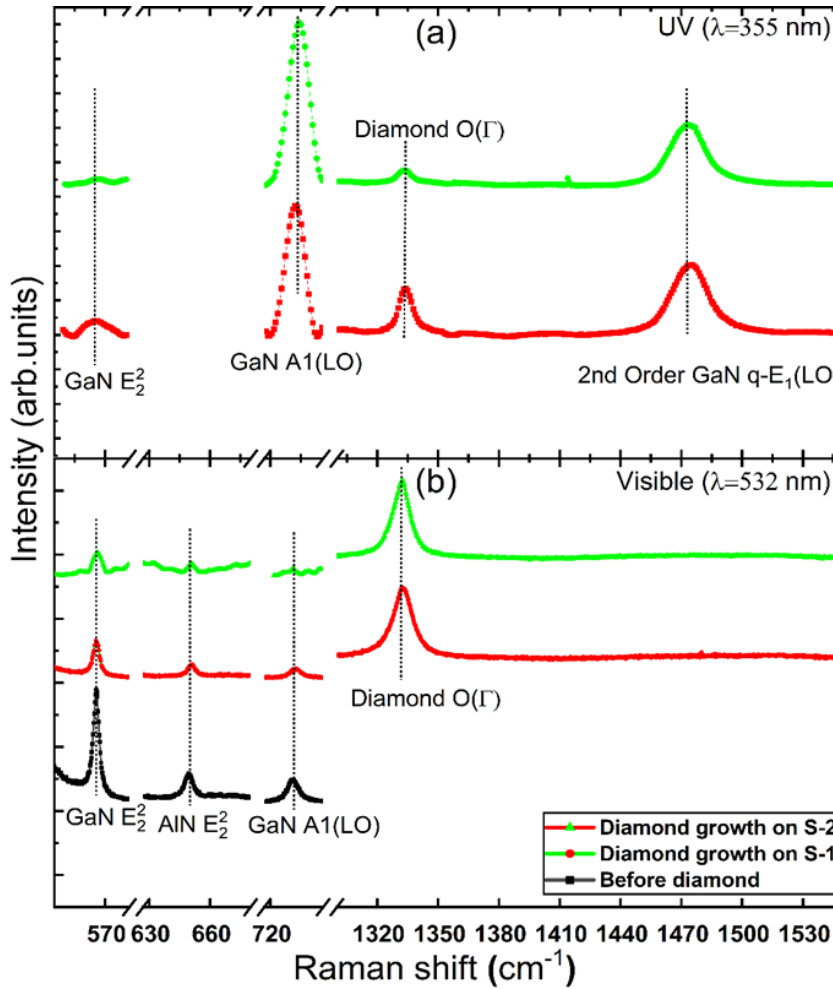


Figure 5.4. Ultraviolet (a) and visible (b) Raman spectra taken before and after diamond growth on sample S-1 and S-2. Detailed spectra of E_2^2 (GaN, AlN) and $A_1(\text{LO})$ (GaN) showing phonon shift.

The E_2^2 peak position in GaN and AlN layers are sensitive to stress. The peak position and line width were determined by fitting the data using Lorentzian functions. Results are summarized in Table 4. For the E_2^2 peak position and shift relative to the bulk value for GaN and AlN, the relative shift in each case corresponding to the stress is determined. Stress on the film can be estimated from the Raman shift using published

stress factors, which vary between reports for GaN and AlN. A Raman stress factor of $3.4 \pm 0.1 \text{ cm}^{-1}/\text{GPa}$ [141,142] is used to determine the GaN E_2 stress prior to and after the diamond growth. From visible Raman, a stress value of $0.97 \pm 0.08 \text{ GPa}$ prior to diamond growth was obtained. Following diamond growth, stress values of $0.76 \pm 0.04 \text{ GPa}$ and $1.12 \pm 0.06 \text{ GPa}$ for sample S-1 and S-2, respectively, were obtained. The stress value for sample S-1 decreases following diamond growth, which represents relaxed GaN after diamond deposition due to etching and decomposition of the GaN layer. Increased biaxial stress of the GaN layer following diamond growth on sample S-2 represents a well-protected GaN layer, without etching. Both results are consistent with the HRXRD data discussed in the previous section.

Table 4. Peak Positions from Micro-Raman Spectroscopy before and after Diamond Growth.

Visible Raman Spectroscopy Results						
Parameters	Before diamond growth		After diamond growth			
			S-1		S-2	
	Peak position (cm ⁻¹)	Relative shift (cm ⁻¹)	Peak position (cm ⁻¹)	Relative shift (cm ⁻¹)	Peak position (cm ⁻¹)	Relative shift (cm ⁻¹)
GaN E ₂ ² (FWHM)	564.2±0.1 1 (3.5±0.2)	-4.1±0.1	565.1±0.1 (7.8±0.2)	-3.2±0.2	563.8±0.1 (3.6±0.2)	-4.5±0.2
AlN E ₂ ² (FWHM)	650.6±0.1 1 (4.7±0.2)	-5.9±0.2	650.7±0.1 (4.9±0.3)	-6.0±0.1	650.5±0.1 (4.4±0.3)	-6.2±0.1
GaN A ₁ (LO) (FWHM)	730.9±0.1 1 (6.2±0.3)	-3.4±0.1	730.7±0.1 (6.2±0.2)	-2.0±0.1	731.1±0.1 (6.3±0.2)	-3.2±0.1
Diamond O(Γ)			1332.6±0.1	0.6±0.2	1333.1±0.1	1.2±0.2
The measured reference values for GaN phonon energies are 568.3±0.1 cm ⁻¹ for E ₂ ² and 734.3± 0.1 cm ⁻¹ for A ₁ (LO). For the AlN reference, the measured value is 656.7 ± 0.1 cm ⁻¹ for E ₂ ² . Measured diamond O (Γ) peak reference value is 1331.9 cm ⁻¹ .						
UV Raman Spectroscopy Results						
			Peak position (cm ⁻¹)	Relative shift (cm ⁻¹)	Peak position (cm ⁻¹)	Relative shift (cm ⁻¹)
GaN E ₂ ² (FWHM)			565.9±0.1 (6.5±0.4)	-3.3±0.2	565.6±0.1 (6.5±0.4)	-3.6±0.1
GaN A ₁ (LO) (FWHM)			732.3±0.1 (11.2±0.3)	-1.0±0.1	731.2±0.1 (9.8±0.3)	-2.1±0.1
Second order quasi-E1 (LO)			1475.1±0.1 (21.5±0.6)		1475.1±0.1 (20.2±0.3)	
Diamond O(Γ)			1332.4±0.1	0.2±0.1	1333.4±0.1	1.2±0.1
The measured reference values for GaN phonon energies are 569.2±0.1 cm ⁻¹ for E ₂ ² and 733.3± 0.1 cm ⁻¹ for A ₁ (LO). For the AlN reference, the measured value is 656.7 ± 0.1 cm ⁻¹ for E ₂ ² . Measured diamond O (Γ) peak reference value is 1332.2 cm ⁻¹ .						

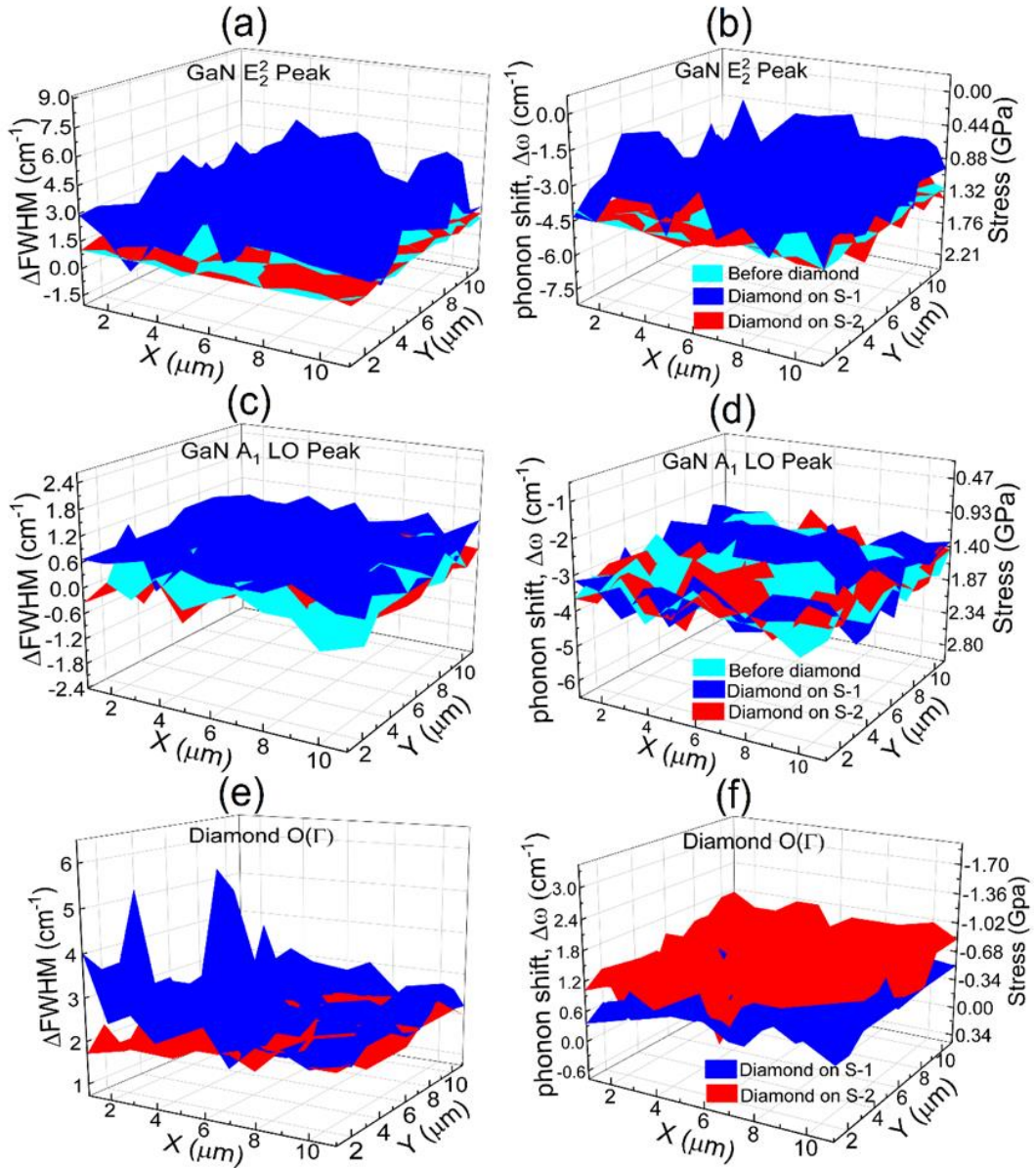


Figure 5.5. Visible Raman spectroscopy map of relative FWHM and phonon shift (stress) for (a)-(b) GaN E_2^2 peak, (c)-(d) GaN A_1 (LO) peak and (e)-(f) Diamond $O(\Gamma)$, for sample before diamond growth and after diamond growth with low seed density (S-1) and high seed density (S-2).

Visible Raman mapping of the samples was performed to ascertain the film quality and stress in GaN and diamond for sample S-1, with low seeding density, and S-2, with high seeding density. The results are summarized in Figure 5.5(a)-(b) which shows the visible Raman mapping of relative FWHM and phonon shift for the GaN E^2_2 phonon energy before diamond growth and after both S-1 and S-2. The relative FWHM for GaN E^2_2 phonon is found to increase after diamond growth for S-1 compared to the GaN sample prior to diamond growth. This indicates that the GaN quality has been degraded after diamond deposition due to the low seed density. The relative FWHM for GaN E^2_2 for sample S-2 after diamond deposition essentially overlaps with the reference sample. This indicates the GaN layer crystal quality remains approximately constant after diamond growth on S-2, due to the high seeding density.

The stress of the GaN layer prior and after diamond growth were also calculated from Raman mapping. Peak position, ω , is determined by fitting a Lorentzian function with background subtraction. The shift from the unstrained phonon position, $\omega - \omega_o$, is used to determine the biaxial stress values,

$$\sigma_{xx} = (\omega - \omega_o) / k_R \quad (17)$$

Where k_R is the Raman stress factor. For E^2_2 phonon, $k_R^{E^2_2} = -3.4 \pm 0.3 \text{ cm}^{-1} / \text{GPa}$ [141,142] is used, while $\omega_o = 568.3 \pm 0.1 \text{ cm}^{-1}$ is measured from a reference relaxed GaN film.

Figure 5.5 (b) shows the map of the E^2_2 phonon shift and corresponding stress calculated using equation (17). A red shift is obtained from ω_o for all samples before and after diamond growth relative to the reference value, $568.3 \pm 0.1 \text{ cm}^{-1}$. The GaN tensile stress before diamond growth ranges from 1.18 GPa to 1.35 GPa with an average value of 1.24

GPa. After diamond growth S-1, with low seed density, exhibits a stress change from 0.35 to 1.40 GPa, with an average 0.52 GPa. This indicates that the GaN surface is substantially relaxed due to significant etching after diamond growth. By comparison, the GaN stress remains consistent, 1.18 GPa to 1.58 GPa, with average 1.43 GPa for sample S-2, with high seed density. The average tensile stress of sample S-2 increases after diamond growth compared to prior to diamond growth signifying that the GaN film is stressed with diamond growth without etching (or decomposition). The GaN A_1 (LO) phonon peak was also mapped for relative FWHM and peak shift from the visible Raman spectroscopy using the Raman-stress factor for this phonon, $k_R^{A_1} = -2.4 \pm 0.28 \text{ cm}^{-1}/\text{GPa}$ [140], and the stress-free reference frequency $\omega_0 = 734.3 \text{ cm}^{-1}$. The results are shown in Figure 5.5(c)-(d). We observed similar characteristics for FWHM and relative peak shift for all samples before and after diamond growth as was observed for GaN E^2_2 phonon.

Finally, the diamond FWHM and peak position with relative stress were mapped from the visible Raman spectroscopy. The results are shown in Figure 5.5(e)-(f). The relative FWHM for the diamond $O(\Gamma)$ peak for sample S-2 is more uniform and narrower compared to S-1, relative to the reference value of 5.9 cm^{-1} . This confirms that the diamond film quality is improved for the diamond film grown with high seeding density in comparison to lower seeding density. Similarly, the relative diamond volume fraction measured on S-1 and S-2 are 0.59 ± 0.08 and 0.73 ± 0.06 , respectively. The improved crystallinity and diamond phase on sample S-2 is due to improved nucleation with high seed density.

The stress in the diamond film for both samples is determined from the phonon shift maps shown in Figure 5.5(f). The overall biaxial stress of the diamond film for respective peak positions was calculated by using equation (17) where $k_R^{dia} = -1.76 \text{ cm}^{-1}/\text{GPa}$ and ω_0 at 1331.9 cm^{-1} were used. The diamond film stress of S-1 varied from -0.36 to -0.78 GPa with an average biaxial stress $\sigma_{bs} = -0.40 \text{ GPa} \pm 0.28 \text{ GPa}$. Similarly, the stress of the diamond film for S-2 varied from -0.34 to -1.32 GPa with an average compressive stress $\sigma_{bs} = -0.95 \text{ GPa} \pm 0.26 \text{ GPa}$. The compressive stress developed on diamond film on S-1 is lower than S-2. This indicates that etching the GaN layer during diamond growth on S-1 relaxes the diamond film. The compressive biaxial stress is generated on sample S-2 due to dense seeding inhibiting etching and decomposition of the underlying GaN layer.

Summary

The role of diamond seeding density on direct diamond growth on GaN without a dielectric adhesion layer was studied. It was observed that the diamond nuclei coverage with low seeding density did not coalesce during the early stage of diamond growth resulting in etching and decomposition of the GaN layer. In contrast, quick diamond coalescence during the early growth stage results in a GaN layer protected from etching by the harsh HFCVD diamond growth conditions. XRD and micro-Raman studies confirm that the GaN material quality has been degraded for the sample with low seed density and remains unchanged compared to the reference GaN layer for the sample with high seeding density. Furthermore, the diamond film quality is improved with high seed density as indicated by the narrower FWHM compared to the low seed density sample. The experiment confirms, for the first time, that diamond can be grown directly on GaN

with no dielectric adhesion layers by utilizing a high diamond seeding density process.

VI. STUDY ON THE HETEROGENEOUS INTEGRATION OF DIAMOND ON ULTRA-WIDEBAND GAP SEMICONDUCTOR

In this chapter, diamond integration with ultra-wideband gap semiconductors AlN and high Al contents AlGaN is presented.

Integration of Diamond on AlN with Different Seeding Density

AlN and high Al content AlGaN is currently used in various applications ranging from deep ultraviolet light emitting diode to high power electronic devices [162]. AlN and AlGaN active layers of these devices is primarily grown on foreign substrates, such as silicon, sapphire, and silicon carbide [163]. The density of threading dislocations in nitride films grown on a foreign substrate is high, typically $>10^8 \text{ cm}^{-2}$, even when special growth techniques are employed and is a major obstacle to improve device performance [163]. Typically, an AlN nucleation layer is utilized to grow high Al content AlGaN in order to achieve lower defect densities as well as non-radiative recombination centers [164]. In addition, AlGaN alloys grown on Si substrates with an AlN nucleation layer need to undergo strain relaxation to ensure low defect density and to assist in devices' design [1].

Growth of $\text{Al}_x\text{Ga}_{1-x}\text{N}$ across the full composition range, x , has long been established using several methods including molecular beam epitaxy (MBE), hydride vapor phase epitaxy (HVPE), and metal organic chemical vapor deposition (MOCVD) [165–168]. $\text{Al}_x\text{Ga}_{1-x}\text{N}$ transition layers are often used in the fabrication of GaN high electron mobility transistors on silicon for fabrication of subsequent device quality $\text{Al}_x\text{Ga}_{1-x}\text{N}$ confinement layers [131]. The current crowding inherent in the 2DEG of these HEMT structures produces aggressive self-heating. It was shown that the effect produces

a temperature rise in the device of $\Delta T \sim 360^\circ\text{C}$, at 7.8 W/mm drive power (per gate length) [9]. To fully realize the promise of high power possible in GaN, i.e., when not limited by self-heating, the power electronics community has been drawn to research for improving thermal management. An attractive solution to thermal management is integration of the III-Nitride semiconductors with diamond [169].

Diamond is a superior choice as a heat spreading materials compared with standard GaN based substrates such as SiC, Si and Al_2O_3 [53]. Although the thermal conductivity values for bulk GaN ($160 \text{ W m}^{-1} \text{ K}^{-1}$) and SiC ($\sim 420\text{-}490 \text{ W m}^{-1} \text{ K}^{-1}$) are reasonably high [2,143], the nucleation layer and the resulting microstructure near to the interface can cause a significant barrier for heat to travel from the GaN device to the SiC substrate [134,144]. In addition to any film adhesion layer resistance and intrinsic thermal boundary resistance, additional factors, such as poor material quality near the interface, could impact thermal transport across the layers [134,135]. The heat must be removed through back or side of the substrate wafer to an external cooling system.

Direct diamond growth on GaN based devices is challenging due to adhesion and etching problems on harsh HFCVD conditions. AlN is one possible material to use as the barrier layer [145]. However, some issue related to adhesion and etching of AlN layer during diamond growth has been reported [146,147]. Pobedinskas et al. [147] had studied the effects of hydrogen and methane plasmas on sputtered AlN during micro-wave plasma chemical vapor deposition of diamond. They found that the films can be etched when exposed to plasma for long periods of time. Once the diamond film is coalesced, the AlN layer should be protected by the diamond layer. Mandal et al. [148] showed that the thick diamond $\sim 200 \mu\text{m}$ can be grown on AlN with normal nano-diamond seeding

technique with low thermal boundary resistance $\sim 15 \text{ m}^2\text{K/GW}$. They have shown that AlN is readily attached with diamond and readily form a carbide which helps diamond adhesion plus the added benefit is that the AlN layer acts as an etch stop and an adhesion layer for the diamond growth.

In this chapter, a comparative study of the nucleation, growth rate, grain size, crystal quality and thermal properties of diamond films grown on AlN at seed densities 1×10^8 and $2 \times 10^{12} \text{ cm}^{-2}$ are reported. Building off the progress discussed in the previous chapters, the innovative polymer assisted electrostatic seeding approach was used to control diamond seeding density on AlN from $\sim 10^8 \text{ cm}^{-2}$ to $\sim 10^{12} \text{ cm}^{-2}$. Thick diamond, $\sim 10 \text{ }\mu\text{m}$, on AlN with different diamond seed density by hot filament chemical vapor deposition (HFCVD) without any adhesion or protective layer was investigated. Characterization methods include scanning electron microscopy (SEM), atomic force microscopy (AFM), and micro-Raman spectroscopy. The growth, morphology, and quality of diamond film across the entirety of the film thickness from the substrate interface region to the diamond surface was evaluated.

Diamond seeding, growth, and characterization methods. The sample investigated had a $\sim 400 \text{ nm}$ thick AlN layer deposited on a single crystalline Si (111) substrate using Texas State University's custom-built MOCVD reactor. Trimethylaluminum (TMAI) was used as the Al source and ammonia (NH_3) was used as the nitrogen source in hydrogen carrier gas, following the standard growth procedure [132,149]. The AlN layer was (0001) oriented with a surface RMS roughness of $\sim 1.5 \text{ nm}$ over $5 \times 5 \text{ }\mu\text{m}$ scans, shown in Figure 6.1(a). The substrate was cut into four equal quadrants and pre-seeded with diamond using the polymer assisted electrostatic seeding technique. The seeding

technique involves self-assembly of diamond nanoparticles on the polymer coated substrate by creating electrostatic van der Waal force between a cationic polymer and the diamond nanoparticles. The detail of the seeding technique is discussed in Chapter III.

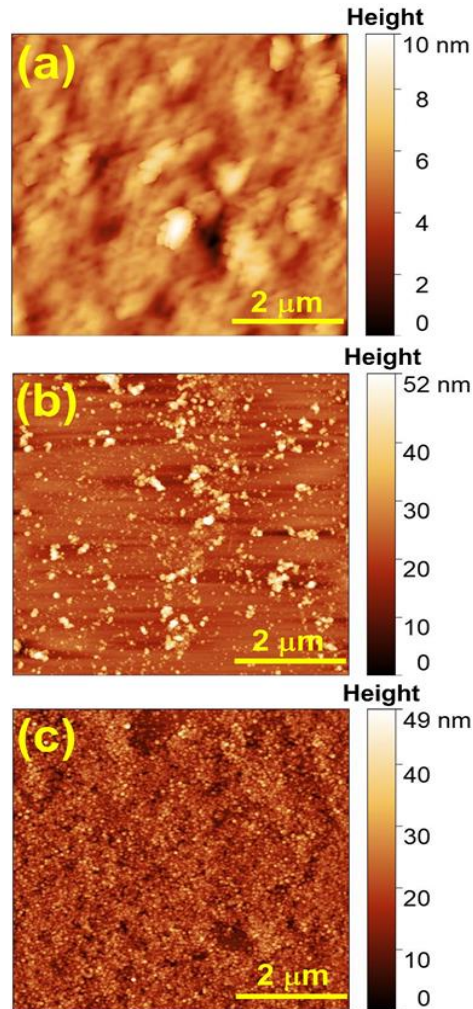


Figure 6.1. (a) $5 \times 5 \mu\text{m}^2$ AFM images before seeding and (b)-(c) after seeding with low seed density $1.1 \times 10^8 \text{ cm}^{-2}$ (S-1) and dense seeding density $2 \times 10^{12} \text{ cm}^{-2}$ (S-2), respectively.

Two samples (S-1 and S-2) were seeded to obtain two different seeding densities. Both samples were rinsed with acetone, methanol, and isopropanol prior to diamond seeding. ~250 nm thick Poly (diallyl dimethylammonium chloride) PDDAC polymer

with positive zeta-potential ~ 51 mV was coated on both samples. The samples were then ultrasonicated in the carboxylate nano-diamond slurry with negative zeta-potential ~ 47 mV. S-1 and S-2 were sonicated for 5 and 60 min, respectively, to achieve the different seeding densities. Following the seeding, both samples were rinsed with water and lightly dried with N_2 gas to remove poorly attached seeds from the substrate surface.

The diamond seed density was measured using AFM images and identifying the diamond particles on the surface using the Gwyddion scanning probe microscopy (SPM) analysis software [106] following the previously described approach for determining diamond seeding densities [24]. The results are summarized in Figure 6.1(b)-(c). The AFM images clearly show diamond seed coverage is substantially lower on S-1 compared with S-2, with an average seed density of $\sim 1 \times 10^8$, and 2×10^{12} cm^{-2} , respectively. Furthermore, S-2 seeding is more uniformly distributed with only a few small clusters, as shown Figure 6.1(c). The measured seed density obtained from AFM is less than the maximum 4.6×10^{12} cm^{-2} predicted with a seed diameter of 5 nm using an idealized close-packing approach [91].

For diamond growth, the samples were simultaneously positioned inside the HFCVD system. Power (6 kW) driven through the array of nine tungsten wires—24 cm long and 0.25 mm diameter—resulted in a 2200 °C filament temperature. The water-cooled rotating substrate holder was positioned 6 mm from the tungsten wire array to produce a substrate temperature of 720–750 °C as measured by IR pyrometer. Source gases were 60 sccm CH_4 (3%), 2000 sccm H_2 , and 3 sccm O_2 , with chamber pressure maintained at 2773 Pa (20.8 Torr). The total growth time was 20 h.

After diamond growth, the samples were characterized by SEM (FEI Helios 400) in-plane and cross-section to assess the film uniformity, layer thickness, and to examine the diamond/Si interface from cleaved samples. AFM (Bruker Dimension ICON) was used in tapping mode to evaluate the root-mean square (RMS) roughness and grain size of the deposited diamond film.

Diamond phase purity and quality across the diamond film was ascertained by micro-Raman measurements with ultraviolet (UV) excitation wavelength 363.8 nm. At this excitation wavelength, the diamond fluorescence is lower than when measuring in the standard visible-wavelength range [80,113,140]. The laser excitation was focused into a line approximately 10- μm long and 2- μm wide using a 100 \times objective (NA 0.40) and acquisition time of 60 s to collect the spectra. Visible micro-Raman spectra (excitation wavelength 532 nm) were used to measure the samples along cross-section planes using a Horiba (LabRAM) system. The nominal spot diameter was $\sim 2 \mu\text{m}$ utilizing a $\times 100$ objective lens with NA 0.90. For all micro-Raman cross-section measurements, a coupon $\sim 10 \text{ mm} \times 3 \text{ mm}$ was vertically affixed on a translational stage illuminating the freshly cleaved edge with the excitation. The sample position was stepped every 1 μm along the growth direction to obtain line images. Visible micro-Raman $10 \times 10 \mu\text{m}^2$ mapping were performed on the sample before and after the diamond growth. In all cases, spectra were collected to capture the silicon and diamond O(Γ)-symmetry phonon lines and the broad non-diamond carbon (NDC) bands in the 1450–1600 cm^{-1} range. The quantitative information was obtained by fitting the diamond Raman band using Lorentzian line shape. Intensities from the disordered carbon were obtained by integrating from 1000 to 1700 cm^{-1} with background subtracted and eliminating the diamond phonon intensity

using the fit results. Finally, diamond thermal conductivity and thermal boundary resistance ($TBR_{\text{eff.}}$) between diamond/AlN was measured using steady state transient thermo-reflectance measurements.

Diamond thickness, morphology, and grain size. Presented in Figure 6.2 are representative SEM analysis results for diamond film with different seed density after 20 h growth. Figure 6.2(a)-(b) represent the morphology of the diamond films with low (S-1) and high (S-2) seeding density, respectively. For both samples, the diamond crystals have stable equilibrium shapes such as rhombic dodecahedron, and truncated octahedron [150]. The diamond structures for sample S-1 are relatively larger and non-uniform in shape, as shown in Figure 6.2(a). For low seed density sample, S-1, the Volmer-Weber growth mechanism during the early stages of diamond growth permit the diamond crystals to grow three dimensionally into larger grains [117,151]. In contrast to sample S-1, the diamond crystals of sample S-2 are more uniform, smaller and compact. This is attributed to the dense seeding, and corresponding to a situation dominated by early van der Drift growth mode [111].

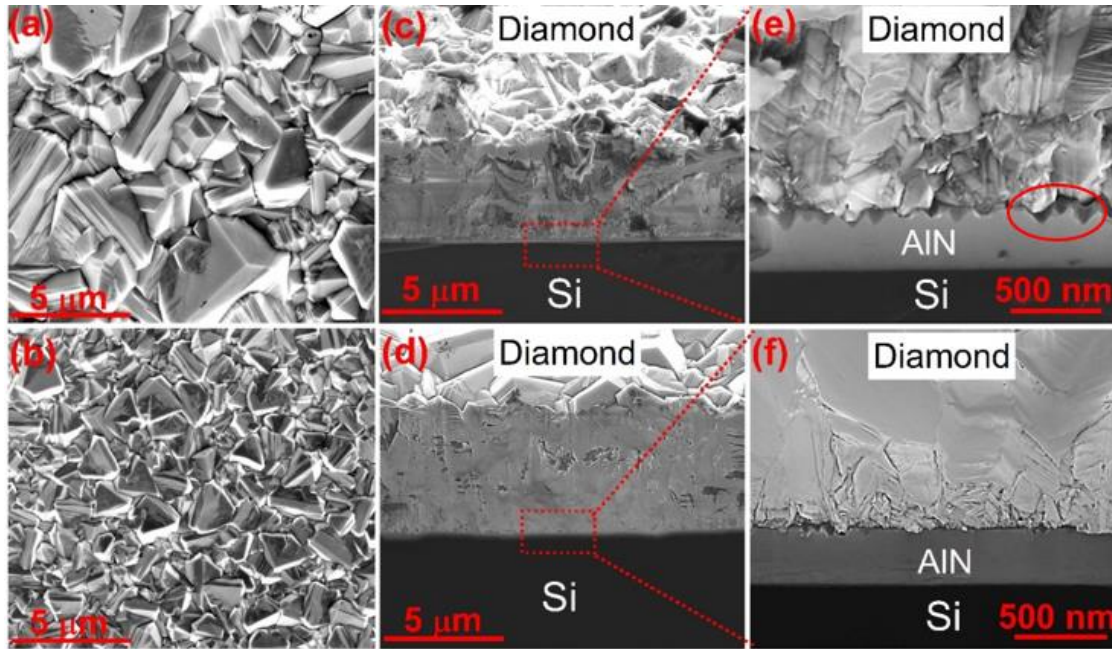


Figure 6.2. (a)-(b) SEM morphology of diamond film on S-1 and S-2, respectively. (c)-(d) Cross-sectional SEM image for the sample S-1 with low magnification, respectively. (e)-(f) Cross-sectional SEM image for the sample S-1 with higher magnification, respectively taken from cleaved samples.

Cross-section SEM images from the cleaved samples were used to investigate diamond morphology along the growth direction after 20 h and are shown in Figure 6.2(c)-(d), at lower magnification and Figure 6.2(e)-(f), at higher magnification, for S-1 and S-2, respectively. Large diamond grains with columnar structure and, possibly, voids between the diamond and AlN is formed when isolated diamond grains coalesced with sample S-1 with low seed density. In contrast to S-1, the diamond-AlN interface is improved with an abrupt interface with dense diamond grains at the interface. The “V” shaped structure observed along the AlN surface, shown in Figure 6.2(e) by red circle, is associated with the dislocation defects within the AlN film [152,153] and is typical for this standard growth process employed by our research group.

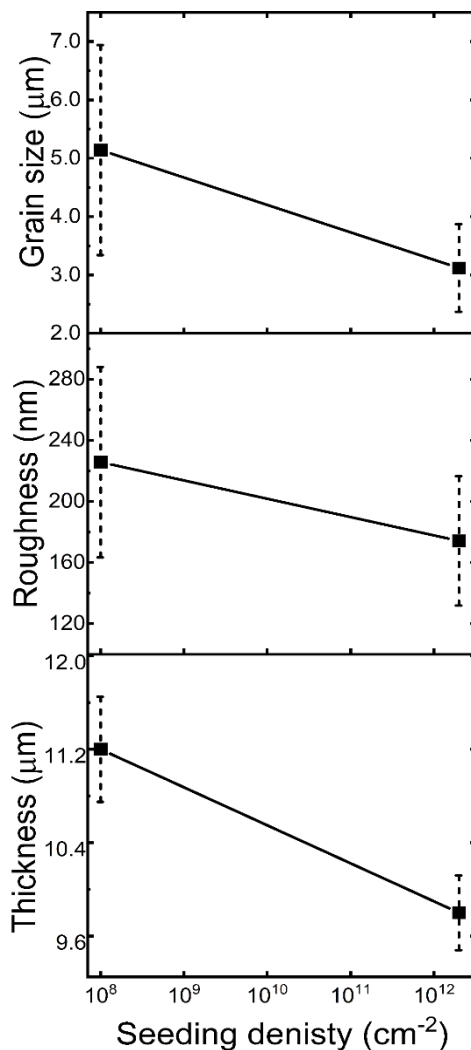


Figure 6.3. Average for three images of (a) grain size (b) and RMS roughness from AFM scans of diamond film on samples S-1& S-2 after 20 h growth. (c) Average thickness measured on samples S-1 & S-2 from cross-section SEM from cleaved samples.

Analysis of AFM images for the grain size and RMS roughness is shown in Figure 6.3(a)-(b). The mean grain size is larger for sample S-1 with low seed density and decreases with high seed density for sample S-2. The maximum lateral grain size for sample S-1 is due to the longer development of three-dimensional grains, as described

earlier. The uncertainties shown correspond to standard deviations in grain sizes. With increasing seed density, the earlier coalescence of the diamond grains and slow transformation of the diamond film into the van der Drift growth mode results in a smaller average grain size. The diamond surface roughness is greater for sample S-1 compared to S-2. Higher surface roughness is correlated to larger grain size.

The diamond film thickness measured from SEM cross-section for both samples after 20 h growth is shown in Figure 6.3(c). The corresponding average growth rates for S-1 and S-2, were determined to be 0.56 and 0.49 $\mu\text{m}/\text{h}$. The higher growth rate for the sample with lower seed density is attributed to freely developed diamond grains by the Volmer-Weber growth mode [117], as discussed previously. The grain size and roughness follow the increasing trends with diamond film thickness.

Raman analysis for crystallinity, quality, and stress on diamond film. Ultraviolet (UV) micro-Raman measurement were performed to investigate the carbon configuration of the diamond films. The Raman spectra is shown in Figure 6.4. The spectra were collected in the 200-2000 cm^{-1} range, but the AlN peaks are not observed due to the thick diamond film. The most probable bonding between diamond and AlN is carbide bond i.e Al-C or cyanide bond ($\text{C} \equiv \text{N}$) [148]. We didn't observe any peaks or bands associated with the aluminum carbide [154] and cyanide [155,156] while scanning ~ 100 nm diamond on AlN. The reason may be due to the presence of very thin carbide layers under the Raman detection volume. For all samples, a sharp O (\square)-symmetry phonon for diamond was observed with varying blue shift relative to the reference value of 1332.2 cm^{-1} . The broad features from 1350 to 1450 cm^{-1} and 1500 to 1620 cm^{-1} correspond to the "D" and "G" bands that are present in non-diamond carbon (NDC)

graphitic phase. Prior to quantitative analysis, it may observe that the diamond peak is more intense with suppressed NDC peak for sample S-2 compared to S-1.

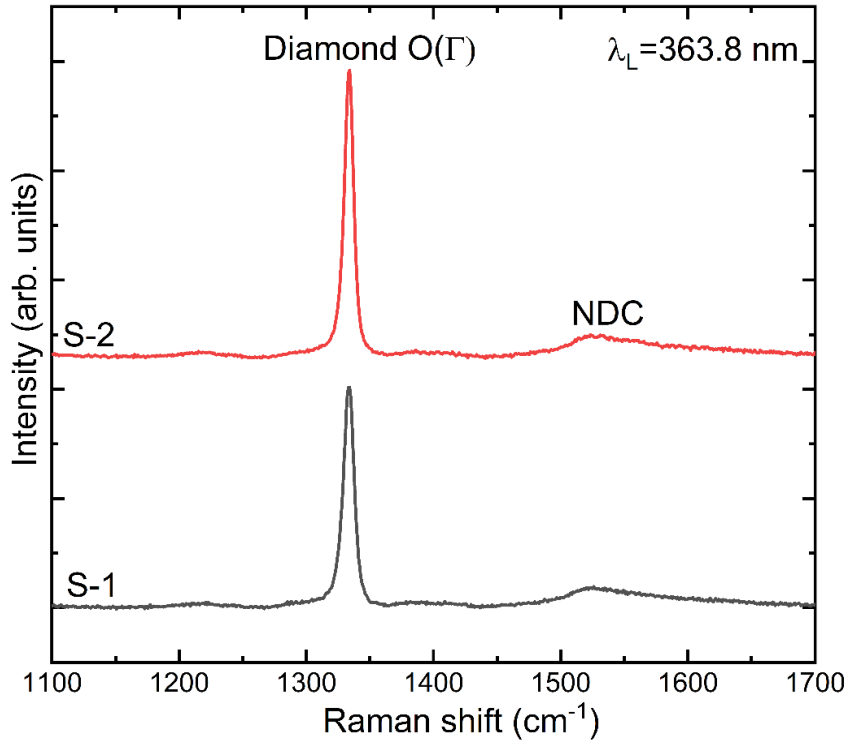


Figure 6.4. Raman spectra for diamond film after 20 h growth.

The quantitative information on diamond quality, crystallinity and stress is determined by the Lorentzian peak fitting with background subtraction [27]. The results are summarized in Figure 6.5. The upper panel of Figure 6.5(a) shows the increase in diamond phonon line width relative to the reference diamond. The diamond line narrows with increasing seeding density. Figure 6.5(b) show trends in relative intensity for diamond examined through $I_D/(I_D + I_{NDC})$, the ratio of integrated intensities of the diamond peak (I_D) to the total Raman intensity, where the I_{NDC} term is from the NDC bands, and following background subtraction. The relative intensity for diamond

increases systematically with S-2 compared to S-1. The results in Figure 6.5(a) and (b) quantitatively show improvement in diamond film crystal quality and intensity, respectively, due to higher seeding density.

The overall biaxial stress σ in the diamond film can be estimated from the Raman data using equation (15) with diamond reference ω_0 at 1332.2 cm^{-1} . The presence of residual stress developed in the diamond film is studied by examining the shift in the diamond phonon energy and the results are shown in Figure 6.5(c). The total residual stress is the sum of intrinsic stress and thermal stress. The thermal stress is calculated via equation (16), by including temperature dependent linear thermal expansion coefficients for diamond [121] and AlN[154], from room temperature, T_a to growth temperature T_g . The compressive thermal stress is estimated to be $\sim -3.3 \text{ GPa}$ for a $750 \text{ }^\circ\text{C}$ diamond deposition temperature. Figure 6.5(c) show the residual stress developed in the diamond films as a function of seeding density. The residual stress is compressive and stresses in the diamond films are -0.5 ± 0.2 and $-0.6 \pm 0.1 \text{ GPa}$ for S-1 and S-2, respectively. The uncertainty values are calculated by measuring the stress at different positions across the samples and taking the standard deviation. The stress variation on S-1 and S-2 is associated with different stress component contributions for different stages of the film formation.

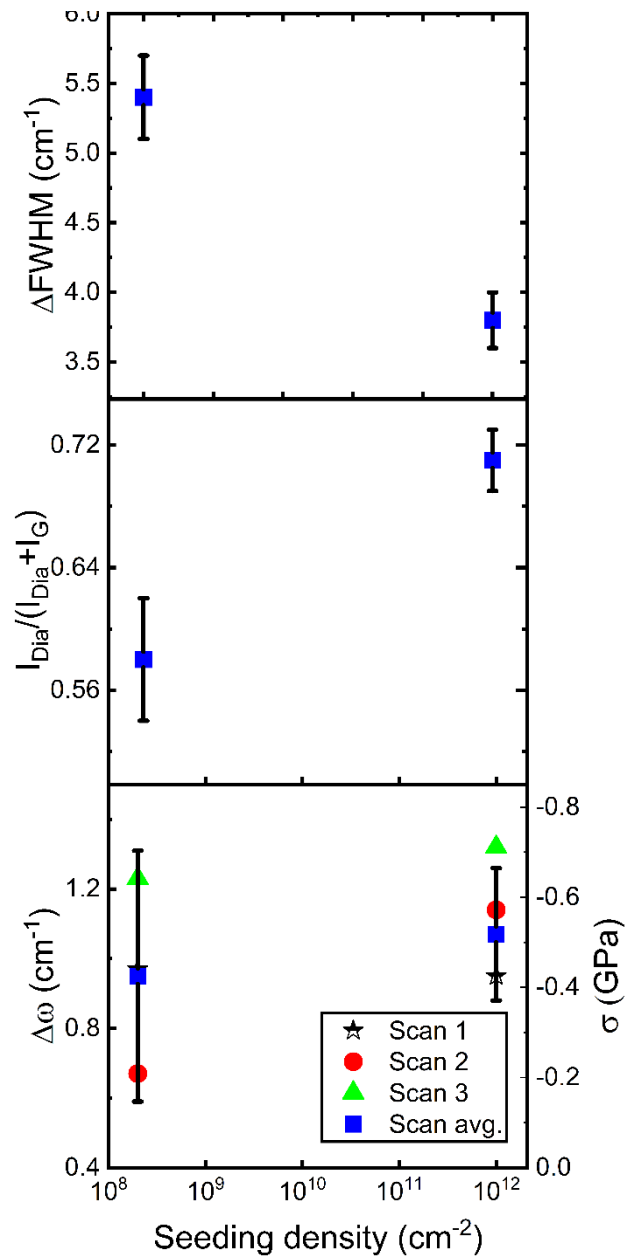


Figure 6.5. (a) Relative FWHM (b) Relative diamond intensity (c) Relative peak shift and stress, as a function of seeding density on the samples after 6 h and 16 h growth.

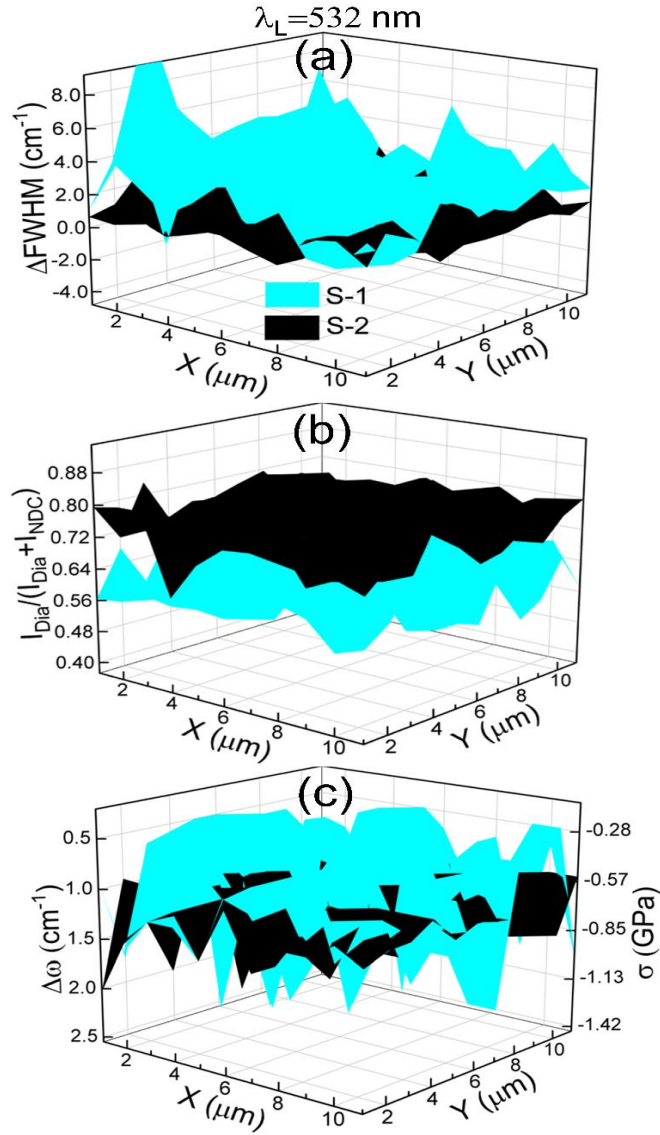


Figure 6.6. Map of diamond (a) relative FWHM (b) relative diamond intensity and (c) relative peak shift and stress measurements using visible micro-Raman spectroscopy.

The data from the UV-Raman measurement were cross-checked by performing $10 \times 10 \mu\text{m}^2$ mapping from visible micro-Raman using $\lambda_L = 532 \text{ nm}$. The results are summarized in Figure 6.6. Figure 6.6(a) compare relative FWHM measurements for samples S-1 and S-2 with respect to the reference FWHM of diamond of 5.9 cm^{-1} . Based

on the measurement, the relative FWHM of S-1 ranges from 1.2 to 9.4 cm^{-1} with an average of 5.2 cm^{-1} with uncertainty values of individual data points $\pm 3.1 \text{ cm}^{-1}$. The relative FWHM of S-2 ranges from 0.1 to 2.6 cm^{-1} with uncertainty value of $\pm 1.1 \text{ cm}^{-1}$. This indicates that the diamond crystal quality is better with increasing seed density and more uniform throughout the sample. This is explained due to the rapid coalescence and uniform diamond growth of S-2 from the early growth stage. The variation of relative FWHM for S-1 represents the non-uniform diamond growth. These data are consistent with the UV Raman measurement shown in Figure 6.5(a).

The relative diamond intensity within the mapped $10 \times 10 \mu\text{m}^2$ region is analyzed from the diamond Raman spectra and shown in Figure 6.6(b). The relative diamond intensity for sample S-1 ranges from 0.51 to 0.70 with an average of 0.60 ± 0.04 . The diamond volume fraction increases for sample S-2, ranging between 0.61 to 0.87 with an average of 0.74 ± 0.05 . This indicates that the diamond film quality is improved for the diamond film grown with high seeding density.

The peak position mapped from visible micro-Raman measurements of the diamond $\text{O}(\Gamma)$ phonon is shown in Figure 6.6(c), along with the corresponding stress values on the right-hand axis. The stress is calculated using the relative peak shift indicated in equation (15) with a reference peak position for diamond $\text{O}(\Gamma)$ at 1331.9 cm^{-1} . The compressive stress of sample S-1 from this measurement ranges from -0.23 to -1.46 GPa. An average compressive stress of $\sigma_{avg} = -0.57 \text{ GPa}$ was obtained across the wafer with uncertainty values of individual data points $\pm 0.20 \text{ GPa}$ and standard deviation of $\pm 0.10 \text{ GPa}$ from this map. The significant variation in the compressive stress of S-1 is attributed to variation of the non-diamond carbon phase within the diamond crystals.

Specifically, the low stress, ~ -0.23 GPa, within the scanned area is attributed to small voids enclosed between the diamond crystals due to the sparse seeding density during lateral diamond growth near the diamond-AlN interface. Higher intrinsic stress is developed in the diamond with less non-diamond phase [120,136]. The compressive stress of sample S-2 ranges from -0.53 to -1.30 GPa with an average compressive stress of $\sigma_{avg} = -0.65$ GPa with an uncertainty value of individual data points ± 0.06 GPa and standard deviation of ± 0.08 GPa from the map. The stress variation is substantially less and signifies that the uniformity and diamond quality are much improved with high seeding density. The average measured stress from visible Raman spectroscopy is consistent with the UV micro-Raman measurements. Larger variation in each measured stress data from visible Raman is due to larger area of scan compared to the UV micro-Raman spectroscopy.

Cross-section Raman spectroscopy. The diamond film quality was also characterized by cross-section Raman spectroscopy. A series of cross-section spectra were measured with Visible micro-Raman spectroscopy from the near interface to the growth surface. All scans were taken from the same region but not at the same position. All spectra exhibit a narrow diamond peak and broad non-diamond carbon bands. The scans were taken starting near the diamond-AlN interface (marked $0 \mu\text{m}$) to the growth surface ($10 \mu\text{m}$) with a step size of $1 \mu\text{m}$. The diamond reference sample was measured prior to each measurement with $O(\Gamma)$ at 1331.9 cm^{-1} and FWHM of 5.9 cm^{-1} . For all samples, the NDC intensity decreases along the scan direction from the near interface to the growth surface, identical to the trend for diamond on Si, discussed in Chapter IV.

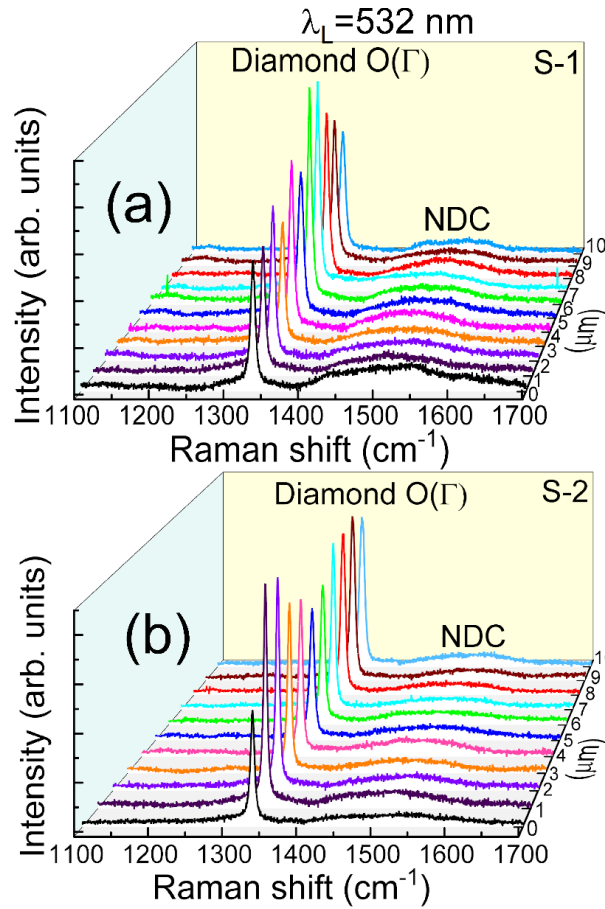


Figure 6.7. Visible Cross-section micro-Raman spectra of diamond from near interface with AlN (0 μm) to near-growth surface (10 μm) for samples S-1 and S-2, respectively.

A broad Raman band is observed across the range 1400-1650 cm^{-1} for sample S-1 near the interface as shown in Figure 6.7(a) and is attributed to a mixture of diamond-like and amorphous carbon. The appearance of such an NDC band is associated with amorphous interface regions between the diamond polycrystals. During the initial phase of growth with low seed density, the scattered seeds start to grow both vertically and laterally, and there is no spontaneous nucleation in the regions between the diamond seeds, similar to what was observed with a Si surface, discussed in Chapter IV. Such

regions are exposed to the HFCVD carbon environment and may diffuse into the layer/substrate. For the present samples, carbon adatoms may bond with Al and N to form Al-C or possibly $C\equiv N$ and accumulate into three-dimensional amorphous carbon clusters near the interfacial region [148]. This carbon is predominantly sp^2 -bonded and, thus, the lower diamond nucleation density will exhibit the broad sp^2 band near the interface. With increasing diamond film thickness, the quality of the film improves, and the intensity of this band diminishes. In contrast to S-1, the NDC band is narrower and its intensity lower at the interface and throughout the diamond film for S-2, shown in Figure 6.7(b).

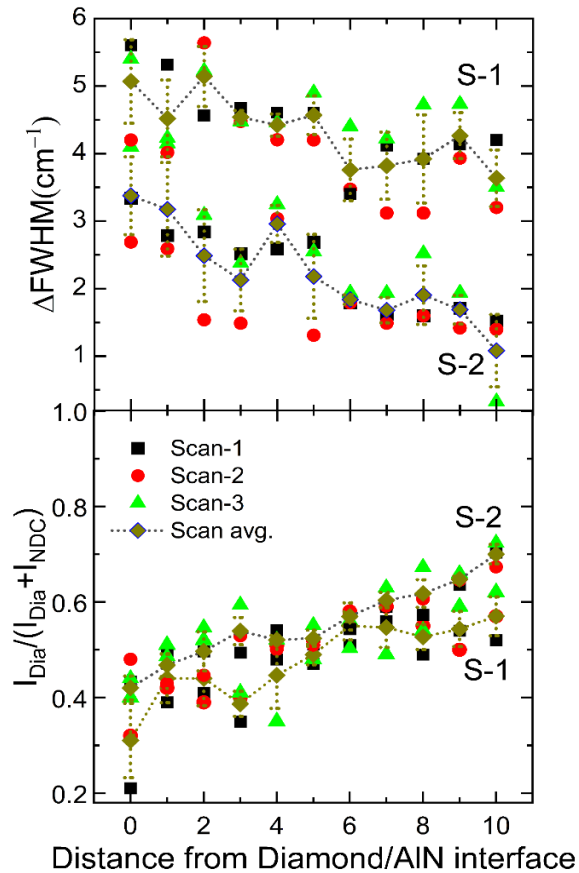


Figure 6.8. Visible micro-Raman results for (a) relative FWHM and (b) Relative diamond intensity as a function of distance from AlN/Diamond interface for all samples.

The quantitative analysis for relative FWHM and diamond intensity for samples S-1 and S-2 from the cross-section Raman spectra shown in Figure 6.7 is summarized in Figure 6.8. The variation in relative diamond FWHM for both samples measured near the interface to the growth surface is shown in Figure 6.8(a). There is a systematic narrowing of the diamond line with increasing diamond film thickness for both samples. The narrowing lines correspond to improving crystal quality with diamond film thickness. Furthermore, there is a consistent trend of superior crystal quality (lower DFWHM) with thickness for S-2, the diamond film with higher seed density. The variation in relative diamond intensity from the interface to the growth surface measured from visible micro-Raman spectroscopy, is shown in Figure 6.8(b). For both samples, the diamond growth begins with material that has the lowest diamond phase near the interface while the diamond fraction increases with increasing thickness toward the growth surface. Furthermore, comparing S-1 and S-2 in Figure 6.8(b), the relative diamond phase is enhanced throughout the layer with higher diamond seed density.

The larger diamond phase and narrower FWHM near the AlN/diamond interface with high seed density (S-2) compared to the lower seed density (S-1) is due to the difference in diamond growth mechanisms during the diamond nucleation process, explained previously. These studies show that the diamond seeding density has a profound effect on the diamond film quality, phase purity and crystallinity from the interface to the growth surface for AlN/diamond heterostructures.

Integration of Diamond on High Al Content $\text{Al}_x\text{Ga}_{1-x}\text{N}$ ($x = 52\%$) with High Seeding Density

In this section, the direct integration of diamond on high Al content AlGa_N with high seeding density is presented. The diamond integration on $\text{Al}_{0.52}\text{Ga}_{0.48}\text{N}$ with high seeding density is expected to help protect the layer from the harsh HFCVD diamond growth environment. Characterization techniques including atomic force microscopy (AFM), high resolution X-ray diffraction (HRXRD) and scanning electron microscopy (SEM) were employed to analyze the samples before and after the diamond growth.

Diamond seeding and diamond growth. To deposit $\text{Al}_{0.52}\text{Ga}_{0.48}\text{N}$ on Si (111) via MOCVD, the growth starts with an AlN nucleation layer followed by the AlGa_N alloy layer. The process has been established on Si (111) due to its smaller lattice mismatch with the III-nitride hexagonal crystal. After heating the substrate to ~1020 °C, ammonia is first introduced for a few seconds to nitridate the Si surface. This nitridation is extremely important for nucleation of III-nitride semiconductors on Si. The chamber pressure and substrate temperature are held constant at 100 Torr and 1020 °C, respectively. A nominally thick 420 nm AlN layer is deposited using TMA and ammonia with a V/III ratio of 9433. The flow rate for TMA and NH₃ are 30.3 μmole/min and 0.295 mole/min, respectively, for this layer. A 550 nm thick $\text{Al}_{0.52}\text{Ga}_{0.48}\text{N}$ layer is grown on top of AlN. The V/III ratio for this layer is 5530 with TMG flow of 29.75 μmole/min, TMA flow of 23.5 μmole/min and 0.295 mole/min of NH₃.

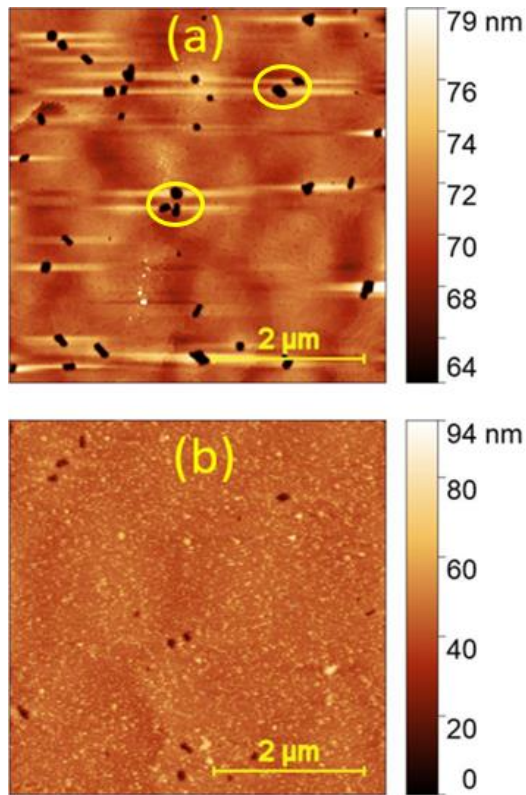


Figure 6.9. $(5 \times 5) \mu\text{m}^2$ AFM morphology of the $\text{Al}_{0.52}\text{Ga}_{0.48}\text{N}$ sample (a) before and (b) after diamond seeding.

The AFM morphology of the $\text{Al}_{0.52}\text{Ga}_{0.48}\text{N}$ sample prior to diamond seeding is shown in Figure 6.9(a). These dark spots on the sample with hexagonal inverted shaped pyramids are dislocation pits of $\sim 80 \text{ nm}$ width and $\sim 75 \text{ nm}$ vertical height, shown by a yellow circle in Figure 6.9(a). The average surface roughness is measured to be $\sim 3.29 \text{ nm}$. The density of the dislocation pits on the sample were found to be $> 10^8 \text{ cm}^{-2}$. In some regions, the density of such pits was found to be significantly decreased and depends upon the microstructure of the underlying AlN thin film. These hexagonal defects are similar to the so called “V” defects typically observed in GaN [158].

For diamond seeding, a mixed electrostatic dip seeding approach using a cationic Poly (diallyl dimethyl) ammonium chloride, commonly known as PDDAC polymer and nano diamond slurry carboxylate on water (1 wt% vol) was used. The details of the seeding process are presented in Chapter III. With this seeding approach, the diamond seeding density can be the excess of 10^{12} cm⁻². The AFM morphology of the seeded Al_{0.52}Ga_{0.48}N sample is shown in Figure 6.9(b). The surface is uniformly covered with dense nano-diamond seeds with a density $> 10^{12}$ cm⁻². AFM data shows no voids between the seed on the sample. The hot filament chemical vapor deposition (HFCVD) process for the diamond growth was carried at 3% methane (57sccm) at 750°C for 2 h.

X-ray diffraction analysis. The samples before and after the diamond growth were characterized using high resolution x-ray diffraction technique. Theta/two theta scans for the sample prior to and after diamond growth are shown in Figure 6.10. The HRXRD data indicate to what extent the underlying AlGa_N layer has been protected after CVD diamond growth in the HFCVD environment. Both III-nitride layer's (AlN and AlGa_N) second order (0002) diffraction peaks are present and have not substantially changed before and after the diamond growth. This confirms that the Al_{0.52}Ga_{0.48}N layer beneath the diamond layer is fully protected by the direct integration of diamond with high seeding density. Following diamond growth, the corresponding diamond (111) diffraction peak is present at 43.90°.

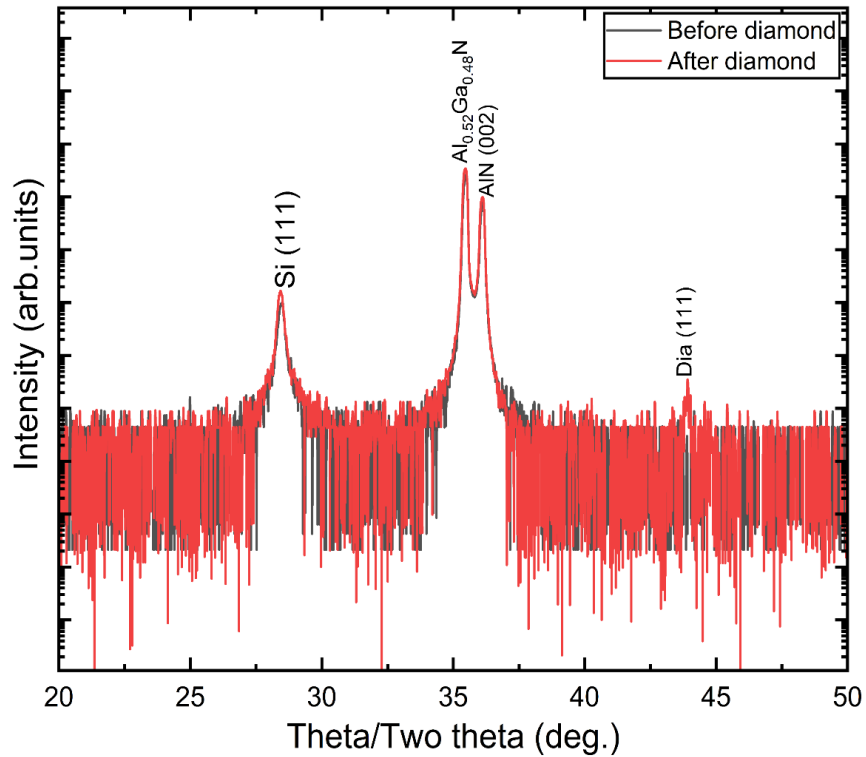


Figure 6.10. HRXRD θ - 2θ spectrum of the AlGaIn/AlN structure on Si (111) before and after diamond growth.

In addition, the FWHM values for the $\text{Al}_{0.52}\text{Ga}_{0.48}\text{N}$ layer were determined from ω – scans as shown in Figure 6.11. The measured FWHM before and after diamond growth are 1020 ± 35 and 991 ± 25 arc sec, respectively. The variation in FWHM is the standard deviation taken from three different measurements taken at different positions across the sample. The slight improvement in FWHM after diamond growth is not considered substantial as the values are within same order while considering the standard deviation for the measurements. This confirms that the material quality has not been negatively impacted by the diamond growth or the HFCVD environment. I.e., no etching or damage of the $\text{Al}_{0.52}\text{Ga}_{0.48}\text{N}$ layer is observed from the HRXRD data.

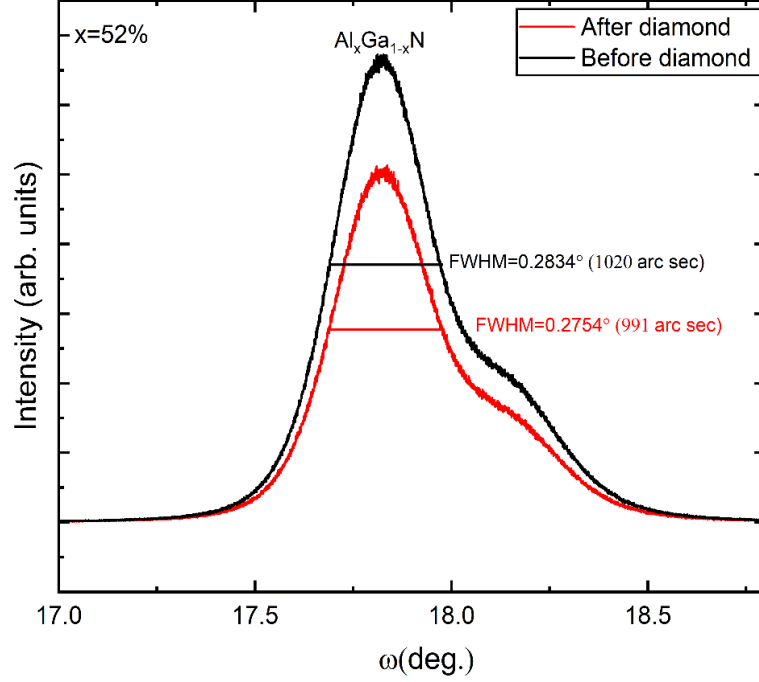


Figure 6.11. 2θ - ω scan for $\text{Al}_{0.52}\text{Ga}_{0.48}\text{N}$ sample before and after diamond growth.

Reciprocal space mapping (RSM). Reciprocal space mapping (RSM) analysis was conducted to determine the lattice constant and stress-strain phenomena in the $\text{Al}_x\text{Ga}_{1-x}\text{N}$ ($x=.52$) layer. Figure 6.12(a)-(b) show the asymmetric RSM for $\text{Al}_{0.52}\text{Ga}_{0.48}\text{N}/\text{AlN}$ grown on Si (111) before and after diamond growth. The stress of the AlGaN layer is calculated using peak positions in the RSM data. The reciprocal lattice vector q_{hkl} is defined in terms of inter planar spacing d_{hkl} as

$$q_{hkl} = \frac{1}{d_{hkl}} = \sqrt{\frac{4(h^2+k^2+hk)}{3a^2} + \frac{l^2}{c^2}} \quad (18)$$

where a and c are the in-plane and out-plane lattice constants, respectively. Hence, for a given reciprocal lattice point (hkl) in the scattering plane, the horizontal components of

reciprocal lattice vectors are [149]

$$q_{hkl}(\parallel) = \sqrt{\frac{4(h^2+k^2+hk)}{3a^2}} \quad (19)$$

Equation (19) is simplified when substituting $h=1$, $k=0$, and $l=4$ for the (10-14) reflection

$$q_{104}(\parallel) = \frac{2}{\sqrt{3}} \frac{1}{a} \quad (20)$$

The lattice constant a -axis parameter is measured from equation (20) using the RSM measured value of $q_{104}(\parallel)$. Based on the measurement the lattice constants (a_m , c_m) for the $\text{Al}_{0.52}\text{Ga}_{0.48}\text{N}$ layer before and after diamond growth are calculated as (3.183, 5.061) Å and (3.186, 5.062) Å, respectively. The in-plane biaxial strain (ε_{xx}^b) of the $\text{Al}_{0.52}\text{Ga}_{0.48}\text{N}$ layer can be expressed as a linear combination of uniaxial in-plane strain, along a direction, and hydrostatic strain ε_h can be expressed as follows [140,159].

$$\varepsilon_{xx}^b = \varepsilon_{xx} - \varepsilon_h \quad (21)$$

$$\varepsilon_{xx}^b = \frac{a_m(x) - a_o(x)}{a_o(x)} - \varepsilon_h \quad (22)$$

where subscripts “m” and “o” refer to the measured and relaxed lattice parameters, respectively. In-plane biaxial stress (σ_{bs}) can be expressed in terms of biaxial strain (ε_{xx}^b) and biaxial elastic modulus (M_f) [149,160],

$$\sigma_{bs} = M_f \varepsilon_{xx}^b \quad (23)$$

$$M_f = C_{11} + C_{12} - 2 \frac{C_{13}^2}{C_{33}} \quad (24)$$

Here, C_{ij} is the elastic constants of $\text{Al}_{0.52}\text{Ga}_{0.48}\text{N}$ calculated using Vegard’s law [161]. We use for these $C_{11} = 399$ GPa, $C_{12} = 147$ GPa, $C_{13} = 102$ GPa, and $C_{33} = 374$ vGPa,

respectively [160]. The relaxed lattice parameter was measured using Vegard's law for relaxed Al composition ($x=0.52$) and relaxed elastic constants for AlN and GaN [149], the relaxed lattice constants for $\text{Al}_{0.52}\text{Ga}_{0.48}\text{N}$ were calculated and found to be $a_0 = 3.176 \text{ \AA}$ and $c_0 = 5.088 \text{ \AA}$. Using the measured lattice constant and unstrained lattice constant using equations (18), (19) and (20), the biaxial stress on $\text{Al}_{0.52}\text{Ga}_{0.48}\text{N}$ was determined to be 1.08 GPa and the stress increased to 1.54 GPa after diamond integration.

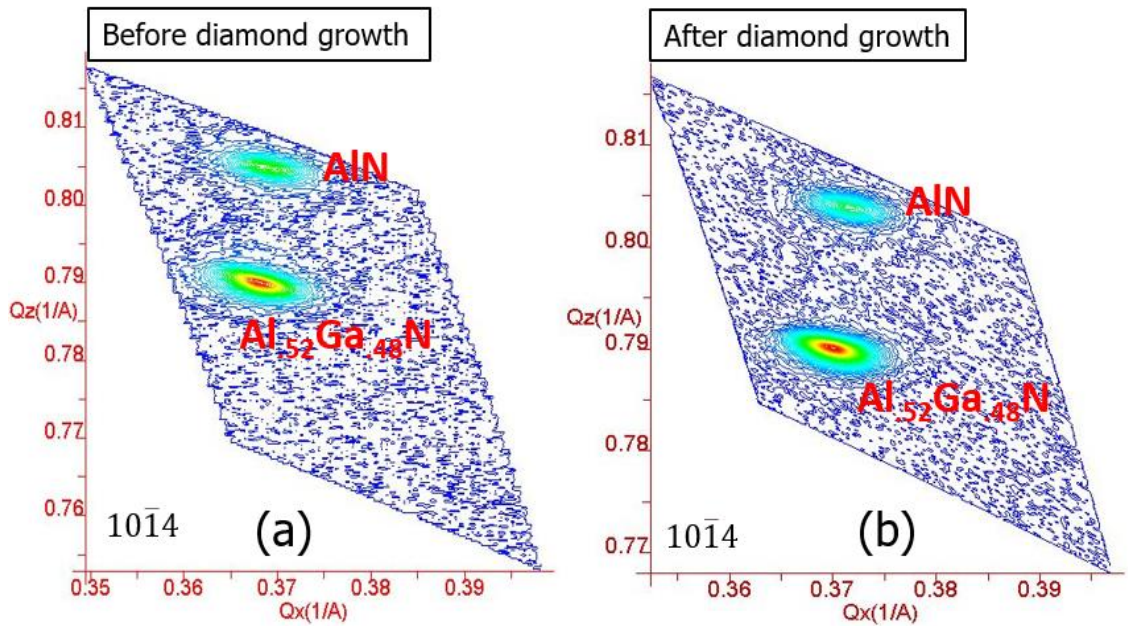


Figure 6.12. Asymmetric RSM ($10\bar{1}4$) scan of the $\text{Al}_{0.52}\text{Ga}_{0.48}\text{N}/\text{AlN}$ thin film grown on Si (a) before and (b) after diamond growth.

Cross-section scanning electron microscopy and morphology. While the structural and material properties of the $\text{Al}_{0.52}\text{Ga}_{0.48}\text{N}$ layer before and after diamond growth were investigated using HRXRD, it is also important to study the interface properties. To do so, cross-sectional SEM measurements were taken before and after diamond growth, as

shown in Figure 6.13(a)-(b). The $\text{Al}_{0.52}\text{Ga}_{0.48}\text{N}$ layer was found to not be impacted after diamond integration. The interface is between the diamond and $\text{Al}_{0.52}\text{Ga}_{0.48}\text{N}$ layer is abrupt without any indications of etching or damage. This confirms that diamond integration on $\text{Al}_{0.52}\text{Ga}_{0.48}\text{N}$ is successful without substantial material quality degradation from the harsh HFVCD conditions. The diamond film surface morphology is shown in Figure 6.13(c). The diamond grain structure is uniformly shaped with an average grain size of ~ 250 nm and an average film roughness of ~ 35 nm.

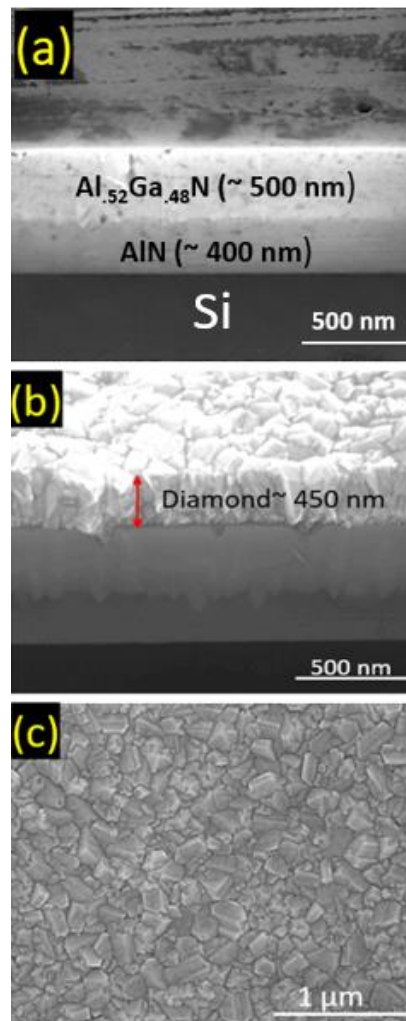


Figure 6.13. Cross-section SEM images taken (a) before and (b) after diamond growth, and (c) surface morphology of the diamond film.

Summary

The effect of diamond seeding density spanning from 1×10^8 to 2×10^{12} cm^{-2} on the growth, morphology, quality, and interfacial/material properties of diamond film grown on AlN was studied. The diamond film grown with low seed density was found to follow the Volmer Weber growth mechanism where the diamond nuclei grow three dimensionally with larger grains and higher surface roughness. In contrast, diamond grown with high seed density is substantially vertically aligned and follows the van der Drift growth mechanism. With low seed density the diamond-AlN interface is rough and contains voids near the interface due to the slower development of diamond grains. However, the absence of pores or voids and an abrupt interface is seen for the diamond film grown with dense seeding density. Due to the three-dimensional development of diamond grains with low seed density, the measured diamond film thickness is increased compared to the film grown with high seed density.

Micro Raman measurements confirm improvement of the diamond film quality with increasing diamond seed density. Visible Raman cross-section measurements show superior diamond film quality near the interface as well as throughout the film thickness with increasing seed density. This study indicates that high seed density $> 10^{12}$ cm^{-2} is critical for improving the overall diamond film quality, growth kinetics, thermal boundary conductance (TBC), and morphology of diamond film on AlN. Also, the effect of dense diamond seeding density $> 10^{12}$ cm^{-2} on the growth, morphology, and interfacial properties of diamond on $\text{Al}_{0.52}\text{Ga}_{0.48}\text{N}$ was investigated. High resolution XRD and rocking curve analysis confirmed that the diamond film mitigated etching and decomposition of the AlGa_N layer from the harsh HFCVD diamond growth conditions.

Cross-section SEM also confirmed an abrupt interface between the $\text{Al}_{0.52}\text{Ga}_{0.48}\text{N}$ layer and diamond. Reciprocal space mapping along the asymmetric $(10\bar{1}4)$ plane indicates the biaxial stress on the $\text{Al}_{0.52}\text{Ga}_{0.48}\text{N}$ layer to be 1.08 GPa and the stress increased to 1.54 GPa after diamond integration. This indicates that the diamond film produced a compressive biaxial stress without impacting the $\text{Al}_{0.52}\text{Ga}_{0.48}\text{N}$ layer crystal quality.

VII. CONCLUSIONS AND FUTURE WORKS

Conclusions

An innovative approach for diamond seeding to obtain dense diamond seed density on different semiconductor surfaces has been developed. The effect of diamond seeding density on growth, morphology, quality, interfacial/material, and thermal properties has been studied. Successful integration of high-quality diamond on Si, GaN, AlN and high Al-content AlGaN with dense diamond seeding density has been achieved and studied in detail. The key findings from this dissertation project include:

- i. Electrostatic van der Waal forces between the nano-diamond seeds and the substrate is necessary to attain dense diamond seeding.
- ii. Diamond growth dynamics depend on the available seed density on the substrate for the nucleation process. The Volmer Weber growth (three dimensional) mechanism is dominant for diamond films with sparse seed density and van der Drift (mostly 2-D) growth mechanism is dominant with dense diamond seed density.
- iii. The coalescence time for diamond film depends on the available diamond seeds for the nucleation process. Minimum thickness~100 nm is found to achieve 100 % coalescence with dense diamond seeding.
- iv. Diamond film quality and morphology is improved with dense diamond seed density compared to sparse seed density.
- v. The diamond-semiconductor interface is found to be porous and/or contain voids when grown with sparse seed density. In contrast, the absence of pores and/or voids was found for samples with dense seeding density.

- vi. The non-diamond carbon phase near the interface is found to be greater for diamond films grown with sparse seed density and substantially reduced for the samples grown with dense seeding density.
- vii. The thermal boundary conductance (TBC) between the diamond film and Si substrate is found to depend on the diamond seeding density. Improved TBC is found with increasing seeding density.
- viii. The quick lateral coverage of diamond during the early nucleation process helps to protect the underlying III-nitride layers from the harsh HFCVD environment. Hence, dense diamond seeding helps to protect the III-nitride layers from etching and decomposition during diamond growth.

Suggested Future Works

This dissertation research has provided a proof of concept for growing high quality diamond materials with dense diamond seeding. An innovative approach for diamond seeding developed on different semiconductors under this research opens many exciting research opportunities in the application of diamond as a heat spreader in different electronic devices as well as several other applications of diamond on optoelectronics. The most interesting research projects are summarized below:

Optimization of dielectric adhesion layer thickness between diamond and GaN HEMT with dense diamond seeding approach. This research establishes a dense seeding approach over 10^{12} cm^{-2} that results in relatively quick lateral coverage for diamond on different semiconductors. Thus, utilizing the seeding concept should help to decrease the required thickness of a dielectric adhesion layer between the diamond and GaN HEMT to help reduce the effective thermal boundary resistance of the structure.

Also, the quality of diamond is improved with dense seeding to further help better thermal management of the devices.

Study on the diamond film texture grown with different seeding density. From this dissertation research, the diamond growth kinetics were found to differ with different seeding density. The growth kinetics of diamond plays a key role in maintaining the texture and orientation of diamond nuclei. So, texture development of the diamond film can be further understood if a systematic study is performed on the effect of diamond seeding density on the texture development of the diamond film. Also, the effect of diamond seeding density on texture from early nucleation to the final film thickness is important to understand the texture development during growth of the diamond film.

Selective diamond growth with high diamond seeding density. The results of this dissertation suggest that the dense seeding approach is effective at improving the diamond quality as well as reducing the effective thermal boundary resistance between the diamond and underlying semiconductor surface. Also, diamond with superior crystal quality has lower defect density and reduces the stress variation of the diamond film. So, selective growth of diamond using the high seeding density should be established to fabricate electronic devices. This should reduce the effective thermal boundary resistance as well as global stress generated when integrating diamond on UWBG devices.

Effect of diamond seed size for effective thermal boundary conductance and conductivity of diamond film. The nucleation and growth of the diamond film depends on the initial diamond seeding on the substrate. The contact area between the diamond and semiconductor surface is essential for optimizing the thermal conductance as well as the overall diamond film quality. Thus, a systematic study should be conducted based on

diamond seed size on the thermal conductivity and overall thermal boundary conductance of the diamond film.

REFERENCES

- [1] O. Ambacher, *Growth and Applications of Group III-Nitrides*, Journal of Physics D: Applied Physics **31**, 2653 (1998).
- [2] M. E. Levinshtein, S. L. Rumyantsev, and M. S. Shur, *Properties Of Advanced Semiconductor Materials GaN,AlN,InN,BN,SiC,SiGe* (A wiley-interscience publications, 2001).
- [3] G. Cywiński, K. Szkudlarek, I. Yahniuk, S. Yatsunenko, M. Siekacz, C. Skierbiszewski, D. B. But, D. Coquillat, N. Dyakonova, and W. Knap, *GaN/AlGaN Based Transistors for Terahertz Emitters and Detectors*, in *2016 21st International Conference on Microwave, Radar and Wireless Communications, MIKON 2016* (Institute of Electrical and Electronics Engineers Inc., 2016).
- [4] N. Dyakonova, D. Coquillat, D. B. But, F. Teppe, W. Knap, P. Faltermeier, P. Olbrich, S. D. Ganichev, K. Szkudlarek, and G. Cywinski, *Terahertz Detection by AlGaN/GaN HEMTs at High Intensity*, in *2016 21st International Conference on Microwave, Radar and Wireless Communications, MIKON 2016* (Institute of Electrical and Electronics Engineers Inc., 2016).
- [5] A. El Fatimy, N. Dyakonova, Y. Meziani, T. Otsuji, W. Knap, S. Vandenbrouk, K. Madjour, D. Théron, C. Gaquiere, M. A. Poisson, S. Delage, P. Prystawko, and C. Skierbiszewski, *AlGaN/GaN High Electron Mobility Transistors as a Voltage-Tunable Room Temperature Terahertz Sources*, Journal of Applied Physics **107**, 024504 (2010).
- [6] D. Marti, S. Tirelli, A. R. Alt, J. Roberts, and C. R. Bolognesi, *150-GHz Cutoff Frequencies and 2-W/Mm Output Power at 40 GHz in a Millimeter-Wave AlGaN/GaN HEMT Technology on Silicon*, IEEE Electron Device Letters **33**, 1372 (2012).
- [7] J. W. Johnson, E. L. Piner, A. Vescan, R. Therrien, P. Rajagopal, J. C. Roberts, J. D. Brown, S. Singhal, and K. J. Linthicum, *12 W/MM AlGaN-GaN HFETs on Silicon Substrates*, IEEE Electron Device Letters **25**, 459 (2004).
- [8] Y. -f. Wu, M. Moore, A. Saxler, T. Wisleder, and P. Parikh, *40-W/MM Double Field-Plated GaN HEMTs*, in *IEEE* (Institute of Electrical and Electronics Engineers (IEEE), 2006), pp. 151–152.
- [9] M. Nazari, B. L. Hancock, E. L. Piner, and M. W. Holtz, *Self-Heating in a GaN-Based Heterojunction Field-Effect Transistor Investigated by Ultraviolet and Visible Micro-Raman Spectroscopy*, in *2015 IEEE Compound Semiconductor Integrated Circuit Symposium, CSICS 2015* (Institute of Electrical and Electronics Engineers Inc., 2015), pp. 1–4.

- [10] F. Faili, N. Palmer, S. Oh, and D. Twitchen, *Physical and Thermal Characterization of CVD Diamond: A Bottoms-up Review*, in *16th IEEE Intersociety Conference on Thermal and Thermomechanical Phenomena in Electronic Systems (ITherm)* (IEEE, 2017), pp. 79–86.
- [11] B. Dai, J. Zhao, V. Ralchenko, A. Khomich, A. Popovich, K. Liu, G. Shu, G. Gao, S. Mingqi, L. Yang, P. Lei, J. Han, and J. Zhu, *Thermal Conductivity of Free-Standing CVD Diamond Films by Growing on Both Nuclear and Growth Sides*, *Diamond and Related Materials* **76**, 9 (2017).
- [12] J. D. Blevins, G. D. Via, K. Sutherlin, S. Tetlak, B. Poling, R. Gilbert, B. Moore, J. Hoelscher, B. Stumpff, A. Bar-Cohen, J. J. Maurer, and A. Kane, *Recent Progress in GaN-on-Diamond Device Technology*, CS MANTECH 2014 - 2014 International Conference on Compound Semiconductor Manufacturing Technology 105 (2014).
- [13] F. Ejeckam, D. Francis, F. Faili, D. Twitchen, B. Bolliger, and J. Felbinger, *GaN-on-Diamond: A Brief History*, in *IEEE* (Ithaca, NY, USA, 2014), pp. 1–5.
- [14] J. Cho, Z. Li, M. Asheghi, and K. E. Goodson, *Near-Junction Thermal Management: Thermal Conduction in Gallium Nitride Composite Substrates*, *Annual Review of Heat Transfer* **18**, 7 (2015).
- [15] C. Gu, Z. Jin, X. Lu, G. Zou, J. Zhang, and R. Fang, *The Deposition of Diamond Film with High Thermal Conductivity*, *Thin Solid Films* **311**, 124 (1997).
- [16] Z. Feng, K. Komvopoulos, I. G. Brown, and D. B. Bogy, *Effect of Graphitic Carbon Films on Diamond Nucleation by Microwave-plasma-enhanced Chemical-vapor Deposition*, *Journal of Applied Physics* **74**, 2841 (1993).
- [17] R. B. Heimann, S. E. Evsvukov, and Y. Koga, *Carbon Allotropes: A Suggested Classification Scheme Based on Valence Orbital Hybridization*, *Carbon* **35**, 1654 (1997).
- [18] J. J. Gracio, Q. H. Fan, and J. C. Madaleno, *Diamond Growth by Chemical Vapour Deposition*, *Journal of Physics D: Applied Physics* **43**, 374017 (2010).
- [19] E. Kohn, M. Adamschik, P. Schmid, A. Denisenko, A. Aleksov, and W. Ebert, *Prospects of Diamond Devices*, *Journal of Physics D: Applied Physics* **34**, R77 (2001).
- [20] M. N. R. Ashfold, P. W. May, C. A. Rego, and N. M. Everitt, *Thin Film Diamond by Chemical Vapour Deposition Methods*, *Chemical Society Reviews* **23**, 21 (1994).
- [21] P. W. May, *Diamond Thin Films: A 21st-Century Material*, *The Royal Society* **358**, 23 (2000).

- [22] R. Ahmed, Growth and Characterization of Nitride Semiconductors on Chemical Vapor Deposited Diamond, PhD Dissertation, Texas State University, 2018.
- [23] S. Rossi, Nanocrystalline Diamond Growth for Top Heat-Spreading Applications on GaN-Based Devices, Doctoral thesis, ulm university, 2015.
- [24] O. A. Williams, O. Douhéret, M. Daenen, K. Haenen, E. Osawa, and M. Takahashi, *Enhanced Diamond Nucleation on Monodispersed Nanocrystalline Diamond*, Chemical Physics Letters **445**, 255 (2007).
- [25] O. A. Williams, M. Nesladek, M. Daenen, S. Michaelson, A. Hoffman, E. Osawa, K. Haenen, and R. B. Jackman, *Growth, Electronic Properties and Applications of Nanodiamond*, Diamond and Related Materials **17**, 1080 (2008).
- [26] M. N. Touzelbaev and K. E. Goodson, *Impact of Nucleation Density on Thermal Resistance near Diamond-Substrate Boundaries*, Journal of Thermophysics and Heat Transfer **11**, 506 (1997).
- [27] R. Ahmed, A. Siddique, R. Saha, J. Anderson, C. Engdahl, M. Holtz, and E. Piner, *Effect of Precursor Stoichiometry on Morphology, Phase Purity, and Texture Formation of Hot Filament CVD Diamond Films Grown on Si (100) Substrate*, Journal of Materials Science: Materials in Electronics **31**, 8597 (2020).
- [28] H. A. Girard, S. Perruchas, M. Chaigneau, L. Vieille, J. Arnault, P. Bergonzo, J. Boilot, and T. Gacoin, *Electrostatic Grafting of Diamond Nanoparticles: A Versatile Route to Nanocrystalline Diamond Thin Films*, Applied Materials and Interfaces **1**, 2738 (2009).
- [29] V. Kunderát, An Investigation of Diamond Thin Film Deposition on Steel Substrates, PhD Thesis, Aston University, 2015.
- [30] K. Anupam, Preferentially Oriented Growth of Diamond Film on Silicon Substrate, MS Thesis, Texas State University, 2019.
- [31] H. Buchkremer-Hermanns, H. Ren, J. Utsch, and H. Weiss, *Optimization of MW-PACVD Diamond Deposition Parameters for High Nucleation Density and Growth Rate on Si₃N₄ Substrate*, Diamond and Related Materials **6**, 411 (1997).
- [32] A. Vanhulsel, J.-P. Celis, E. Dekempeneer, J. Meneve, J. Smeets, and K. Vercammen, *Inductively Coupled r.f. Plasma Assisted Chemical Vapour Deposition of Diamond-like Carbon Coatings*, Diamond and Related Materials **8**, 1193 (1999).
- [33] Ch. Wild, N. Herres, and P. Koidl, *Texture Formation in Polycrystalline Diamond Films*, Journal of Applied Physics **68**, 973 (1990).

- [34] C. Wild, P. Koidl, W. Müller-Sebert, H. Walcher, R. Kohl, N. Herres, R. Locher, R. Samlenski, and R. Brenn, *Chemical Vapour Deposition and Characterization of Smooth 100-Faceted Diamond Films*, *Diamond and Related Materials* **2**, 158 (1993).
- [35] C. Wild, R. Kohl, N. Herres, W. Müller-Sebert, and P. Koidl, *Oriented CVD Diamond Films: Twin Formation, Structure and Morphology*, *Diamond and Related Materials* **3**, 373 (1994).
- [36] J. E. Graebner and S. Jin, *Chemical Vapor Deposited Diamond for Thermal Management*, *JOM* **50**, 52 (1998).
- [37] J. E. Graebner, J. A. Mucha, L. Seibles, and G. W. Kammlott, *The Thermal Conductivity of Chemical-vapor-deposited Diamond Films on Silicon*, *Journal of Applied Physics* **71**, 3143 (1992).
- [38] J. E. Graebner, S. Jin, J. A. Herb, and C. F. Gardinier, *Local Thermal Conductivity in Chemical-vapor-deposited Diamond*, *Journal of Applied Physics* **76**, 1552 (1994).
- [39] M. N. Touzelbaev and K. E. Goodson, *Applications of Micron-Scale Passive Diamond Layers for the Integrated Circuits and Microelectromechanical Systems Industries*, *Diamond and Related Materials* **7**, 1 (1998).
- [40] W. Fortunato, A. J. Chiquito, J. C. Galzerani, and J. R. Moro, *Crystalline Quality and Phase Purity of CVD Diamond Films Studied by Raman Spectroscopy*, *Journal of Materials Science* **42**, 7331 (2007).
- [41] J. W. Ager and M. D. Drory, *Quantitative Measurement of Residual Biaxial Stress by Raman Spectroscopy in Diamond Grown on a Ti Alloy by Chemical Vapor Deposition*, *Physical Review B* **48**, 2601 (1993).
- [42] E. O. Johnson, *Physical Limitation on Frequency and Power Parameters of Transistors*, in *Semiconductor Devices: Pioneering Papers* (1991), pp. 295–302.
- [43] R. W. Keyes, *Figure of Merit for Semiconductors for High-Speed Switches*, *Proceedings of the IEEE* **60**, 225 (1972).
- [44] M. Levinshtein, S. Rumyantsev, and M. Shur, *Handbook Series on Semiconductor Parameters* (WORLD SCIENTIFIC, 1996).
- [45] M. Kim, J. H. Seo, U. Singiseti, and Z. Ma, *Recent Advances in Free-Standing Single Crystalline Wide Band-Gap Semiconductors and Their Applications: GaN, SiC, ZnO, β -Ga₂O₃, and Diamond*, *Journal of Materials Chemistry C* **5**, 8338 (2017).

- [46] J. Y. Tsao, S. Chowdhury, M. A. Hollis, D. Jena, N. M. Johnson, K. A. Jones, R. J. Kaplar, S. Rajan, C. G. Van de Walle, E. Bellotti, C. L. Chua, R. Collazo, M. E. Coltrin, J. A. Cooper, K. R. Evans, S. Graham, T. A. Grotjohn, E. R. Heller, M. Higashiwaki, M. S. Islam, P. W. Juodawlkis, M. A. Khan, A. D. Koehler, J. H. Leach, U. K. Mishra, R. J. Nemanich, R. C. N. Pilawa-Podgurski, J. B. Shealy, Z. Sitar, M. J. Tadjer, A. F. Witulski, M. Wraback, and J. A. Simmons, *Ultrawide-Bandgap Semiconductors: Research Opportunities and Challenges*, *Advanced Electronic Materials* **4**, 1600501 (2018).
- [47] D. L. Mauch, F. J. Zutavern, J. J. Delhotal, M. P. King, J. C. Neely, I. C. Kizilyalli, and R. J. Kaplar, *Ultrafast Reverse Recovery Time Measurement for Wide-Bandgap Diodes*, *IEEE Transactions on Power Electronics* **32**, 9333 (2017).
- [48] D. Kotchetkov, J. Zou, A. A. Balandin, D. I. Florescu, and F. H. Pollak, *Effect of Dislocations on Thermal Conductivity of GaN Layers*, *Applied Physics Letters* **79**, 4316 (2001).
- [49] J. Zou, D. Kotchetkov, A. A. Balandin, D. I. Florescu, and F. H. Pollak, *Thermal Conductivity of GaN Films: Effects of Impurities and Dislocations*, *Journal of Applied Physics* **92**, 2534 (2002).
- [50] J. J. Rosenberg, M. Benlamri, P. D. Kirchner, J. M. Woodall, and G. D. Pettit, *An In_{0.15}Ga_{0.85}As/GaAs Pseudomorphic Single Quantum Well HEMT*, *IEEE Electron Device Letters* **6**, 491 (1985).
- [51] T. Wu and B. Ozpineci, *Impact of Heat Dissipation Profiles on Power Electronics Packaging Design*, in *2018 IEEE Transportation Electrification Conference and Expo (ITEC)* (2018), pp. 482–487.
- [52] M. Y. Chernykh, A. A. Andreev, I. S. Ezubchenko, I. A. Chernykh, I. O. Mayboroda, E. M. Kolobkova, Yu. V. Khrapovitskaya, J. V. Grishchenko, P. A. Perminov, V. S. Sedov, A. K. Martyanov, A. S. Altakhov, M. S. Komlenok, V. P. Pashinin, A. G. Sinogeykin, V. I. Konov, and M. L. Zhanaveskin, *GaN-Based Heterostructures with CVD Diamond Heat Sinks: A New Fabrication Approach towards Efficient Electronic Devices*, *Applied Materials Today* **26**, 101338 (2022).
- [53] S. E. Coe and R. S. Sussmann, *Optical, Thermal and Mechanical Properties of CVD Diamond*, *Diamond and Related Materials* **9**, 1726 (2000).
- [54] D. Altman, M. Tyhach, J. McClymonds, S. Kim, S. Graham, J. Cho, K. Goodson, D. Francis, F. Faili, F. Ejeckam, and S. Bernstein, *Analysis and Characterization of Thermal Transport in GaN HEMTs on Diamond Substrates*, in *Thermomechanical Phenomena in Electronic Systems -Proceedings of the Intersociety Conference* (IEEE, 2014), pp. 1199–1205.
- [55] K. Yoshida and H. Morigami, *Thermal Properties of Diamond/Copper Composite Material*, *Microelectronics Reliability* **44**, 303 (2004).

- [56] H. Sun, D. Liu, J. Pomeroy, D. Francis, F. Faili, D. Twitchen, and M. Kuball, *GaN-on-Diamond: Robust Mechanical and Thermal Properties* (2016).
- [57] A. Sood, J. Cho, K. D. Hobart, T. Feygelson, B. Pate, M. Asheghi, and K. E. Goodson, *Anisotropic and Nonhomogeneous Thermal Conduction in 1 Mm Thick CVD Diamond*, in *Thermomechanical Phenomena in Electronic Systems - Proceedings of the Intersociety Conference* (IEEE, Orlando, FL, USA, 2014), pp. 1192–1198.
- [58] J. E. Graebner, S. Jin, G. W. Kammlott, B. Bacon, L. Seibles, and W. Banholzer, *Anisotropic Thermal Conductivity in Chemical Vapor Deposition Diamond*, *Journal of Applied Physics* **71**, 5353 (1992).
- [59] C. Monachon, L. Weber, and C. Dames, *Thermal Boundary Conductance: A Materials Science Perspective*, *Annual Review of Materials Research* **46**, 433 (2016).
- [60] M. Nazari, B. L. Hancock, J. Anderson, A. Savage, E. L. Piner, S. Graham, F. Faili, S. Oh, D. Francis, D. Twitchen, and M. Holtz, *Near-Ultraviolet Micro-Raman Study of Diamond Grown on GaN*, *Applied Physics Letters* **108**, 1 (2016).
- [61] T. Bai, Y. Wang, T. I. Feygelson, M. J. Tadjer, K. D. Hobart, N. J. Hines, L. Yates, S. Graham, J. Anaya, M. Kuball, and M. S. Goorsky, *Diamond Seed Size and the Impact on Chemical Vapor Deposition Diamond Thin Film Properties*, *ECS Journal of Solid State Science and Technology* **9**, 053002 (2020).
- [62] J. E. Butler, Y. A. Mankelevich, A. Cheesman, J. Ma, and M. N. R. Ashfold, *Understanding the Chemical Vapor Deposition of Diamond: Recent Progress*, *Journal of Physics Condensed Matter* **21**, 364201 (2009).
- [63] J. Ryou and R. D. Dupuis, *Chapter 6: CVD of III-V Compound Semiconductors*, in *Chemical Vapour Deposition: Precursors, Processes and Applications* (2009), pp. 272–319.
- [64] G. W. G. V. Dreumel, *GaN on Diamond: A Hot Combination?*, Doctoral thesis, Radboud University Nijmegen, 2011.
- [65] B. Chu, *Laser Light Scattering*, *Annual Review of Physical Chemistry* **21**, 145 (1970).
- [66] R. Pecora, *Doppler Shifts in Light Scattering from Pure Liquids and Polymer Solutions*, *The Journal of Chemical Physics* **40**, 1604 (1964).
- [67] J. Zmpitas and J. Gross, *Modified Stokes–Einstein Equation for Molecular Self-Diffusion Based on Entropy Scaling*, *Ind. Eng. Chem. Res.* **60**, 4453 (2021).

- [68] J. D. Clogston and A. K. Patri, *Zeta Potential Measurement*, in *Characterization of Nanoparticles Intended for Drug Delivery*, edited by S. E. McNeil (Humana Press, Totowa, NJ, 2011), pp. 63–70.
- [69] C. Yang, *Measuring Zeta Potential, Methods*, in *Encyclopedia of Microfluidics and Nanofluidics*, edited by D. Li (Springer US, Boston, MA, 2008), pp. 1068–1076.
- [70] T. Itoh, A. Sujith, and Y. Ozaki, *Surface-Enhanced Raman Scattering Spectroscopy: Electromagnetic Mechanism and Biomedical Applications*, *Frontiers of Molecular Spectroscopy* 289 (2009).
- [71] S. N. Magonov and D. H. Reneker, *Characterization of Polymer Surfaces with Atomic Force Microscopy*, *Annual Review of Materials Science* 27, 175 (1997).
- [72] N. Ishida and V. Craig, *Direct Measurement of Interaction Forces between Surfaces in Liquids Using Atomic Force Microscopy*, *KONA Powder and Particle Journal* 36, (2019).
- [73] R. Waser, *Nanoelectronics and Information Technology: Materials, Processes, Devices*, 2nd ed. (John Wiley & Sons, 2005).
- [74] G. Joseph I., D. E. Newbury, P. Echlin, C. Joy, C. Fiori, E. Lifshin, A. S. Pooley, J. I. Goldstein, E. Dale, P. Echlin, D. C. Joy, C. Fiori, and E. Lifshin, *Scanning Electron Microscopy and X-Ray Microanalysis: A Text For Biologists, Materials Scientists, And Geologists*, second (Plenum press, Newyork and London, 1992).
- [75] R. F. Egerton, P. Li, and M. Malac, *Radiation Damage in the TEM and SEM*, *Micron* 35, 399 (2004).
- [76] M. Joshi and A. Bhattacharyya, *Characterization Techniques for Nanotechnology Applications in Textiles*, *Indian Journal of Fibre and Textile Research* 33, 304 (2008).
- [77] P. J. D. Whiteside, J. A. Chininis, and H. K. Hunt, *Techniques and Challenges for Characterizing Metal Thin Films with Applications in Photonics*, *Coatings* 6, 35 (2016).
- [78] J. R. Dennison, M. Holtz, and G. Swain, *Raman Spectroscopy of Carbon Materials*, *Spectroscopy (Santa Monica)* 11, 38 (1996).
- [79] C. Manuel and M. Roberto, *Light Scattering in Solids IX, Novel Materials and Techniques*, Vol. 111 (Springer Berlin Heidelberg, 2008).
- [80] M. Nazari and M. W. Holtz, *Near-UV Raman and Micro-Raman Analysis of Electronic Materials*, *Applied Physics Reviews* 5, 041303 (2018).

- [81] S. Praver and R. J. Nemanich, *Raman Spectroscopy of Diamond and Doped Diamond*, Philosophical Transactions of the Royal Society A: Mathematical, Physical and Engineering Sciences **362**, 2537 (2004).
- [82] D. S. Knight and W. B. White, *Characterization of Diamond Films by Raman Spectroscopy*, Journal of Materials Research **16802**, 385 (1989).
- [83] M. Malakoutian, M. A. Laurent, and S. Chowdhury, *A Study on the Growth Window of Polycrystalline Diamond on Si₃N₄-coated N-polar GaN*, Crystals **9**, 1 (2019).
- [84] Andrew M. Ellis, Miklos Feher, and Timothy G. Wright, *Electronic and Photoelectronic Spectroscopy* (Cambridge University Press, 2012).
- [85] D. R. Baer, K. Artyushkova, H. Cohen, C. D. Easton, M. Engelhard, T. R. Gengenbach, G. Greczynski, P. Mack, D. J. Morgan, and A. Roberts, *XPS Guide: Charge Neutralization and Binding Energy Referencing for Insulating Samples*, Journal of Vacuum Science & Technology A **38**, 031204 (2020).
- [86] C. R. Brundle, *Photoelectron Spectroscopy: An Introduction to Ultraviolet Photoelectron Spectroscopy in the Gas Phase*, Physics Bulletin **26**, 129 (1975).
- [87] J. García, A. Sanz-Lobera, P. Maresca, T. Pareja, and C. Wang, *Some Considerations about the Use of Contact and Confocal Microscopy Methods in Surface Texture Measurement*, Materials **11**, 1484 (2018).
- [88] J. M. Thomas, *The Birth of X-Ray Crystallography*, Nature **491**, 186 (2012).
- [89] B. D. Cullity, *Elements of X Ray Diffraction* (Addison-Wesley Publishing Company InC., 1978).
- [90] J. L. Braun, D. H. Olson, J. T. Gaskins, and P. E. Hopkins, *A Steady-State Thermoreflectance Method to Measure Thermal Conductivity*, Review of Scientific Instruments **90**, 024905 (2019).
- [91] S. Mandal, *Nucleation of Diamond Films on Heterogeneous Substrates: A Review*, RSC Advances **11**, 10159 (2021).
- [92] S. Mandal, E. L. H. Thomas, C. Middleton, L. Gines, J. T. Gri, M. J. Kappers, R. A. Oliver, D. J. Wallis, L. E. Go, S. A. Lynch, M. Kuball, and O. A. Williams, *Surface Zeta Potential and Diamond Seeding on Gallium Nitride Films*, ACS Omega **2**, 7275 (2017).
- [93] H. Liu and D. S. Dandy, *Studies on Nucleation Process in Diamond CVD: An Overview of Recent Developments*, Diamond and Related Materials **4**, 1173 (1995).

- [94] X. Liu, T. Yu, Q. Wei, Z. Yu, and X. Xu, *Colloids and Surfaces A : Physicochemical and Engineering Aspects Enhanced Diamond Nucleation on Copper Substrates by Employing an Electrostatic Self-Assembly Seeding Process with Modified Nanodiamond Particles*, *Colloids and Surfaces A: Physicochemical and Engineering Aspects* **412**, 82 (2012).
- [95] C. J. Tang, A. J. Neves, and A. J. S. Fernandes, *Influence of Nucleation Density on Film Quality, Growth Rate and Morphology of Thick CVD Diamond Films*, *Diamond and Related Materials* **12**, 1488 (2003).
- [96] J. Hees, A. Kriele, and O. A. Williams, *Electrostatic Self-Assembly of Diamond Nanoparticles*, *Chemical Physics Letters* **509**, 12 (2011).
- [97] L. Fayette, M. Mermoux, and B. Marcus, *Role of the Nucleation Step in the Growth Rate of Diamond Films*, *Diamond and Related Materials* **3**, 480 (1994).
- [98] K. Tsugawa, M. Ishihara, Y. K. J. Kim, and M. Hasegawa, *Nucleation Enhancement of Nanocrystalline Diamond Growth at Low Substrate Temperatures by Adamantane Seeding*, *Journal of Physical Chemistry C* **114**, 3822 (2010).
- [99] N. Fujimori, T. Imai, and A. Doi, *Characterization of Conducting Diamond Films*, *Vacuum* **36**, 99 (1986).
- [100] J. C. Arnault, S. Saada, S. Delclos, L. Rocha, L. Intiso, R. Polini, A. Hoffman, S. Michaelson, and P. Bergonzo, *Surface Science Contribution to the BEN Control on Si(100) and 3C-SiC(100): Towards Ultrathin Nanocrystalline Diamond Films*, *Chemical Vapor Deposition* **14**, 187 (2008).
- [101] E. J. W. Smith, A. H. Piracha, D. Field, J. W. Pomeroy, G. R. Mackenzie, Z. Abdallah, F. C.-P. Massabuau, A. M. Hinz, D. J. Wallis, R. A. Oliver, M. Kuball, and P. W. May, *Mixed-Size Diamond Seeding for Low-Thermal-Barrier Growth of CVD Diamond onto GaN and AlN*, *Carbon* **167**, 620 (2020).
- [102] S. Mandal, E. L. H. Thomas, C. Middleton, L. Gines, J. T. Gri, M. J. Kappers, R. A. Oliver, D. J. Wallis, L. E. Go, S. A. Lynch, M. Kuball, and O. A. Williams, *Surface Zeta Potential and Diamond Seeding on Gallium Nitride Films*, *ACS Omega* **2**, 7275 (2017).
- [103] R. N. Tiwari, J. N. Tiwari, L. Chang, and M. Yoshimura, *Enhanced Nucleation and Growth of Diamond Film on Si by CVD Using a Chemical Precursor*, *Journal of Physical Chemistry C* **115**, 16063 (2011).
- [104] P. N. Barnes and R. L. C. Wu, *Nucleation Enhancement of Diamond with Amorphous Films*, *Applied Physics Letters* **62**, 37 (1993).
- [105] T. J. Woehl, K. L. Heatley, C. S. Dutcher, N. H. Talken, and W. D. Ristenpart, *Electrolyte-Dependent Aggregation of Colloidal Particles near Electrodes in Oscillatory Electric Fields*, *Langmuir* **30**, 4887 (2014).

- [106] D. Nečas and P. Klapetek, *Gwyddion: An Open-Source Software for SPM Data Analysis*, Central European Journal of Physics **10**, 181 (2012).
- [107] S. T. Lee, Z. Lin, and X. Jiang, *CVD Diamond Films: Nucleation and Growth*, Materials Science and Engineering R: Reports **25**, 123 (1999).
- [108] D. Das and R. N. Singh, *A Review of Nucleation, Growth and Low Temperature Synthesis of Diamond Thin Films*, International Materials Reviews **52**, 29 (2007).
- [109] S. K. Sarangi, D. K. Sahu, S. Padhi, and A. K. Chattopadhyay, *Nucleation and Growth of Diamond by Different Seeding Mechanisms on Cemented Carbide Inserts by HFCVD Process*, Aimtdr 1 (2014).
- [110] S. T. Lee, Z. Lin, and X. Jiang, *CVD Diamond Films: Nucleation and Growth*, Materials Science and Engineering R: Reports **25**, 123 (1999).
- [111] V. der Drift, *Evolutionary Selection, a Principle Governing Growth Orientation in Vapour-Deposited Layers.*, Philips Res. Rep. **22**, 267 (1967).
- [112] D. R. Gilbert, R. Singh, R. Clarke, and S. Murugkar, *Dynamic Growth Effects during Low-Pressure Deposition of Diamond Films*, Applied Physics Letters **70**, 1974 (1997).
- [113] R. Ahmed, M. Nazari, B. L. Hancock, J. Simpson, C. Engdahl, E. L. Piner, and M. W. Holtz, *Ultraviolet Micro-Raman Stress Map of Polycrystalline Diamond Grown Selectively on Silicon Substrates Using Chemical Vapor Deposition*, Applied Physics Letters **112**, 181907 (2018).
- [114] K. Paprocki, A. Dittmar-Wituski, M. Trzciński, M. Szybowicz, K. Fabisiak, and A. Dychalska, *The Comparative Studies of HF CVD Diamond Films by Raman and XPS Spectroscopies*, Optical Materials **95**, 109251 (2019).
- [115] X. Pan, L. Wang, Q. Zeng, L. Shi, R. Xu, J. Huang, K. Tang, and Y. Xia, *XPS Study of Polycrystalline Diamond Surfaces after Annealing Treatment*, Surface and Coatings Technology **228**, S446 (2013).
- [116] B. L. Prealas Mark, Popovici Galina, *Handbook of Industrial Diamonds and Diamond Films* (Marcel Dekker, New York, 1996).
- [117] K. A. Lozovoy, A. G. Korotaev, A. P. Kokhanenko, V. V. Dirko, and A. V. Voitsekhovskii, *Kinetics of Epitaxial Formation of Nanostructures by Frank–van Der Merwe, Volmer–Weber and Stranski–Krastanow Growth Modes*, Surface and Coatings Technology **384**, 125289 (2020).
- [118] K. Ganesan, P. K. Ajikumar, S. K. Srivastava, and P. Magudapathy, *Structural, Raman and Photoluminescence Studies on Nanocrystalline Diamond Films: Effects of Ammonia in Feedstock*, Diamond and Related Materials **106**, 107872 (2020).

- [119] A. C. Ferrari and J. Robertson, *Interpretation of Raman Spectra of Disordered and Amorphous Carbon.*, Physical Review B **31**, 632 (1969).
- [120] V. Jirásek, T. Ižák, M. Varga, O. Babchenko, and A. Kromka, *Investigation of Residual Stress in Structured Diamond Films Grown on Silicon*, Thin Solid Films **589**, 857 (2015).
- [121] P. Jacobson and S. Stoupin, *Thermal Expansion Coefficient of Diamond in a Wide Temperature Range*, Diamond and Related Materials **97**, 107469 (2019).
- [122] H. Watanabe, N. Yamada, and M. Okaji, *Linear Thermal Expansion Coefficient of Silicon from 293 to 1000 K*, International Journal of Thermophysics **25**, 221 (2004).
- [123] D. Fang, F. He, J. Xie, and L. Xue, *Calibration of Binding Energy Positions with C1s for XPS Results*, Journal Wuhan University of Technology, Materials Science Edition **35**, 711 (2020).
- [124] S. Kono, T. Kageura, Y. Hayashi, S. G. Ri, T. Teraji, D. Takeuchi, M. Ogura, H. Kodama, A. Sawabe, M. Inaba, A. Hiraiwa, and H. Kawarada, *Carbon 1s X-Ray Photoelectron Spectra of Realistic Samples of Hydrogen-Terminated and Oxygen-Terminated CVD Diamond (111) and (001)*, Diamond and Related Materials **93**, 105 (2019).
- [125] Y. Fan, A. G. Fitzgerald, P. John, C. E. Troupe, and J. I. B. Wilson, *X-Ray Photoelectron Spectroscopy Studies of CVD Diamond Films*, Surface and Interface Analysis **34**, 703 (2002).
- [126] C. J. Powell and A. Jablonski, *Surface Sensitivity of X-Ray Photoelectron Spectroscopy*, Nuclear Instruments and Methods in Physics Research, Section A: Accelerators, Spectrometers, Detectors and Associated Equipment **601**, 54 (2009).
- [127] J. I. B. Wilson, J. S. Walton, and G. Beamson, *Analysis of Chemical Vapour Deposited Diamond Films by X-Ray Photoelectron Spectroscopy*, Journal of Electron Spectroscopy and Related Phenomena **121**, 183 (2001).
- [128] P. Mérel, M. Tabbal, M. Chaker, S. Moisa, and J. Margot, *Direct Evaluation of the Sp³ Content in Diamond-like-Carbon Films by XPS*, Applied Surface Science **136**, 105 (1998).
- [129] J. Anaya, H. Sun, J. Pomeroy, and M. Kuball, *Thermal Management of GaN-on-Diamond High Electron Mobility Transistors: Effect of the Nanostructure in the Diamond near Nucleation Region*, in (IEEE, Las Vegas, NV, USA, 2016), pp. 1558–1565.

- [130] K. E. Goodson, O. W. Käding, M. Rösner, and R. Zachai, *Thermal Conduction Normal to Diamond-silicon Boundaries*, Applied Physics Letters **66**, 3134 (1995).
- [131] V. Goyal, *Thermal Characterization of Nanostructures and Advanced Engineered Materials*, (2011).
- [132] A. Siddique, R. Ahmed, J. Anderson, M. Nazari, L. Yates, S. Graham, M. Holtz, and E. L. Piner, *Structure and Interface Analysis of Diamond on an AlGaIn/GaN HEMT Utilizing an InSitu SiN_x Interlayer Grown by MOCVD*, ACS Applied Electronic Materials **1**, 1387 (2019).
- [133] Y. Zhou, R. Ramaneti, J. Anaya, S. Korneychuk, J. Derluyn, H. Sun, J. Pomeroy, J. Verbeeck, K. Haenen, and M. Kuball, *Thermal Characterization of Polycrystalline Diamond Thin Film Heat Spreaders Grown on GaN HEMTs*, Applied Physics Letters **111**, 041901 (2017).
- [134] H. Sun, R. B. Simon, J. W. Pomeroy, D. Francis, F. Faili, D. J. Twitchen, D. J. Twitchen, and M. Kuball, *Reducing GaN-on-Diamond Interfacial Thermal Resistance for High Power Transistor Applications*, Applied Physics Letter **106**, 111906.1 (2015).
- [135] X. Gu, C. Lee, J. Xie, E. Beam, M. Becker, T. A. Grotjohn, J. Anaya, M. Kuball, and W. R. Road, *GaN-on-Diamond with Ultra-Low Thermal Barrier Resistance GaN-on-Diamond Preparation and Surface Morphology Thermal Characterizations*, in (2016), pp. 405–408.
- [136] D. Liu, D. Francis, F. Faili, C. Middleton, J. Anaya, J. W. Pomeroy, D. J. Twitchen, and M. Kuball, *Impact of Diamond Seeding on the Microstructural Properties and Thermal Stability of GaN-on-Diamond Wafers for High-Power Electronic Devices*, Scripta Materialia **128**, 57 (2017).
- [137] P. W. May, H. Y. Tsai, W. N. Wang, and J. A. Smith, *Deposition of CVD Diamond onto GaN*, Diamond and Related Materials **15**, 526 (2006).
- [138] M. Oba and T. Sugino, *Oriented Growth of Diamond on (0001) Surface of Hexagonal GaN*, Diamond and Related Materials **10**, 1343 (2001).
- [139] P. H. Chung, E. Perevedentseva, J. S. Tu, C. C. Chang, and C. L. Cheng, *Spectroscopic Study of Bio-Functionalized Nanodiamonds*, Diamond and Related Materials **15**, 622 (2006).
- [140] B. L. Hancock, M. Nazari, J. Anderson, E. Piner, F. Faili, S. Oh, D. Twitchen, S. Graham, and M. Holtz, *Ultraviolet Micro-Raman Spectroscopy Stress Mapping of a 75-Mm GaN-on-Diamond Wafer*, Applied Physics Letters **108**, 1 (2016).
- [141] S. Choi, E. Heller, D. Dorsey, R. Vetury, and S. Graham, *The Impact of Mechanical Stress on the Degradation of AlGaIn/GaN High Electron Mobility Transistors*, Journal of Applied Physics **114**, 164501 (2013).

- [142] I. Ahmad, M. Holtz, N. N. Faleev, and H. Temkin, *Dependence of the Stress-Temperature Coefficient on Dislocation Density in Epitaxial GaN Grown on α -Al₂O₃ and 6H-SiC Substrates*, Journal of Applied Physics **95**, 1692 (2004).
- [143] Q. Zheng, C. Li, A. Rai, J. H. Leach, D. A. Broido, and D. G. Cahill, *Thermal Conductivity of GaN, and SiC from 150 K to 850 K*, Phys. Rev. Materials **3**, 014601 (2019).
- [144] R. S. Pengelly, S. M. Wood, J. W. Milligan, S. T. Sheppard, and W. L. Pribble, *A Review of GaN on SiC HEMTs and MMICs*, IEEE **60**, 1764 (2012).
- [145] L. Yates, J. Anderson, X. Gu, C. Lee, T. Bai, M. Mecklenburg, T. Aoki, M. S. Goorsky, M. Kuball, E. L. Piner, and S. Graham, *Low Thermal Boundary Resistance Interfaces for GaN-on-Diamond Devices*, ACS Applied Materials and Interfaces **10**, 24302 (2018).
- [146] J. Cervenka, D. Lau, N. Dontschuk, O. Shimoni, L. Silvestri, F. Ladouceur, S. Duvall, and S. Praver, *Nucleation and Chemical Vapor Deposition Growth of Polycrystalline Diamond on Aluminum Nitride: Role of Surface Termination and Polarity*, Crystal Growth and Design **13**, 3490 (2013).
- [147] P. Pobedinskas, G. Degutis, W. Dexters, W. Janssen, S. D. Janssens, B. Conings, B. Ruttens, J. D'Haen, H.-G. Boyen, A. Hardy, M. K. Van Bael, and K. Haenen, *Surface Plasma Pretreatment for Enhanced Diamond Nucleation on AlN*, Applied Physics Letters **102**, 201609 (2013).
- [148] S. Mandal, C. Yuan, F. Massabuau, J. W. Pomeroy, J. Cuenca, H. Bland, E. Thomas, D. Wallis, T. Batten, D. Morgan, R. Oliver, M. Kuball, and O. A. Williams, *Thick, Adherent Diamond Films on AlN with Low Thermal Barrier Resistance*, ACS Appl. Mater. Interfaces **11**, 40826 (2019).
- [149] M. A. Siddique, *Diamond on GaN: Heterointerface and Thermal Transport Study*, PhD Dissertation, Texas State University, 2018.
- [150] H. Sumiya, N. Toda, and S. Satoh, *Development of High-Quality Large-Size Synthetic Diamond Crystals*, SEI Technical Review **60**, 10 (2005).
- [151] E. L. H. Thomas, S. Mandal, Ashek-I-Ahmed, J. E. Macdonald, T. G. Dane, J. Rawle, C.-L. Cheng, and O. A. Williams, *Spectroscopic Ellipsometry of Nanocrystalline Diamond Film Growth*, ACS Omega **2**, 6715 (2017).
- [152] R. Rounds, B. Sarkar, D. Alden, Q. Guo, A. Klump, C. Hartmann, T. Nagashima, R. Kirste, A. Franke, M. Bickermann, Y. Kumagai, Z. Sitar, and R. Collazo, *The Influence of Point Defects on the Thermal Conductivity of AlN Crystals*, Journal of Applied Physics **123**, 185107 (2018).

- [153] C. Kai, H. Zang, J. Ben, K. Jiang, Z. Shi, Y. Jia, X. Cao, W. Lü, X. Sun, and D. Li, *Origination and Evolution of Point Defects in AlN Film Annealed at High Temperature*, Journal of Luminescence **235**, 118032 (2021).
- [154] J. L. Kennedy, T. D. Drysdale, and D. H. Gregory, *Rapid, Energy-Efficient Synthesis of the Layered Carbide, Al₄C₃*, Green Chem. **17**, 285 (2015).
- [155] H. Seki and M. G. Samant, *Use of Cassegrain System for in Situ Raman Scattering Study of Cyanide Ions on a Palladium Electrode*, Appl. Spectrosc. **47**, 952 (1993).
- [156] D. Cosano, C. Esquinas, C. Jiménez-Sanchidrián, and J. R. Ruiz, *Use of Raman Spectroscopy to Assess the Efficiency of MgAl Mixed Oxides in Removing Cyanide from Aqueous Solutions*, Applied Surface Science **364**, (2015).
- [157] H. Kroencke, s Figge, D. Hommel, and B. M. Epelbaum, *Determination of the Temperature Dependent Thermal Expansion Coefficients of Bulk AlN by HRXRD*, Acta Physica Polonica A **114**, 1193 (2008).
- [158] M. A. Reshchikov, A. Usikov, H. Helava, Yu. Makarov, V. Prozheeva, I. Makkonen, F. Tuomisto, J. H. Leach, and K. Udvary, *Evaluation of the Concentration of Point Defects in GaN*, Scientific Reports **7**, 9297 (2017).
- [159] P. F. Fewster, *X-Ray Analysis of Thin Films and Multilayers*, Reports on Progress in Physics **59**, 1339 (1996).
- [160] Y. Feng, V. Saravade, T.-F. Chung, Y. Dong, H. Zhou, B. Kucukgok, I. T. Ferguson, and N. Lu, *Strain-Stress Study of Al_xGa_{1-x}N/AlN Heterostructures on c-Plane Sapphire and Related Optical Properties*, Scientific Reports **9**, 10172 (2019).
- [161] A. R. Denton and N. W. Ashcroft, *Vegard's Law*, Phys. Rev. A **43**, 3161 (1991).